

Vol. 31/1
January, 2019

ISRAPS Bulletin

NSRP-2019
SPECIAL ISSUE



Guest Editors
Soumyakanti Adhikari
Subrata Sinha

A Publication of
Indian Society for
Radiation and Photochemical Sciences

Message from the President and Secretary

Dear ISRAPS Members,

On behalf of the ISRAPS Executive Council, we wish you all a very happy new year 2019 and take this opportunity to acknowledge the contribution of all the members who have actively participated in organizing various activities of ISRAPS at different institutes.

Apart from successfully organizing the TSRP-2018 in collaboration with Chemistry Group, BARC, during Jan 3-7, 2018, ISRAPS has also supported the organization two One Day Discussion Meetings in 2018; one on Spectroscopy and Dynamics of Chemical and Biological Systems at SINP, Kolkata on 5th May 2018 and the other one on Atmospheric Chemistry at IACS, Kolkata on November 24, 2018. Both the meetings focussed on the state of the art research on their respective research domain and provided a common platform in bringing collaboration, by sharing technical information among the research groups. The EC thank all those who contributed to the success of these endeavours.

This special bulletin which is brought out on the occasion of National Symposium on Radiation and Photochemistry (NSRP-2019) being organized at Visva Bharati, Santiniketan, Kolkata, during Feb. 7-9, 2019, is a collection of articles on the topics discussed in the meeting. The Executive Council of ISRAPS take this opportunity to thank all the speakers/contributors of NSRP-2019 and record our gratitude to Dr. Soumyakanti Adhikari and Dr. Subrata Sinha for their active role in organizing the NSRP-2019 and bringing out this special bulletin serving as Guest Editors. ISRAPS executive council sincerely requests all the member scientists and students to participate and contribute whatever way possible to spread the knowledge of Radiation and Photochemical Sciences among young researchers in the country. As in the past, the society will be happy to provide all logistical support for such an event.

Once again ISRAPS council wish to express our sincere gratitude to all life members for their constant support and encouragement and look forward to your valuable suggestions and active participation in the forthcoming events of ISRAPS.



(P. D. Naik)
President, ISRAPS



(A. C. Bhasikuttan)
Secretary, ISRAPS



ISRAPS Bulletin

A Publication of
Indian Society for Radiation and Photochemical Sciences

Editor's Desk...

It is our privilege to present this NSRP-Special Issue of ISRAPS Bulletin on the auspicious occasion of the National Symposium on Radiation & Photochemistry organized jointly by Indian Society for Radiation and Photochemical Sciences (ISRAPS) and the Integrated Science Education & Research Centre (ISERC), Visva-Bharati, Santiniketan, during February 7-9, 2019.

The symposium deliberations would cover many areas of Radiation and Photochemistry which are being pursued in different laboratories in the national level. The present issue provides a glimpse of some of the selected research and their applications under the umbrella of the twin area presented in the symposium. The articles cover areas such as heterogeneity in molecular and cluster level of doped carbon nanodot; intertwined facet of lasers and accelerators; radiation processing as a non-thermal technology for food preservation; radiation chemical reaction using porous platinum nanoballs; reaction of model peroxy radicals; and super-strong van der Waals complexes involving noble gases. Although these articles give the flavor of the works from some selected labs only, we are confident that the level of science portrayed as well as the diverse nature of the studies will stimulate the youngsters in the area to explore worthy aspects.

We sincerely acknowledge the active cooperation received from all the contributors of the articles appearing herein. We also thank ISRAPS for entrusting editorial responsibility on us.

Soumyakanti Adhikari & Subrata Sinha
(Guest Editors)



Dr. Soumyakanti Adhikari is working as Scientific Officer (H) in the Radiation & Photochemistry Division, Bhabha Atomic Research Centre and an affiliated Professor at Homi Bhabha National Institute, Mumbai. He has obtained his Ph. D. (Physical Chemistry) degree from University of Mumbai, India in 2000. He is the recipient of the prestigious IUPAC Prize for Young Chemist in 2001, Scientific and Technical Excellence Award, DAE in 2008. He has worked as Visiting Scientist at Leipzig, Germany, 1999 and at the Hahn Meitner Institute, Berlin, Germany, 2002. He was Visiting Professor, at ISIR, Sanken, Osaka, Japan, 2007. Dr. Adhikari is the Editorial Board Member of

Oriental Journal of Chemistry; and Vice President of Society for Free Radical Research (SFRR)-India. His research interests are: Radiation chemistry of microheterogeneous media, ionic liquids and deep eutectic solvents; Free radical chemistry and biology involving natural and synthetic antioxidants; Radiation chemical synthesis, characterization and application of nanomaterials. Dr. Adhikari is now involved in the development of Picosecond Electron Accelerator in BARC for ultrafast radiation chemical studies.



Dr. Subrata Sinha is Associate Professor in the Integrated Science Education & Research Centre (ISERC), Visva-Bharati, Santiniketan. He obtained the Ph. D. degree from Jadavpur University while working at Indian Association for the Cultivation of Science in 1998 and M. Sc. in Physics from Jadavpur University in 1993. He had pursued his Post-doctoral works during 1999-2004 at Lund University (Sweden), University of Durham (England), Kyoto University (Japan) as JSPS Fellow, National Institute of Advanced Industrial Science and Technology (Japan). Dr. Sinha is involved in different projects sponsored by DAE-BRNS, CSIR, DST-RMES. His recent Research interest is in the area of Molecular spectroscopy.



INDIAN SOCIETY FOR RADIATION AND PHOTOCHEMICAL SCIENCES (ISRAPS)

EXECUTIVE COUNCIL (2018-2020)

President

Dr. P. D. Naik

Vice-Presidents

Prof. S. Wategaonkar

Dr. D. B. Naik

Secretary

Dr. A.C. Bhasikuttan

Joint Secretary

Prof. A. Datta

Treasurer

Dr. (Mrs) J. Mohanty

Executive Members

Dr. S. Adhikari

Dr. T. Bandyopadhyaya

Dr. Atanu Barik

Prof. T. Chakraborty

Dr. Aloke Das

Dr. Awadhesh Kumar

Prof. A. S. Kumbhar

Dr. S. Nath

Dr. D. K. Palit

Dr. C. N. Patra

Prof. P. Ramamurthy

Dr. H. P. Upadhyaya

Co-opted Members

Dr. Y.K. Bhardwaj

Dr. G. R. Dey

Dr. T. K. Ghanty

Dr. (Mrs) Nandita Maiti

Dr. J. P. Mittal

Dr. J. A. Mondal

Dr. Alok Samanta

Dr. S. K. Sarkar

Dr. (Mrs) S. Sen Gupta

Prof. Anil K. Singh

Dr. V. S. Tripathi

Dr. R.K. Vatsa

Web Master

Mr. Abhishek Das

Contact Details:

C/o Radiation & Photochemistry Division
Bhabha Atomic Research Centre, Mumbai - 400 085

E-mail: israps.secretary@gmail.com

Telephone: (022)- 25595398/25593866/25593771

Web: www.israps.org.in



INDIAN SOCIETY FOR RADIATION AND PHOTOCHEMICAL SCIENCES

(Reg. No. 617/1985, GBBSD, Bombay; Trust No. F-10965)

Radiation & Photochemistry Division

Bhabha Atomic Research Centre, Mumbai - 400 085

Member Enrolment Form

1. Name in Block Letters:
2. Date of Birth:
3. Highest Academic Qualification:
4. Present Position:
5. Addresses:

Photograph

Office	Residence
Telephone E-mail	Telephone E-mail

6. Address for Correspondence: Office / Residence
7. Category of Membership Applied for: Annual / Life / Corporate member
8. Remittance: DD in favour of 'ISRAPS' payable at MUMBAI
For Bank Transfer:
A/c No.10536133801, SBI, BARC Branch, IFSC SBIN0001268
(e-mail the money transfer details along with the details requested above to israps.secretary@gmail.com and CC to bkac@barc.gov.in)

Category	Fees	Admission fee	Total Amount
Annual	Rs 200/-	Rs 100/-	Rs 300/-
Life Member	Rs 1500/-	Rs 100/-	Rs 1600/-
Corporate Member	Rs 20000/-	Rs 1000/-	Rs 21000/-

9. Brief Resume of activities and research interests:
10. List of memberships of other professional bodies, if any:
11. List of prizes/awards/fellowships received, if any:
12. Number of Publications:

I agree to abide by the constitution and bye-laws, and rules and regulations of the SOCIETY.

Place:

Signature

Date:

Contents

Message from the President and Secretary, ISRAPS	i
Guest Editors	
<i>Soumyakanti Adhikari</i>	
<i>Subrata Sinha</i>	iii
Doped Carbon Nanodot: Heterogeneity in Molecular and Cluster level	1
<i>Debashis Panda, Shivam Dwivedi</i>	
Intertwined Facet of Lasers and Accelerators	8
<i>Sisir K Sarkar</i>	
Radiation Processing: A non-thermal technology for food preservation	16
<i>Sunil K. Ghosh</i>	
Pulse Radiolysis Study of 4-Nitrophenol Reduction Reaction using Porous Platinum Nanoballs	25
<i>G. K. Sharma and K. K. K. Sharma</i>	
Reactions of model peroxy ($\text{CCl}_3\text{O}_2\cdot$) radical by radiation chemical method	32
<i>Shaukat Ali M. Shaikh, Rupali G. Shinde, Atanu Barik</i>	
“Super-Strong” van der Waals Complexes involving Noble Gases	40
<i>Ayan Ghosh and Tapan K. Ghanty</i>	

Doped Carbon Nanodot: Heterogeneity in Molecular and Cluster level

Debashis Panda*, Shivam Dwivedi

*Rajiv Gandhi Institute of Petroleum Technology,
(An Institute of National Importance)*

Jais, Uttar Pradesh, INDIA

Email: dpanda@rgipt.ac.in

Abstract

The effect of doping on the luminescence dynamics of carbon nanodots (CNDs) have been poorly understood, at least at the molecular level. We have used molecular dopant, thiourea for the synthesis of N, S doped nanodots. The synthesized nanodots exhibit phenomenologically similar but mechanistically distinct emission properties. We provide evidences for the heterogeneity at molecular and cluster level, primarily involving two fluorophores. We identify the two molecular fluorophores with characteristic emission properties. The computed vertical excitations of the molecular fluorophore predicted by the reaction mechanism suggests presence of thiazolopyridone-moiety. Citrazinic acid in DMF exhibits excitation dependent emission suggesting formation of different-sized clusters, which is also evident from the DLS particle-size measurements. The luminescence dynamics of N, S-doped nanodot is primarily thus dictated by distinct fluorophores and their different-sized clusters.

1. Introduction

In recent times, carbon nanodots (CNDs) have emerged as an exciting quasi-0D class of nanomaterial due to their one-pot synthesis and superior optoelectronic functionalities.¹⁻³ In particular, CNDs have generated profound interest owing to its unique excitation-dependent luminescence, low-toxicity, and biocompatibility.⁴⁻⁸ Nanodots also possess very unique properties, such as high photostability, good water solubility and effective surface immobilization. Apart from imaging applications, it finds numerous exciting applications in such as energy conversion, catalysis, light-emitting diodes, and photovoltaic devices.⁹⁻¹⁴ Nanodots are reportedly synthesized by a bottom-up chemical synthesis- hydrothermal method. The starting materials are a mixture of either polyols/ polyacids and amines or carbohydrates and amino acids.¹⁵⁻²¹ Considering the presence of graphitic nature of nanodots observed in electron microscopy, nitrogen and sulphur -doped CNDs have also been synthesized in order to augment the

optoelectronic properties.²²⁻²⁴ Surprisingly, most CNDs irrespective of their synthetic strategies are found to display considerable similarities in their photoluminescence (PL) spectra- excitation wavelength-dependent emission.

The origin of that excitation wavelength-dependent emission has been attributed to various effects such as solvent relaxation, electron-hole recombination, red edge shift, etc.²⁵⁻²⁸ In addition, the emission property of nanodot has been dissected into two components- first, a strong fluorescence from fluorophore molecules at shorter wavelengths, and second, the weak emission from carbon cores at longer wavelengths.¹⁶ Most recently, it has been reported that the fluorophore aggregates, such as citrazinic acid and methylsuccinic acid reproduce the emissive features of nanodots, thus contradicting the hypothesis on the contribution of graphitic domains to the emission features of CNDs.²⁹ However, the hypothesis of aggregates requires validations due to the fact that both the aggregation mentioned is either requires

heterogeneous (polymeric) environment or solid state, i.e. crystal phase. On the other hand, the fluorophore is ubiquitous in nanodot synthesis. The citrazinic acid has been identified as a product of the reaction of citric acid and either ammonia or urea precursors, whereas methylsuccinic acid is the product of hydrothermal treatment of citric acid only.^{15,30} The pyrrolopyridine fluorophoric unit (akin to vesperlysine) is hypothesized to contribute to the luminescence properties of CNDs derived from carbohydrates and amino acids.²¹ We have synthesized doped-nanodots from a bioresource, lemon juice. Thiourea is selected as a molecular source of “so-called” dopant- nitrogen and sulfur. To rationalize the molecular fluorophores present in a bio-resource-derived nanodot, a direct comparative study with citric acid-derived nanodot has also been made and striking similarities have been highlighted. The molecular structures of the fluorophores have been predicted by using quantum chemical methods. We show that H-bonding has a significant role in the excitation dependent emission.

2. Experimental Section

2.1 Materials

Citrazinic acid (Alfa-Aesar), Citric Acid (SDFCL), Thiourea (SDFCL) are purchased and used as received. Polyvinyl alcohol (SDFCL), polyvinyl pyrrolidone (SRL), Silica (SDFCL), Silver nitrate (SDFCL), Dimethyl Formamide (SRL) are obtained from the respective companies. All chemicals used in the experiments of analytical grade and used without any purification. Water from ELGA LAB Water-purifier (18.2 mΩ) is used throughout the experiments.

2.2 Synthesis of Carbon Nanodot

In a typical synthesis, fresh lemons are squeezed to obtain 30 mL of pulp-free juice which is centrifuged at 13000 rpm for 20 minutes. The supernatant is then filtered through Whatman paper filter paper (11μM pore size). The 20 mL of clear solution obtained thereafter

is mixed with 0.5 g thiourea for the synthesis of CND1. Whereas for CND2, commercially available chemical, citric acid and thiourea are used at the same reaction condition. The solution is thereafter transferred into a Teflon-coated stainless steel autoclave (purchased from M/S Shilpa Enterprises, Nagpur, India) at 160°C for 7 hours. After cooling to room temperature, the color of the solution is changed to reddish brown from whitish, indicating formation of carbon dots. The reddish brown solution is centrifuged again at 13000 rpm for 20 minutes to remove large particles and thereafter silica loaded column chromatographic method is employed to further purify the supernatant solution.

2.3. Instrumentation

The steady state absorption spectra are collected using a LAB India UV-Vis 3200 spectrophotometer. Steady state photoluminescence (PL) spectra are recorded on a Varian Cary Eclipse fluorescence spectrophotometer with a Peltier temperature controller. The Perkin Elmer Spectrum Two FT-IR spectrometer is used to record the FT-IR spectra of the vacuum dried samples. The samples are recorded using “attenuated total reflectance” (ATR) mode. The PIKE MIRacle™ single reflection horizontal ATR accessory is used for recording the FT-IR spectra. Time-resolved emission measurements are performed using Time Correlated Single Photon Counting (TC-SPC) system, from IBH, UK. The decay traces for each of the excitation are analyzed with IBH DAS v6.2 data analysis. Using the iterative re-convolution method, the data were fitted to the sum of multi-exponential functions as shown below:

$$I(t) = I(0) \sum_i A_i \exp\left(-\frac{t}{\tau_i}\right)$$

$I(t)$ and $I(0)$ are the emission intensities at time t and zero after excitation by the source. A_i is the amplitude of the i th component. CNDs are imaged by a transmission electron microscope (TEM) (HR-TEM FEI Titan G2 60) mounted with field emission gun FEG TEM at 300

kV accelerating voltage. The Malvern Zetasizer (Nano) has been used to measure the hydrodynamic diameter of the sample.

2.4. Quantum Chemical Calculations

The ground state geometries of thiazolopyridone (molecule-1) and thiazolopyridine (molecule-2) are optimized using the density functional theory method with the Becke3LYP functional as implemented in GAUSSIAN 09w software package. The default options for the self-consistent field (SCF) convergence and threshold limits in the optimization are used. Time dependent density functional theory (TDDFT) calculations are performed on the gas phase optimized geometry of the ground state (S_0) and vertical excitations are carefully analyzed.

3. Results & discussion

3.1. Characterizations of carbon nanodots

Determining the impact of thiourea in dictating the structure and thereby luminescence properties of nanodots is a subject of study here. The synthesis is therefore designed to produce the N,S-doped nanodots. At first, Fourier Transform Infrared (FT-IR) spectroscopy is used for identification of functional groups present in the synthesized carbon nanodots (Figure 1A). From 3600 to 2800 cm^{-1} , the stretching vibrations of C-H, N-H, O-H, and COO-H contribute to the broad IR band. The stretching vibration at 2058 cm^{-1} is assigned to SCN bonding.^{31,32} The strong FTIR bands at 1700 cm^{-1} and 1565 cm^{-1} belong to C=O and C=C vibrations respectively. At 1393 cm^{-1} , a strong C-N stretching can be assigned to the pyridone unit of the molecule, that is also predicted by quantum chemical calculations.

The high-resolution transmission electron microscopy (HRTEM) is employed to understand the precursor-dependent graphitization of nanodots (Figure 1B). TEM images of CND1 indicate the deposition of particles on a flake-like nanosheets. The average diameter of the particles deposited is measured to be 11.9 ± 4.1 nm. Moreover, high-resolution TEM images show

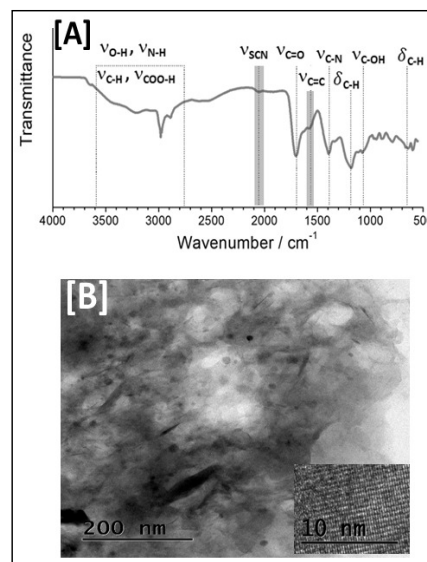


Figure 1: [A] ATR FT-IR spectra of (i) CND1 (blue-line). [B] TEM image of CND1; Inset HRTEM image of CND1 with lattice spacing (approx. 0.25 nm).

two-dimensional nanosheets (graphene-like) with the appearance of lattice fringes distributed in the nanosheet matrix. The observed lattice spacing of 0.25 nm is referred to the [020] facet of graphitic carbon.^{33,34}

3.2. Luminescence Dynamics of Carbon Nanodots

Figure 2A summarizes the excitation wavelength dependence of the CNDs as a function of the emission peak. Interestingly, the emission peaks of CND2 appear in the same range as CND1, 420 nm, and 508 nm respectively. However, two distinct emission peaks appear in the excitation window from 290-490 nm for the synthesized nanodots. The emission maximum remains unchanged for the nanodots for the blue-end excitations, 290- 370 nm. Similarly, for the excitation range 420- 470 nm, the emission maximum hardly shifts and resides between 500 -508 nm. The gradual shift of emission peak from either 450 nm or 425 nm to green end 508 nm indicates a typical two-state existence. A two-fluorophore system upon excitation is expected to exhibit two distinct peaks. The disappearance of such distinct emission peaks might have resulted from the inhomogeneous spectral broadening of

nanodots in water. However, a closer inspection has been discussed as well at later.

The synchronous luminescence spectrum of CND1 appears relatively broader in the blue-end region (Figure 2B). To rationalize the ground state heterogeneity further, the synchronous spectrum of CND2 is compared with CND1. Interestingly, a considerable overlap of the peak at 454 nm is noticed for CND1, thus indicating the identical molecular structure of the fluorophore. The study therefore infers that the luminescence from the doped nanodot is primarily originated by two fluorophores. In time-resolved fluorescence measurements, an attempt has been made to cover the entire emission range by picking the high-intensity emission wavelengths- 420

nm, 460 nm and 510 nm for 336 nm excitation; 510 and 550 nm for 440 nm excitations. Since the decays are multiexponential, therefore, then it is pertinent to use an average decay time. Figure 2C illustrates the dependence of fluorescence lifetime on emission wavelengths for an excitation wavelength. The luminescence lifetime is found to be more-or-less independent of emission wavelength, whereas strongly depends on the excitation wavelengths, which is the characteristic of a system having number of molecular fluorophores. Unprecedentedly, a sharp change in fluorescence lifetime is observed at 510 nm emission wavelength, thus confirming the presence of two-fluorophores. Analysis of decay traces of CND1 at 336 nm excitation reveals the presence of two components in aqueous solution: a short one with a lifetime (τ_1) of 2.49 ns (± 0.52), and longer component (τ_2) 7.07 ns (± 0.55). The average lifetime of CND1 is estimated to be 6.52 ns (± 0.48) for the emission wavelengths.¹⁵ This is a very similar to a molecular-fluorophore-citrazinic acid.

3.3. Role of H-bonding for excitation dependent emission

Citrazinic acid is commercially available, however, sparingly soluble in water. Hence, dimethyl formamide (DMF), apolar solvent is used for the study. Emission spectra of citrazinic acid in DMF shows strong excitation dependence (Figure 4 A), resembling to a nanodot behavior. Surprisingly, the synchronous spectrum clearly identifies the ground state heterogeneity, i.e. at cluster level. To substantiate that claim, we have carried out the dynamic light scattering (DLS) studies to determine the distribution of sizes of such clusters. The average diameter in DMF is found be 72 nm, which is much larger than the molecular size. Therefore, the similar observation in nanodot indicates identical cluster sizes. The formation of such clusters is highly expected in nanodot as the most of reactions are carried out in acidic condition and high temperature in which the water is not only acidic (pH of water at 160°C \sim 5.7), also apolar

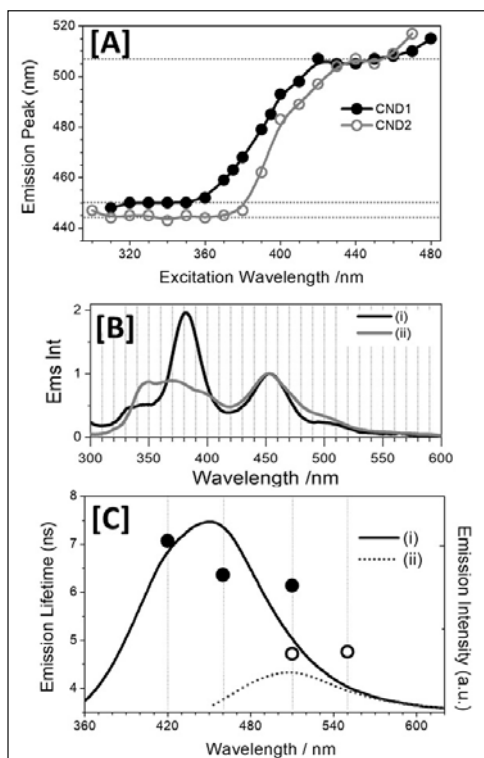


Figure 2: [A] The emission maximum as a function of the excitation wavelength. [B] Synchronous luminescence spectra of – (i) CND1 (grey line) and (ii) CND2 (black line) in aqueous solution. $\Delta\lambda = 20$ nm. [C] Average luminescence lifetime over emission wavelengths of CND1; at 336 nm excitation, CND1 (solid circle), and at 440 nm excitation (hollow circle). Solid line show the representative emission spectra recorded at $\lambda_{exc} = 340$ nm, whereas the dotted lines at $\lambda_{exc} = 440$ nm.

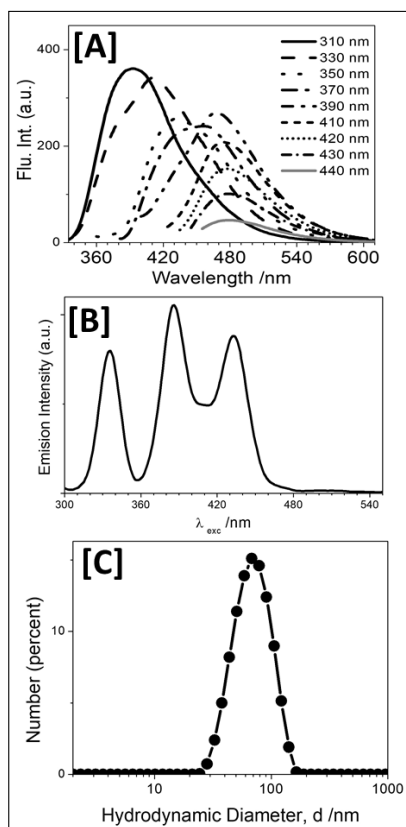


Figure 3: Citrazinic Acid in DMF- [A] Excitation-dependent emission spectra, [B] Synchronous luminescence spectrum, [C] Hydrodynamic diameter.

in nature due to low dielectric constant of water ($\epsilon \cong 42$) at 160°C.

3.4. Identification of fluorophores

As already stated earlier that the first fluorophore is the citrazinic acid-type, whereas for the identification of second one, a reaction mechanism has been proposed (Figure 4A). Decomposition of thiourea yields ammonia and isothiocyanate. First, the reaction of weak organic acids with ammonia results in the formation of citrazinic acid (precursor- citric acid). Thereafter, isothiocyanate reacts with citrazinic acid to form thiazolopyridone.^{35,36} It can be mentioned here that the X-ray Photoelectron spectroscopic (XPS) studies on N, S-doped CNDs suggested the presence of two types of nitrogens - pyridinic (399.7 eV), pyrrolic (400.6 eV) and thiophenic-S (164.3 eV).²³ The molecule predicted from the reaction mechanism also contain the pyridinic,

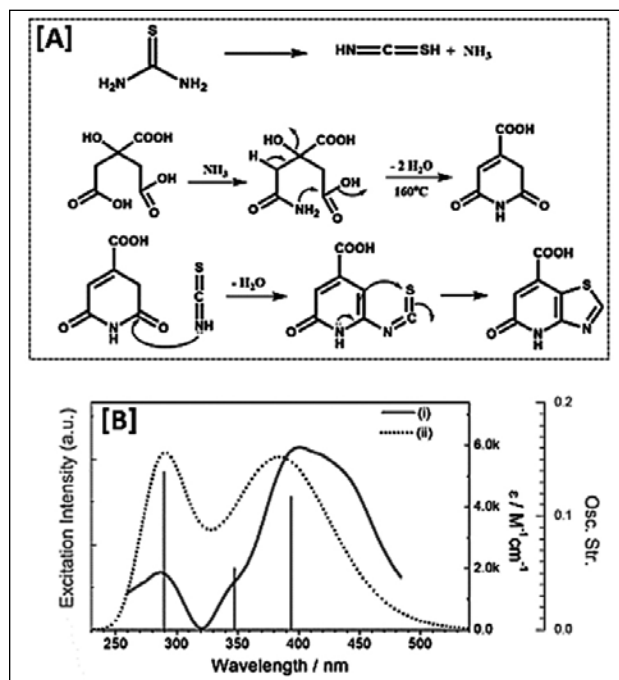


Figure 4: [A] Proposed reaction mechanism for the formation of fluorophore- thiazolopyridone. [B] Comparison between computed absorption spectra of proposed molecule (in gas phase) and the difference excitation spectrum (red line) of CND1 at 500 nm in water. The computed absorption spectra- (i) molecule (solid blue line) and (ii) molecule-1 (black dotted line). Oscillator strengths associated with vertical transitions for molecule (solid blue vertical lines).

pyrrolic nitrogens and thiophenic sulfur as well.

The isolation of thiazolopyridone is relatively difficult due to their covalent bonding to the other units of nanodot. Thus the quantum chemical computations have been performed. TDDFT calculations predict the wavelengths associated with vertical transitions in the lower energy regions are- 376.9 nm (3.289 eV) and 281.4 nm (4.405 eV) for molecule; The computed absorption spectra have been compared with the difference excitation spectrum of CND1 (Figure 4B). However, the difference spectrum is obtained by the subtraction of excitation spectrum of CND1 at 500 nm from that of CND2 at 400 nm due to the fact that the CND1 and CND2 exhibit considerable similarities in their excitation spectra recorded at 400 nm. The predicted wavelength for high energy absorption- 281.4 nm for product

molecule (and 289.8 nm for molecule 2) is found to be in excellent agreement with experimental excitation spectrum and thus satisfactorily explain the gradual appearance of shoulder peak at 290 nm in the excitation spectra of nanodots. The predicted highest intensity transitions in the lower energy regions are found to be in fairly good agreement with the most intense experimental excitation maxima and suggest the broad excitation spectrum in the red end of the emission. However, it should be mentioned here that the difference of 30-40 nm (0.32 - 0.23 eV) in peak maxima is due to the omission of solvent polarity and specific interactions such as H-bonding, surface interaction might be the reason for the underestimation of computed vertical transitions.^{37,38}

4. Conclusion

In conclusion, N, S-doped nanodots exhibit excitation-independent emission at two ends of the excitation spectrum with distinct emission peaks. The ground-state heterogeneity probed by synchronous fluorescence spectroscopy confirms the existence of two-fluorophore in the doped nanodot. The emission lifetimes at the varied excitations are found to be more-or-less independent of emission wavelengths, thus suggesting molecular-like properties. In particular, the computed vertical excitations for thiazolopyridone are in fairly good agreement with the excitation spectrum of nanodot. Thus, the luminescent N, S-doped nanodot has molecular heterogeneity-citrazinic acid and thiazolopyridone. Excitation dependent emission of only citrazinic acid indicates heterogeneity at cluster level as well.

Acknowledgements

The authors greatly acknowledge RGIPT-Rae Bareilly and the Science and Engineering Research Board, Department of Science and Technology, New Delhi for financial support (DST Project No.: SB/FT/CS-135/2013). Authors are grateful to Prof. Anindya Datta, IIT Bombay for availing the facility of time-resolved emission

measurements. Authors are thankful to Waqar Kaleem, Anand Kumar and Hemen Gogoi, for the help in experimentations. Authors acknowledge Advanced Imaging Centre at IIT Kanpur for Electron Microscopic Characterizations.

References

1. Zhu, S.; Meng, Q.; Wang, L.; Zhang, J.; Song, Y.; Jin, H.; Zhang, K.; Sun, H.; Wang, H.; Yang, B. *Angew. Chem. Int. Ed.* **2013**, *52*, 3953–3957.
2. Li, H.; Kang, Z.; Liu, Y.; Lee, S.-T. *J. Mater. Chem.* **2012**, *22*, 24230.
3. Hola, K.; Zhang, Y.; Wang, Y.; Giannelis, E. P.; Zboril, R.; Rogach, A. L. *Nano Today* **2014**, *9*, 590–603.
4. Baker, S. N.; Baker, G. A. **2010**, *49*, 6726–6744.
5. Wang, K.; Gao, Z.; Gao, G.; Wo, Y.; Wang, Y.; Shen, G.; Cui, D. *Nanoscale Res. Lett.* **2013**, *8*, 122.
6. Ruan, S.; Qian, J.; Shen, S.; Zhu, J.; Jiang, X.; He, Q.; Gao, H. *Nanoscale* **2014**, *6*, 10040–10047.
7. Chen, J.; Wei, J. S.; Zhang, P.; Niu, X. Q.; Zhao, W.; Zhu, Z. Y.; Ding, H.; Xiong, H. M. *ACS Appl. Mater. Interfaces* **2017**, *9*, 18429–18433.
8. Ghosh, S. et al. *Nano Lett.* **2014**, *14*, 5656–5661.
9. Li, H.; He, X.; Kang, Z.; Huang, H.; Liu, Y.; Liu, J.; Lian, S.; Tsang, C. H. A.; Yang, X.; Lee, S.-T. *Angew. Chem. Int. Ed.* **2010**, *49*, 4430–4434.
10. Qu, S.; Liu, X.; Guo, X.; Chu, M.; Zhang, L.; Shen, D. *Adv. Funct. Mater.* **2014**, *24*, 2689–2695.
11. Sun, C.; Zhang, Y.; Sun, K.; Reckmeier, C.; Zhang, T.; Zhang, X.; Zhao, J.; Wu, C.; Yu, W. W.; Rogach, A. L. *Nanoscale* **2015**, *7*, 12045–12050.
12. Yu, S.; Lee, S. Y.; Umh, H. N.; Yi, J. *Nano Energy* **2016**, *26*, 479–487.
13. Liu, J.; Liu, Y.; Liu, N.; Han, Y.; Zhang, X.; Huang, H.; Lifshitz, Y.; Lee, S.-T.; Zhong, J.; Kang, Z. *Science*. **2015**, *347*, 970–974.
14. Majumdar, B.; Mandani, S.; Bhattacharya, T.; Sarma, D.; Sarma, T. K. *J. Org. Chem.* **2017**, *82*, 2097–2106.
15. Schneider, J.; Reckmeier, C. J.; Xiong, Y.; Von Seckendorff, M.; Susha, A. S.; Kasak, P.; Rogach, A. L. *J. Phys. Chem. C* **2017**, *121*, 2014–2022.
16. Fu, M.; Ehrat, F.; Wang, Y.; Milowska, K. Z.; Reckmeier, C.; Rogach, A. L.; Stolarczyk, J. K.; Urban, A. S.; Feldmann, J. *Nano Lett.* **2015**, *15*, 6030–6035.
17. Li, H.; Chen, L.; Wu, H.; He, H.; Jin, Y. *Langmuir* **2014**, *30*, 15016–15021.
18. Sun, D.; Ban, R.; Zhang, P. H.; Wu, G. H.; Zhang, J. R.; Zhu, J. *J. Carbon* **2013**, *64*, 424–434.
19. Qu, S.; Wang, X.; Lu, Q.; Liu, X.; Wang, L. *Angew. Chem. Int. Ed.* **2012**, *51*, 12215–12218.
20. Sun, Y. P. et al. *J. Am. Chem. Soc.* **2006**, *128*, 7756–7757.
21. Nema, A.; Pareek, R.; Rai, T.; Panda, D. *ChemistrySelect* **2017**, *2*, 11255–11264.
22. Dong, Y.; Pang, H.; Yang, H. Bin; Guo, C.; Shao, J.; Chi, Y.; Li, C. M.; Yu, T. *Angew. Chem. Int. Ed.* **2013**, *52*, 7800–7804.
23. Qu, D.; Zheng, M.; Du, P.; Zhou, Y.; Zhang, L.; Li, D.; Tan, H.; Zhao, Z.; Xie, Z.; Sun, Z. *Nanoscale* **2013**, *5*, 12272.

24. Xu, Q.; Pu, P.; Zhao, J.; Dong, C.; Gao, C.; Chen, Y.; Chen, J.; Liu, Y.; Zhou, H. *J. Mater. Chem. A* **2015**, 3, 542–546.
25. Khan, S.; Gupta, A.; Verma, N. C.; Nandi, C. K. **2015**, 15, 8300–8305.
26. Gude, V.; Das, A.; Chatterjee, T.; Mandal, P. K. *Phys. Chem. Chem. Phys.* **2016**, 18, 28274–28280.
27. Nguyen, V.; Si, J.; Yan, L.; Hou, X. *Carbon*. **2015**, 95, 659–663.
28. Wang, L. et al. *ACS Nano* **2014**, 8, 2541–2547.
29. Reckmeier, C. J.; Schneider, J.; Xiong, Y.; Häusler, J.; Kasák, P.; Schnick, W.; Rogach, A. L. *Chem. Mater.* **2017**, 29, 10352–10361.
30. Khan, S.; Sharma, A.; Ghoshal, S.; Jain, S.; Hazra, M. K.; Nandi, C. K. *Chem. Sci.* **2018**, 9, 175–180.
31. Lieber, E.; Rao, C. N. R.; Ramachandran, J. *Spectrochim. Acta* **1959**, 13, 296–299.
32. Stripp, S. T.; Lindenstrauss, U.; Sawers, R. G.; Soboh, B.. *PLoS One* **2015**, 10, e0133118.
33. Sahu, S.; Behera, B.; Maiti, T. K.; Mohapatra, S. *Chem. Commun.* **2012**, 48, 8835.
34. Sharma, A.; Gadly, T.; Neogy, S.; Ghosh, S. K.; Kumbhakar, M. *J. Phys. Chem. Lett.* **2017**, 8, 1044–1052.
35. Lee, T.; Lee, D.; Lee, I. Y.; Gong, Y.-D. *J. Comb. Chem.* **2010**, 12, 95–99.
36. Chorell, E.; Das, P.; Almqvist, F. *J. Org. Chem.* **2007**, 72, 4917–4924.
37. Panda, D.; Mishra, P. P.; Khatua, S.; Koner, A. L.; Sunoj, R. B.; Datta, A. *J. Phys. Chem. A* **2006**, 110, 5585–5591.
38. Halim, S. A.; Khalil, A. K. *J. Mol. Struct.* **2017**, 1147, 651–667.



Dr. Debashis Panda received his B.Sc. from Calcutta University, M.Sc. (2004) and Ph.D. (2007) from Indian Institute of Technology, Bombay. He did his postdoctoral research at Cornell University, USA, (2008–2010) with Prof. Peng Chen on Protein-DNA interaction at single-molecule level. During 2011–2012, he did another postdoctoral research at Waseda University, Japan with Late Prof. Kazuhiko Kinoshita Jr., on single molecule biophysics. Since then, he is working as an Assistant Professor at Rajiv Gandhi Institute of Petroleum Technology (RGIPT), An “Institute of National Importance”. The focus of his group is to understand the fundamentals of the bio-derived nanostructures and their applications.



Mr. Shivam Dwivedi did his B.Sc. with Chemistry from Lucknow University in 2016 and M.Sc. from Ram Manohar Lohia Avadh (RMLA) University in 2018. After completion of his Master degree he joined the group of Dr. Debashis Panda at RGIPT, Jais (U.P.) in 2018. His area of research is Bio-Nano-Photonics.

Intertwined Facet of Lasers and Accelerators

Sisir K Sarkar

Bhabha Atomic Research Centre & National Centre for Free Radical Research

Savitribai Phule Pune University India

sarkarsk@barc.gov.in; sarkarsk@chem.unipune.ac.in

Abstract

The major outcome of the intertwined relationship of lasers and accelerators are Free Electron Laser (FEL) and Laser-driven Plasma Accelerators (LPA). Both of these areas have advanced enormously since they were first proposed over 40-50 years back. Several applications of them have been demonstrated, and further developments in this direction are awaited. Even a complete marriage has recently been demonstrated by building FEL using LPA.

The impressive advances in LPA have, in large part, been enabled by rapid progress in the development of high-power, ultrafast laser systems and especially the development of Chirped Pulse Amplification (CPA). Important next stages in the story of LPA will be their successful adaptation to driving new applications in time-resolved science, and the demonstration of acceleration to particle energies of hundreds of GeV. Successful delivery of these instalments rest on continued advances in high-power laser systems, close cooperation between those with expertise in lasers and conventional accelerator science including plasma physics, particle physics, and constructive dialogue between these groups.

Introduction

When J. J. Thomson discovered the electron, he was indeed using an instrument called accelerator. By applying a potential across two electrodes he accelerated the particles and manipulated the resulting beam with electric and magnetic fields to determine the charge-to-mass ratio of cathode rays. Thomson studied the properties of the beam itself and not its interaction on a target or another beam, as we do today. Thereafter accelerators have become indispensable in understanding the Nature at smaller and smaller scales. Although they have become much bigger and more complex, they still operate on much the same physical principles as Thomson's device. Over next fifty years accelerators became key tools in the subatomic particles research. After 1970 colliders-machines using two accelerated beams in collision are developed and they played major role in new revelations in particle physics. Energies required are in the range of a thousand electron volts to examine matter at the scale of an atom, while it is in MeV for probing nucleus. For interrogation of the fine structure of the basic

constituents of matter requires energies generally exceeding GeV.

The use of high energy in accelerators are needed for another reason, namely to create the elementary particles artificially in the laboratory since most of them do not exist as free particles in nature. The $E = mc^2$ relationship governs the collision energy E required to produce a particle of mass m . Many elementary particles are so heavy that collision energies of several GeV are needed to create them. In fact, the key to understanding the origins of many parameters, including the masses of the known particles and to develop consistent theory required collision energies in the trillion electron volt or TeV range.

Our progress in improving higher collision energy has indeed been remarkable which can be seen from the graph (Fig 1) originally created by Livingston in 1954. Since 1930 the energy has increased by about a factor of 10 every six to eight years. Such spectacular achievement has been possible from a succession of technologies rather than from construction of bigger and

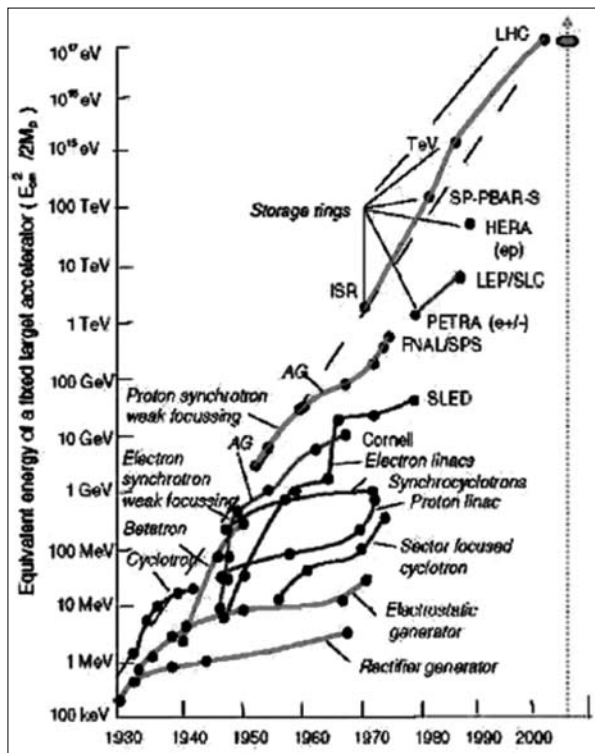


Fig 1 : A "Livingston plot" showing accelerator energy versus time, updated to include machines that came on line since 1930. The filled circles indicate new or upgraded accelerators of each type.

better machines of a given type. When any one technology reached saturation, a successor new technology usually has taken over.

However, the Livingston plot does not recognize another important parameter for an accelerator i.e, the intensity of the beam, or the number of particles accelerated per second. The probability of producing a reaction when the beam strikes a target is given by a number called the cross section, which is the effective area a target particle poses for that reaction to occur. The overall reaction rate is then the product of the beam intensity, the density of target particles, the cross section of the reaction under investigation, and the length of target material the incident particle penetrates. If scientists are to collect data that have sufficient statistical accuracy to draw meaningful conclusions this rate and hence the intensity of the beam should be reasonable. Another important parameter of an accelerator is the duty cycle, the measure of the percentage of time the beam is actually on.

In general, the number of possible reactions increases with increase in energy. Therefore the discriminating power of detectors and the data-analysis system also has to improve to recognize the "wheat" from the "chaff." It is obvious that with energy increase as indicated by the Livingston plot, there had to be a parallel development in the analyzing potential of the equipment.

And finally the economy counts: even if a planned accelerator is technically capable of providing the needed energy, intensity, duty cycle, and low background, it still must be affordable and operable. This overarching issue of costs that dictate the answer to the question, how large can accelerators and colliders become, and what energy can they attain? The relationship of size and cost of the facility with energy is dictated by a set of relations known as scaling laws. With classical electrostatic accelerators and radiofrequency linear accelerators, the scaling laws imply that the costs and other resources required should grow about linearly with energy. However, new physical phenomena will cause the costs eventually to rise more steeply with energy. Several breakthroughs like invention of phase stability in 1945 and strong focusing in 1952 made it possible to squeeze beams in linear and circular accelerators to much tighter dimensions, thus reducing magnetic field volumes and therefore costs. But still fundamental question remains : "To what extent is society willing to support tools for particle physics even if the growth of cost with energy is 'only' linear?" Therefore we must develop new technologies to make accelerators more compact and more economical.

Quest for Smaller and Cheaper

Huge particle colliders, like Large Hadron Collider (LHC) at CERN, are currently the crown jewel of colliders which is a 27-km-circumference ring for accelerating and storing counter circulating beams of 7-TeV protons and has a stored beam energy exceeding 300 MJ. The collider's design luminosity (collision rate per unit scattering cross section) of $10^{34} \text{ s}^{-1} \text{ cm}^{-2}$ is two orders of magnitude better than that of its immediate predecessor, the Tevatron collider at Fermilab.

However, smaller accelerators lie at the heart of many scientific and medical applications. These include synchrotrons and free-electron lasers, which convert beams of energetic electrons into radiation ranging from terahertz radiation to X-rays, and neutron-beam facilities, which are driven by accelerated proton beams. Accelerators probe matter in all its states, enabling advances in engineering, medicine, and the biological and physical sciences. They also have widespread applications in medicine, ranging from X-ray diagnostics to particle-beam therapy. The Linac Coherent Light Source (LCLS) at SLAC, for example, is powered by a high-quality beam of 14-GeV electrons from a kilometer-long segment of the laboratory's venerable two mile linear accelerator. The e-beam generates subpicosecond bursts of coherent 8-keV x rays after traveling through a 100-m-long undulator.

Virtually all of today's machines accelerate charged particles in the electric fields generated between conducting electrodes or excited in an electromagnetic cavity. In this approach, electrical breakdown limits the maximum field to less than 100 MV m^{-1} . In contrast, plasma accelerators can generate 1,000-times greater accelerating fields, reducing the required accelerator length by the same factor. This vibrant research area is driven by the prospect of shrinking kilometre-scale particle colliders to a few metres and of reducing hundreds of metres long accelerators in synchrotrons to a few centimetres (Fig 2 & 3).

With this brief overview the present article will outline the physics of laser-driven plasma accelerators and discuss some of the key developments in this field. We also consider some of their potential applications and discuss the challenges that must be overcome before these applications can be realized. It may be noted that electric fields excited in plasmas by laser pulses have been used to accelerate positive ions, protons and electrons as well. However, we will concentrate on laser-driven acceleration of electrons, but despite this focus, the account presented here is far from comprehensive.

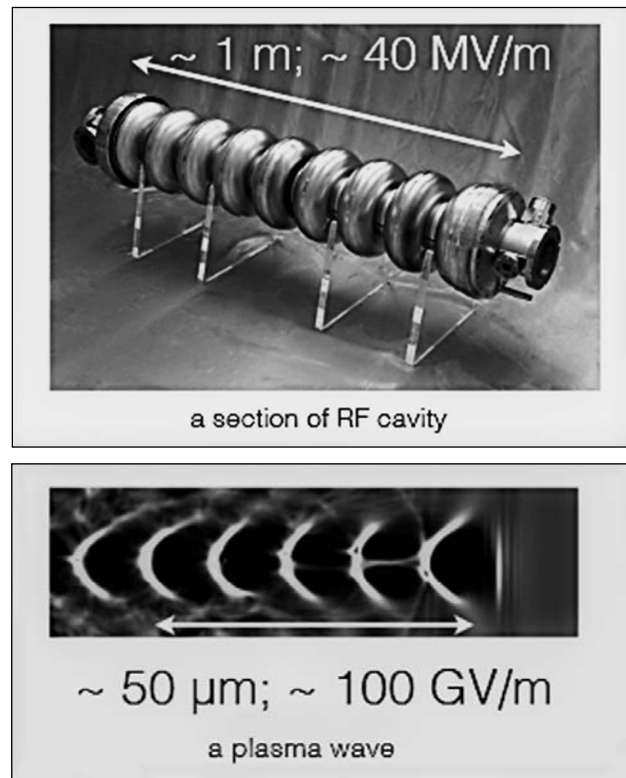


Fig 2 : Pictorial representation of RF cavity and Plasma wave



Fig 3: A section of the first linear electron accelerator, which operated at Stanford University in 1947. Eventually 3.6 m long, it could accelerate electrons to an energy of 6 MeV. (Courtesy Stanford University)

Key concepts

When an intense laser pulse propagates through a plasma (in simple terms, an ionized gas), the free electrons in the plasma are pushed

away from the laser pulse by the ponderomotive force. These electrons are pulled back towards their original positions by the positive ions, but their momentum causes them to overshoot and subsequently to oscillate about their initial position. The separation of electrons and ions forced by the laser pulse hence excites a longitudinal electron density wave - known as a 'plasma wakefield' - which trails the driving laser pulse in a similar fashion to the water wake following a moving boat.

The genesis of plasma accelerators was the pioneering 1979 paper by Tajima and Dawson in which they suggested that the strong electric fields formed within laser-driven plasma waves could accelerate charged particles to relativistic energies. The ability of plasmas to support very large electric fields was shown in the 1980s by Joshi's group at UCLA. Experiments in plasma wakefield acceleration were undertaken with the advent of sufficiently short duration and high power laser pulses. Credit goes to the development of the technique called 'chirped pulse amplification' (CPA). The field witnessed a major milestone in the early 2000s as high-power (~10 TW) femtosecond laser pulses, using titanium sapphire laser systems, became available. In 2004 three independent groups at Imperial College (UK), Lawrence Berkeley National Laboratory (USA), and Laboratoire d'Optique Appliquée (France) demonstrate that under the right conditions, they can produce e-beams with a narrow spread of final energies. The driving lasers in these experiments were Ti:sapphire CPA systems delivering laser pulses with an energy in the range 0.5–1 J and a duration 33–55 fs. The targets were supersonic H₂ or He gas jets, ionized by the driving laser pulse to give fully ionized plasmas of density $n_e \approx 2 \times 10^{19} \text{ cm}^{-3}$. The electron beams produced by these ~10 TW lasers had energies of ~100 MeV in a plasma structure only ~1 mm long.

The plasma oscillates at its characteristic frequency, the plasma frequency, given (in angular units) by $\omega_p = ((n_e \times e^2) / (m_e \times \epsilon_0))^{1/2}$, where n_e is the initial electron density, ϵ_0 is the vacuum permittivity and m_e and e^- are respectively the mass and charge of an electron.

The electrons are kicked forwards and backwards respectively by the front and back of the laser pulse, and hence the wakefield will be strongest when these kicks add in phase - that is, if the laser pulse duration τ satisfies $\omega_p \tau \approx 1$.

The separation of electrons and ions in the plasma wave sets up huge electric fields, which can be used to accelerate charged particles. Importantly, as the wakefield propagates at the speed of the laser pulse, it can be used to accelerate particles to relativistic energies. The magnitude of the electric field in a plasma wave can reach the order of the 'cold wave-breaking limit', namely $E_{wb} = (m_e \times c \times \omega_p) / e$. For example, for a plasma density with $n_e = 1 \times 10^{18} \text{ cm}^{-3}$, we find $\omega_p = 5.6 \times 10^{13} \text{ rad s}^{-1}$ and $E_{wb} = 96 \text{ GeV m}^{-1}$; the plasma period $T_p = 2\pi / \omega_p \approx 110 \text{ fs}$, and thus resonant excitation requires laser pulses with durations somewhat shorter than 100 fs.

The wakefield is driven by the ponderomotive force, which is the time-averaged force experienced by a charged particle as it moves in the fields of an electromagnetic pulse. One way of seeing how this force arises is to consider the mean kinetic energy of an electron oscillating in the laser field. The electron's ponderomotive energy U_p is proportional to the laser intensity I . Spatial variations in the laser intensity, and hence in U_p , correspond to the ponderomotive force $F_p = -\nabla U_p \propto -\nabla I$. It acts to push electrons away from regions of high gradients in the laser intensity.

A fundamental limit to the distance over which particles can be accelerated arises from the fact that the plasma wave travels at the speed of the laser pulse - which is less than the speed of light in vacuum c - whereas the accelerated particles reach speeds very close to c . In the linear regime, particles move from a region of acceleration to one of deceleration after the dephasing length $L_d \approx \lambda_p^3 / \lambda^2$, where $\lambda_p \approx 2\pi c / \omega_p$ and λ are the wavelengths of the plasma wave and the driving laser, respectively. For an 800-nm laser pulse propagating in a plasma with $n_e = 10^{18} \text{ cm}^{-3}$, L_d is about 60 mm. Other limitations arise from defocusing of the pump laser beam and depletion of the driving laser energy through transfer to the plasma wave.

The electrons which are to be accelerated can either be injected into the plasma wave or they can be pulled out of the target plasma. At low laser intensities, the wakefield has a low amplitude, and consequently the plasma electrons cannot gain sufficient momentum to become 'trapped' in the plasma wave. In this regime, for the electrons to become trapped, they have to be injected into the plasma wave with a sufficiently high initial energy (just as a surfer has to swim fast enough to catch a wave). For very intense laser pulses, however, the plasma waves are highly nonlinear,

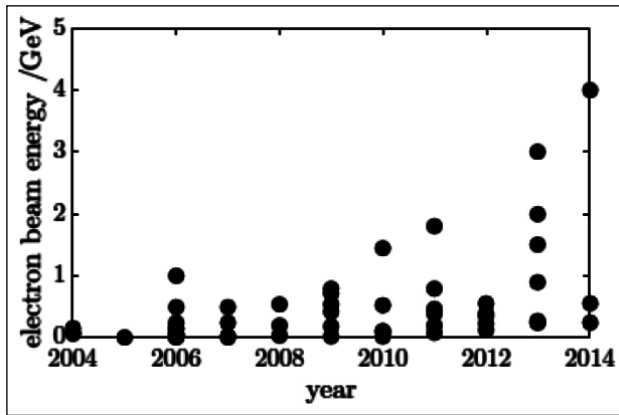


Fig 4 : The progress in the maximum beam energy in laser wakefield accelerator experiments

and some of the background plasma electrons can be trapped and accelerated. This simplifies the generation of an electron beam, but at the cost of reduced control.

Let us now examine how the maximum achievable beam energy has progressed over the last decade using a set of results from published literature which also reveal some of the physics behind this phenomena. The progress in the maximum beam energy in laser wakefield accelerator experiments has been quick as shown in Fig. 4 with 0.2 GeV beam energy reported in 2002 to the current value of 4 GeV from the group at the Lawrence Berkeley National Laboratory achieved in 2014. The inter relationship of various parameters like beam energy, laser power, plasma density and accelerator length are depicted in Fig 5 & 6. However, it may be noted that this exercise is only representative and by no means an exhaustive list of all published experiments in plasma wakefield accelerators.

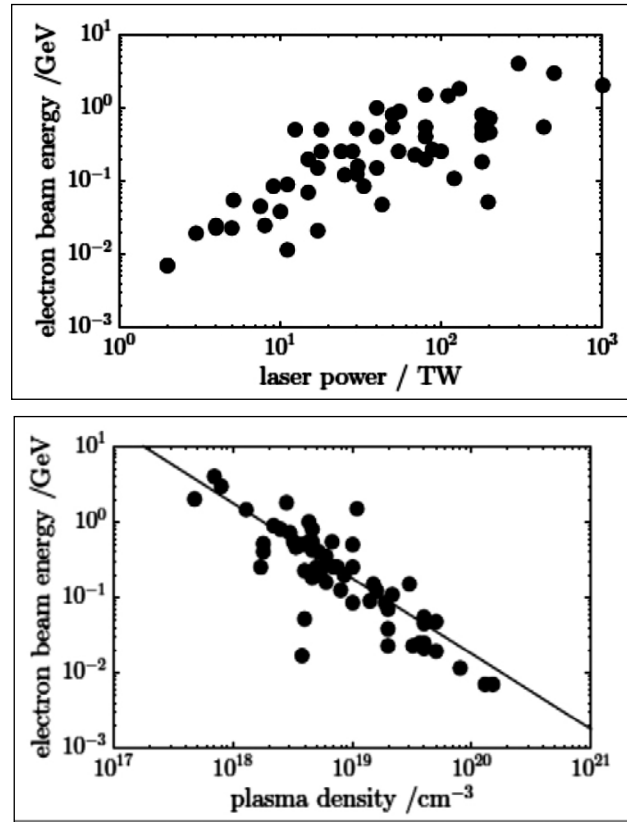


Fig 5 : Variation of electron beam energy with laser power and plasma density respectively reported from various experiments

Application areas

Potential applications of particle or radiation beams generated by laser-driven plasma accelerators include radiography for non-destructive inspection of materials or diagnosis, radiotherapy, ultrafast pulse radiolysis studies in biology and chemistry, ultrafast studies of condensed matter and areas of fundamental research such as 'plasma quantum electrodynamics' and particle physics.

Laser plasma accelerators are well suited for driving compact sources of radiation. Radiation has been generated at visible and soft-X-ray wavelengths by passing laser-accelerated electrons through magnetic undulators (Figure 7). Fuchs et al. could generate 17 nm and 9 nm radiation (the fundamental and second harmonic, respectively) by passing 200 MeV electrons through a compact (30-cm-long) magnetic undulator, with an estimated peak brilliance of 1.3×10^{17} photons s^{-1} mm^{-2} $0.1\% \text{ BW}^{-1}$ at 17 nm.

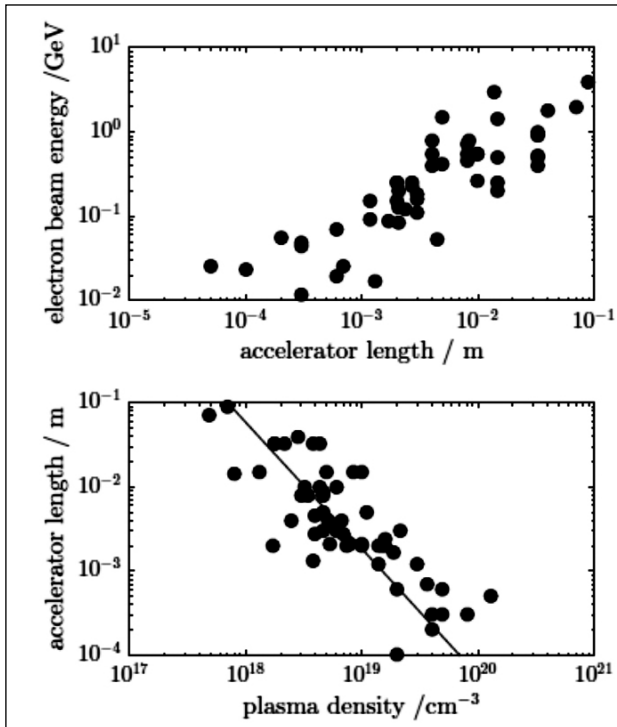


Fig 6: Variation of reported electron beam energy with accelerator length (Top). Relationship between operating plasma density and accelerator length (Bottom).

Bright radiation is also emitted directly from a plasma accelerator as a result of the accelerating electron bunch being oscillated by the transverse electric field of the plasma wakefield. These betatron oscillations generate broadband radiation at very short wavelengths. For example, Kneip et al. have measured the betatron spectrum emitted by a 250-MeV plasma accelerator, and showed that emission occurs in the 1–100 keV range with a peak brilliance of 1×10^{22} at photon energies of 10 keV. The small source size, typically a few micrometres, has allowed X-ray phase-contrast imaging of biological specimens.

In a free-electron laser, positive feedback between an electron bunch and the radiation it generates as it passes through an undulator causes exponential growth of the radiation intensity via ‘microbunching’ of the electrons. Free-electron lasers require very high quality electron bunches, making it challenging to replace the kilometre-scale conventional accelerators of existing X-ray free-electron lasers with plasma accelerators.

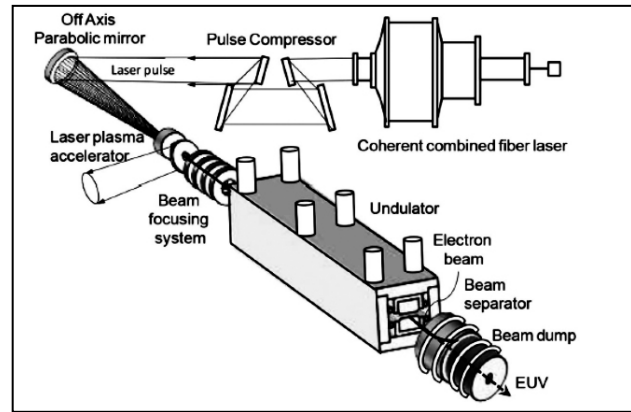


Fig 7: A schematic illustration for the EUV light source based on a compact Free-Electron-Laser-driven by a fibre laser-based plasma accelerator [From Nat. Photon., 7 (2013) 258]

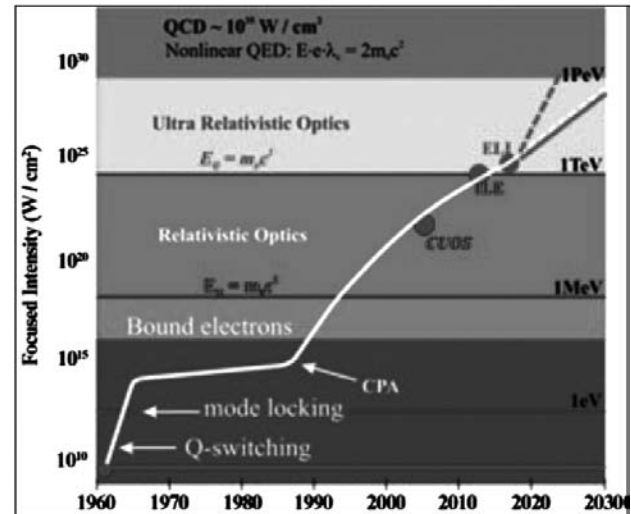


Fig 8: The progress laser intensity achieved over the years. A shortcut (dotted red line) toward EUV and ultrahigh intensities. [revised from Phys. Rev. Lett., 107 (2011) 45003]

Grüner et al. have considered the design of a free-electron laser operating at 0.25 nm driven by a laser-accelerated 1.7-GeV, 1.6-nC, 10-fs electron bunch. Recent work has shown that the requirements on the electron-bunch parameters can be relaxed by employing tailored undulator designs.

In the long run, plasma accelerators could replace the conventional accelerators; however, the requirements of laser and plasma target for a laser-driven TeV collider are daunting. For example, Nakajima et al. have considered

a two-stage plasma accelerator with a plasma stage length of 333 m driven by 10.4-kJ, 950-fs laser pulses with a repetition rate of 880 Hz; this corresponds to a mean laser power of 9.2 MW. An alternative design by Schroeder et al comprises a 50-stage linac in which each stage is driven by 32-J, 56-fs laser pulses with a pulse repetition rate of 15 kHz - that is, a mean laser power per stage of 480 kW.

New frontiers: Exawatts and zeptoseconds

We have seen that the introduction of the idea of LPA and the advent of the CPA reinforced each other to usher in high-field science. Now we envision that these two fundamental ideas are even more intertwined and opening a new accelerated progress. For example, the ever-increasing laser intensity as seen in Fig. 8 may rise even faster, as these two powerful ideas generate even more and newer applications. Previously, the path toward EW seems to take ever higher energy of laser such as MJ lasers. Now a new vista appears to arise with the new compression technique and its application to new accelerating

media for LPA. These new tools are so new that we cannot foresee their full implications. However, we could make a tentative but bold anticipation. For example, the zeptosecond X-ray laser matches very well with nuclear physics, while fs fits well with chemistry and atomic physics investigations. We also anticipate that instead of larger machines and higher energies, these developments tend to strive for shorter machines and more intensity, more compact accelerators and other applications devices. These anticipated developments should also be conducive to arrive at societally useful applications.

Evidences over more than 18 orders of magnitude of the Pulse Intensity-Duration Conjecture have been accumulated experimentally and with simulation (Fig 9). It shows that the pulse duration goes inversely with the intensity from the millisecond to the attosecond and zeptosecond, using values from experiments and simulation. Most notably it predicts that the shortest coherent pulse in the zeptosecond-yoctosecond regime should be produced by the largest laser, like ELI or NIF and the Megajoule, if they are reconfigured in femtosecond pulse systems. This conjecture may provide an invaluable guide for future ultra-intense and short-pulse experiments. It fosters the hope that zeptosecond and perhaps yoctosecond pulses could be produced using kJ-MJ systems. It will then open up the possibility to take snapshots of nuclear reactions and to peek into the nuclear interior in the same way that Zewail examined chemical reactions or Corkum and Krausz probed atoms. The other exciting prospect is the possibility to study the nonlinear optical properties of vacuum. This conjecture ties the three distinct disciplines of science, i.e. ultrafast science, high field science, and large-energy laser science together in a single stroke.

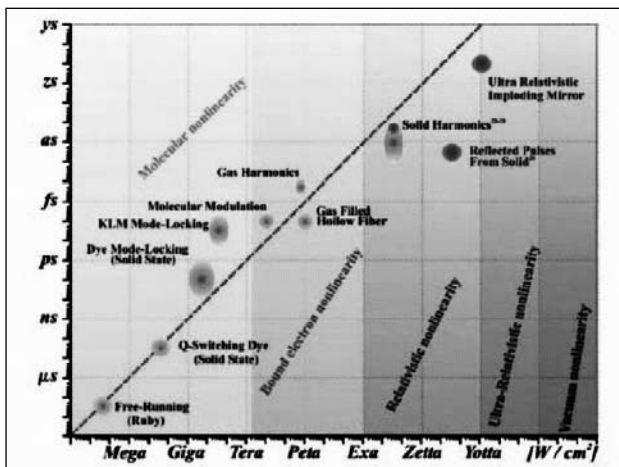


Fig 9: The Pulse Intensity-Duration Conjecture is shown. An inverse linear dependence exists between the pulse duration of coherent light emission and its intensity of the laser driver in the generation volume over 18 orders of magnitude. These entries encompass different underlying physical regimes, whose nonlinearities are arising from molecular, bound atomic electron, relativistic plasma, and ultra-relativistic, and further eventually from vacuum nature. The blue patches are from the experiments, while the red from the simulation or theory. [From Science, 331 (2011) 4146].

Acknowledgement

The author is thankful to many researchers in the field on whose work the article is based and apologies for not representing many other works. In addition the author would like to put on record his special thanks to Bhabha Atomic Research Centre for continuing support.

Suggested Reading

1. Laser acceleration
T. Tajima, K. Nakajima and G. Mourou
Rivista Del Nuovo Cimento, 40, 33 - 133 (2017)
2. Pune University Linear Electron Accelerator based Pulse Radiolysis facility probing Radiation – Matter Interaction
S.K.Sarkar, Geeta Sharma and Avinash S.Kumbhar
ISRAPS Bulletin, 28, 17-30 (2016)
3. Nanoscience and engineering by ionizing radiations
D. K. Avasthi, S. K. Sarkar, A. Tripathi
Advanced Material Letters 4, 385-389 (2013)
4. Coherent Control Technologies and its Applications
Ajay K. Singh and S. K. Sarkar
ISRAPS Bulletin, 21, 22-31 (2009)
5. Laser enrichment of isotopes
V. Parthasarathy, P.N. Bajaj , S. K. Sarkar
Lasers in Chemistry, Ed. Maximilian Lackner, Wiley-VCH Pub (2007).
6. Free-electron lasers
Srinivas Krishnagopal, Vinit Kumar, Sudipta Maiti, S. S. Prabhu and S. K. Sarkar
Current Science 87, 1066 (2004)
7. FEL photochemistry: current developments and future prospects.
S. K. Sarkar, Proc. Indian Natl. Sci. Acad., Part A, 66, 71-106 (2000)



Dr. Sisir K. Sarkar, Outstanding Scientist of DAE served as Director, Chemistry Group and Head, Radiation & Photochemistry Division, Bhabha Atomic Research Centre. He did his post-doctoral work in the area of chemical dynamics at Columbia University, USA.

He has been to various laboratories in USA, Russia, Europe and Japan as visiting scientist and worked with various laser systems including Free Electron Laser. He has more than 400 papers in International journals, symposia and conferences to his credit. He is Fellow of Maharashtra Academy of Sciences. He served as President of Indian Laser Association (ILA) and Society for Material Chemistry (SMC) and Vice-President of Indian Society of Radiation & Photochemical Sciences (ISRAPS). He has been passionately involved till date in Radiation and Photochemical research using lasers and accelerators. He was Raja Ramanna Fellow of DAE associated with National Centre for Free Radical Research (NCFRR), Pune and presently Hon. Professor in the Chemistry Department of Savitribai Phule Pune University.

Radiation Processing: A non-thermal technology for food preservation

Sunil K. Ghosh

Food Technology Division, Bhabha Atomic Research Centre, Trombay, Mumbai, India

Email: ghsunil@barc.gov.in

Introduction

Ensuring food security and safety is of paramount importance in the challenging scenario of global climate change and unpredictable weather. Preservation of food is a prrs are slowly becoming aware of the importance of food safety and regulators are becoming more stringent. Besides, pee-requisite to achieve this goal. Post-harvest losses in food and agricultural commodities especially in India have been estimated to be between 30-40 per cent, valued at thousands of crores of rupees. This is due to poor infrastructure in the country to preserve them. These losses are primarily due to insect infestation, microbiological contamination and physiological changes as a result of sprouting, ripening and senescence. Cold storage, fumigation and drying are conventionally employed for prevention of post-harvest losses. Consumer-capita income is growing and people are becoming increasingly health consciousness. As a result, to avoid food-borne diseases, consumers now demand for safe, fresh, quality and additivefree foods. Also, a large group of consumers are tilted for minimally processed ready-to-cook (RTC) and ready-to-eat (RTE) food products. As these products are processed/handled by several stages, chances of contamination by microorganism increases. The hot and humid climate is also favourable for the growth of numerous insects and microorganisms which destroy stored crops and cause spoilage of food.

Thermal treatment is the conventional way for food processing/preservation relies on by neutralizing foodborne insects, parasites, bacteria, fungus and virus or inactivation of the enzymes that degrade the food material. Although the thermal methods are very effective

for many foods, several of them are not suitable for thermal processing because they lose fresh like character or some of the pathogenic organisms are resistant to thermal treatment. Non-thermal processing which takes care of microbial safety, retain freshness, nutrients and sensory attributes are in demand by food industries. A few alternative to thermal processing methods [1-6] are now under active consideration by industries. Ionizing radiations [3] such as X-rays, gamma rays and electron beam are gaining importance as an alternative to thermal processing. This processing method has the ability to inactivate microorganisms at near-ambient temperatures avoiding thermal degradation of the food components. Radiation processing by ionizing radiation brings about minimal changes in sensory qualities thereby maintaining food quality. This article provides an overview of the use of ionizing radiation especially the use of γ -ray as non-thermal technology that is effective alternative or complementary to thermal techniques to maintain safety and quality of the food.

Preservation of food by ionizing radiation

Particulate radiation such as electron beam (EB) and electromagnetic radiations like X-ray and γ -ray are used for food irradiation. The EB and X-ray are machine generated while γ -ray are obtained from radioactive isotopes namely Cobalt-60 and Caesium-137, They are called ionizing radiations because they can ionize the medium through which they pass. Radiation processing of food provides mechanism to control these food losses significantly [7]. It involves controlled application of energy from ionizing

Introduction

Ensuring food security and safety is of paramount importance in the challenging scenario of global climate change and unpredictable weather. Preservation of food is a prrs are slowly becoming aware of the importance of food safety and regulators are becoming more stringent. Besides, pee-requisite to achieve this goal. Post-harvest losses in food and agricultural commodities especially in India have been estimated to be between 30-40 per cent, valued at thousands of crores of rupees. This is due to poor infrastructure in the country to preserve them. These losses are primarily due to insect infestation, microbiological contamination and physiological changes as a result of sprouting, ripening and senescence. Cold storage, fumigation and drying are conventionally employed for prevention of post-harvest losses. Consumer-capita income is growing and people are becoming increasingly health consciousness. As a result, to avoid food-borne diseases, consumers now demand for

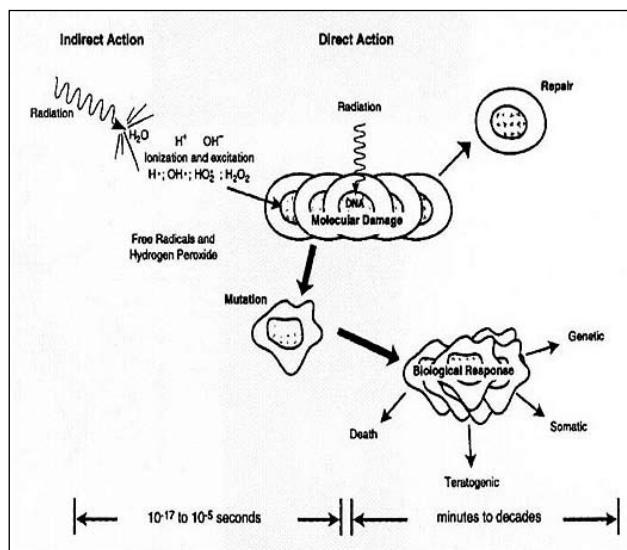


Fig. 1 Effect of ionizing radiation on living cell

safe, fresh, quality and additivefree foods. Also, a large group of consumers are tilted for znizing radiation especially the use of γ -ray as non-thermal technology that is effective alternative or complementary to thermal techniques to maintain safety and quality of the food.

Preservation of food by ionizing radiation

Particulate radiation such as electron beam (EB) and electromagnetic radiations like X-ray and γ -ray are used for food irradiation. The EB and X-ray are machine generated while γ -ray are obtained from radioactive isotopes namely Cobalt-60 and Caesium-137, They are called ionizing radiations because they can ionize the medium through which they pass. Radiation processing of food provides mechanism to control these food losses significantly [7]. It involves controlled application of energy from ionizing radiations using radioisotopes (0.66-1.33 MeV), electron beam (upto 10 MeV) and X-rays (upto 5 MeV). The energy of these radiations are below the threshold limit to destabilize the nucleus of the elements present in food materials. The dose of radiation is measured in unit called gray (Gy) which is equivalent to 1 Joule of absorbed energy per kilogram of material. Irradiation can directly interact with the biologicals molecules or indirectly by interacting with water present in food material to produce first the radiolytic

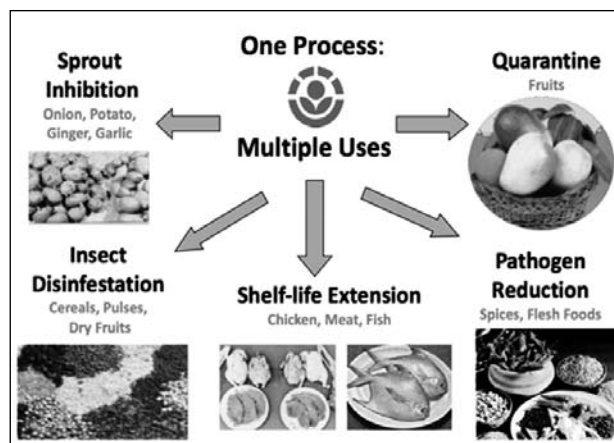


Fig. 2 Multiple applications of radiation processing for preservation of various foods

products like highly reactive hydrogen, hydroxyl and superoxide radicals and molecular species like H_2O_2 . Irradiation thus works directly or indirectly by disrupting the biological processes such as deactivation of enzymes in the food material that lead to decay. Similarly, these radiolytic species can cause the damage (see, Fig. 1) in the cell of

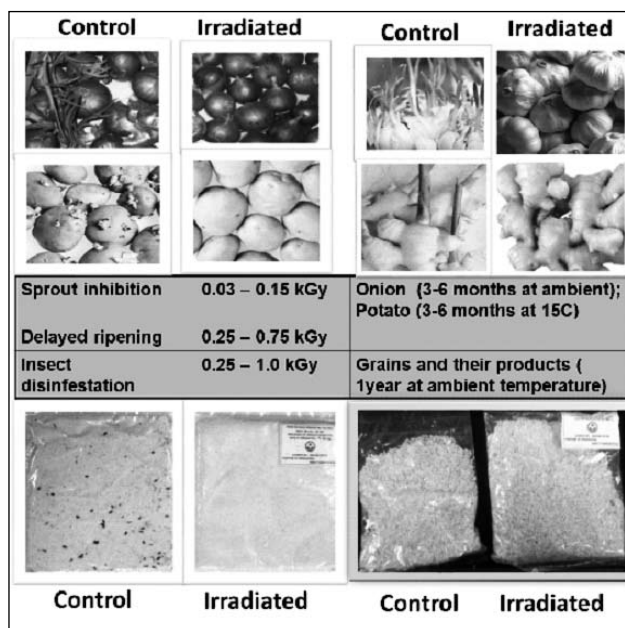


Fig. 3 Radiation processing of agricultural produce

the insects and microorganism present in the food leading to their elimination. The reactions with DNA cause the death of microorganisms and insects and impair the ability of potato and onion to sprout.

Radiation processing technology can provide an effective alternative to fumigants that are being phased out due to their adverse effects on environment and human health. Radiation processing is a single process but multiple applications (see, Fig. 2). The treatment helps in inhibition of sprouting of tubers and bulbs, disinfestations of insect pests in agricultural commodities, delay in ripening and senescence of fruits and vegetables, destruction of microbes responsible for spoilage, and elimination of pathogens and parasites (see, Fig. 3) [8]. The applications of gamma radiation processing of the food have been classified in three broad categories, viz. Low dose applications (0.25-1 kGy) which serve purpose of sprout inhibition in bulbs and tubers, insect disinfestations in grains and delayed ripening of climacteric fruits; Medium dose applications (1-10 kGy) for microbial decontamination and destruction of pathogenic

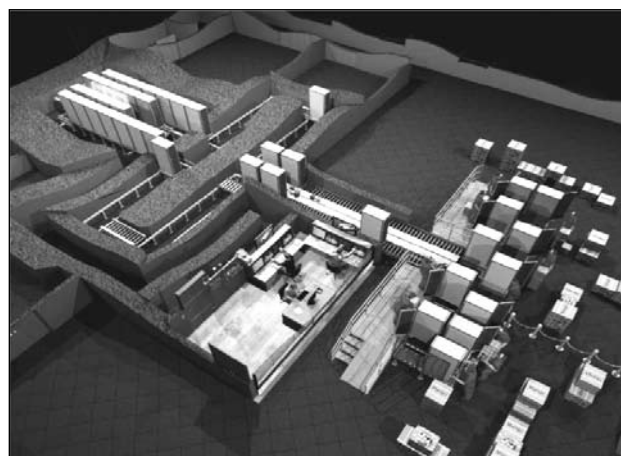


Fig. 4 Schematic view of a radiation processing plant for food

microorganisms in different food commodities and high dose applications for sterilization of food products. The technology can be used for extending shelf-life under recommended conditions of storage, ensuring microbiological safety and in overcoming quarantine barriers to international trade. Radiation processing can also be used for hygienization and sterilization of non-food items including cut-flowers, pet food, cattle feed, aqua feed, ayurvedic herbs and medicines and packaging materials.

Radiation processing of food is carried out in an irradiation chamber (see, Fig. 4) shielded by concrete walls of 1.5-1.8 m thickness. Food, either pre-packed or in bulk in suitable containers is sent into the irradiation chamber on an automatic



Fig. 5 Radura symbol for labelling of radiation processed food

conveyor that goes through a concrete wall labyrinth to prevent radiation from reaching the work area and operator room. The radiation sources Cobalt-60 or Caesium-137 is stored under 6 m deep water when the facility is not in use. The water shield does not allow radiation to escape into the irradiation chamber, thus permitting free access for personnel to carry out plant maintenance. For the irradiation of food, the source is brought to the irradiation position above the water level after activation of all safety devices and restricting human entry. The goods in carriers or tote boxes are mechanically sent inside, positioned around the source rack and turned around their own axis, so that the contents are irradiated on both sides. The absorbed dose is determined by the residence time of the carrier or tote box in the irradiation position [9]. The absorbed dose is checked by placing the dosimeters at various positions in a tote box or carrier.

The process is highly effective, non-residue forming, safe to workers & environment, can be applied to pre-packed commodities, can penetrate deeper into tissues and is a cold process. Radiation processing of food has been thoroughly and extensively studied in order to ensure its toxicological, nutritional and microbiological safety. However, all commodities may not be amenable to radiation processing. The technology is capital intensive. Besides negative consumer perception has resulted in slow progress in acceptance of this technology.

Regulation requires that every food commodity irradiated should be labelled. Label should indicate treatment given along with an international logo known as Radura symbol (Figure 5). Label statements are used to provide information on why the product is irradiated and it gives consumers an opportunity to choose. Several market trials have demonstrated consumer's preference towards irradiated foods when positively informed about the technology.

Like conventional processes, radiation processing has advantages and limitations. There are a number of additional advantages when it comes to radiation processing for sterilization of certain commodities. Gamma radiation has high penetrative power and hence can penetrate deeper into tissues. No area of the product or packaging is left untreated. The materials can be treated in pre-packed conditions. Therefore, no chances of recontamination happen unless the packaging is opened. It is highly effective, non-residue forming and safe to workers & environments. Being a cold process, loss in volatile constituents is not significant [10]. The primary limitations are that all commodities may not be amenable to the process, capital intensive, difficult to detect the treatment and reluctance by both the industry and consumer in adopting the technology.

Irradiation causes negligible changes in chemical composition of the food product since it does not substantially raise the temperature of food during processing. Negligible changes in proteins, fats and carbohydrates are noted even at doses above 10 kGy. Essential amino acids, essential fatty acids, minerals and trace elements are also unaffected. There can be a decrease in certain vitamins (particularly thiamine and vitamin C) but these are of the same order of magnitude as that observed with other preservation methods such as drying or canning (thermal sterilization). In fact, increased antioxidant potential in fruits and vegetables as a result of radiation processing has been reported. Irradiated foods are thus safe for consumption and are nutritionally adequate and wholesome.

Worldwide research over last five decades has adequately demonstrated the safety of irradiated food. Independent technical and scientific committees constituted by several countries including Canada, Denmark, France, India, Sweden, UK, European Union and USFDA have declared that radiation processed food is safe for human consumption. Presently, radiation processing is practiced in sixty countries for over

Table – IA: Classes of Food Products and Dose Limits for Radiation Processing

Class	Food	Purpose	Dose limit Minimum	(kilo Gray) Maximum
Class 1	Bulbs, stem and root tubers, and rhizomes	Inhibit sprouting	0.02	0.2
Class 2	Fresh fruits and vegetables (other than Class 1)	Delay ripening	0.2	1.0
		Insect disinfestation	0.2	1.0
		Shelf-life extension	1.0	2.5
		Quarantine application	0.1	1.0
Class 3	Cereals and their milled products, pulses and their milled products, nuts, oil seeds, dried fruits and their products	Insect disinfestation	0.25	1.0
		Reduction of microbial load	1.5	5.0
Class 4	Fish, aquaculture, seafood and their products (fresh or frozen) and crustaceans	Elimination of pathogenic microorganisms	1.0	7.0
		Shelf-life extension	1.0	3.0
		Control of human parasites	0.3	2.0
Class 5	Meat and meat products including poultry (fresh and frozen) and eggs	Elimination of pathogenic microorganisms	1.0	7.0
		Shelf-life extension	1.0	3.0
		Control of human parasites	0.3	2.0
Class 6	Dry vegetables, seasonings, spices, condiments, dry herbs and their products, tea, coffee, cocoa and plant products	Microbial decontamination	6.0	14.0
		Insect disinfestation	0.3	1.0
Class 7	Dried foods of animal origin and their products	Insect disinfestation	0.3	1.0
		Control of moulds	1.0	3.0
		Elimination of pathogenic microorganisms	2.0	7.0
Class 8	Ethnic foods, military rations, space foods, ready-to-eat, ready-to-cook/ minimally processed foods	Quarantine application	0.25	1
		Reduction of microorganisms	2	10
		Sterilization	5	25

100 food items. International trade in radiation processed food stuffs has increased considerably in the last two decades.

In India, the Food Package Irradiator, commissioned in 1967, was India's first pilot plant radiation processing facility that could

process commodities right from onion and potato requiring very low dose (< 1 kGy) to spices requiring very high doses (6-14 kGy). Based on large scale studies in this facility, approval was sought from Indian government for formulating a policy that governs food irradiation in India.

Table – IB: Dose Limits for Radiation Processing of Allied Products

Sl. No.	Allied Product	Purpose	Dose Limit kGy (kiloGray)	
			Minimum	Maximum
1	2	3	4	5
1.	Packaging materials for food or allied products	Microbial decontamination	5.0	10.0
		Sterilization	10.0	25.0
2.	Food additives	Insect disinfestation	0.25	1.0
		Microbial decontamination	5.0	10.0
		Sterilization	10.0	25.0
3.	Health foods, dietary supplements and nutraceuticals	Insect disinfestation	0.25	1.0
		Microbial decontamination	5.0	10.0
		Sterilization	10.0	25.0

A National Monitoring Agency (NMA) was set up by Government of India in 1987 to oversee commercial application of radiation processing technology. In 1991 Atomic Energy (Control of Irradiation of Food) rules were notified, later amended in 1996. In 1994 Government of India amended Prevention of Food Adulteration Act (1954) Rules and approved irradiation of onion, potato and spices for domestic market. Additional items were approved in April 1998 and in May 2001. In 2007 the Directorate General of Health Services (PFA) issued a draft notification for generic or food class-wise approval of radiation processing. In February 2004, Ministry of Agriculture, Government of India, amended plant protection and quarantine regulations to include irradiation as a quarantine measure. The Atomic Energy (Control of Irradiation of Food) rule 1996, the primary legislation that regulates food irradiation was amended and the notification issued recently in June 2012. An amended draft notification relating to the Prevention of Food Adulteration Act (Fifth Amendment) rules,

Table II: Year-wise quantity of mango irradiated for export purposes

Year of Export	Mango Quantity (MT)
2007	157
2008	300
2009	121
2010	95
2011	84
2012	210
2013	281
2014	295
2015	329
2016	750
2017	1150
2018	1200

1994 was also issued by the Ministry of Health and Family Welfare. The rules governing food irradiation has also been put in place with the notification of the Atomic Energy, (Irradiation of food and allied products rules) 2012 and adoption by FSSAI (Tables IA & B). A generic class-based

Table III: Radiation processing plants in India

Sr. No.	Name Of The Plant	Purpose	Status / Remarks
1	Radiation Processing Plant, BRIT, Vashi, Navi Mumbai – 400075	Food and allied products	Commissioned in 2000
2	KRUSHAK Irradiator, Lasalgaon, Nashik – 411037, Maharashtra	Food Products	Commissioned in 2002
3	M/S Organic Green Foods Ltd., Dankuni, Kolkata, West Bengal	Food, Packaging & Medical Products	Commissioned in 2004
4	M/S A.V. Processors Pvt. Ltd., Ambernath (E), Thane, Maharashtra	Food & Medical Products	Commissioned in 2005
5	M/S Universal Medicap Ltd., Vadodara, Gujarat	Food & Medical Products	Commissioned in 2005
6	M/S. Microtrol, Bangalore, Karnataka	Food & Medical Products	Commissioned in 2006
7	M/S Agrosurg Irradiators, Vasai, Thane, Maharashtra	Food, Packaging & Medical Products	Commissioned in 2008.
8	M/S Gamma Agro Medical Processing, Hyderabad, Telangana	Food & Medical Products	Commissioned in 2008.
9	M/S Jhunsons Chemicals Pvt Ltd., Bhiwadi, Rajasthan	Agro, Medical & Packaging Products	Commissioned in 2010
10	M/S InnovaAgri Bio Park Ltd., Malur, Dist. Kolar, Karnataka	Food & Medical Products	Commissioned in 2011
11	M/S Hindustan Agro Co-Operative Ltd., Rahuri, Ahmednagar, Maharashtra	Onion & Other Agricultural Produces	Commissioned in 2012
12	M/S Impartial Agro Tech (P) Ltd., Unnao, Lucknow, Uttar Pradesh	Food & Medical Products	Commissioned in 2014
13	M/S Gujarat Agro Industries Corp. Ltd, Bavla, Ahmedabad, Gujarat	Food Products	Commissioned in 2014
14	M/s Aligned Industries, Dharuhera, Rewari, Haryana	Food Products	Commissioned in 2015
15	Maharashtra State Agricultural Mktg. Board, Navi Mumbai, Maharashtra	Food Products	Commissioned in 2015

approval has been approved for increasing the product range for radiation processing. It will provide yearlong availability of feedstock for irradiation plants and improve their economic viability. Dried foods of animal origin and their products, ethnic foods, military rations, space foods, ready-to-eat/ready-to-cook minimally processed foods have also been included under this amendment.

The major facility in the government sector catering to irradiation of fresh horticultural produce is the KRUSHAK facility at Lasalgaon, Nashik district, Maharashtra state, India. The facility has been irradiating mangoes for export to USA since 2007[12] (Table II). A total of 3800 tons of mango has been irradiated and exported till 2017 in this facility. Feasibility of radiation as a phytosanitary treatment of other products

such as litchi, grapes and pomegranate has also been demonstrated. Radiation processing plant at Vashi, Navi Mumbai, under the Department of Atomic Energy, that has been processing spices and dry ingredients for microbial decontamination since 2000. In India currently 15 irradiation plants are functional which includes two plants set by Government of India and one each by Maharashtra government and Gujarat government (Table III). Volume of food irradiated in India has been steadily increasing. A total of more than 20,000 tons of produce is being irradiated annually in India.

Conclusion and future outlook

Many novel non-thermal technologies are still in their early stages of development. Irradiation is the only non-thermal method that has been granted the industrial status. Substantial progress has been achieved in the earlier periods on research and development and semi-commercial/pilot-scale processing and storage of irradiated foods. This has led to technology transfer activities, process control procedures and evaluation of public acceptance. Market survey and actual retail sales demonstrate that consumers are willing to pay a premium for food safety. Yet, today, consumers have no choice in the market place as the availability of irradiated foods in the retail market place is highly limited. As consumers and the food control authorities in developed as well as developing countries are becoming increasingly cautious on the question of food safety, food irradiation technology is expected to be applied commercially on a wider scale.

About one million ton of various food products have been processed across the globe in 2015. The technology is safe and its use alone can guarantee the safety of foods. Currently for setting up a commercial irradiation facility the estimated cost comes in the range of Rs. 15-20 crores excluding land cost. A 5-10% increase in cost is normally expected due to the radiation processing charges. But this additional expense is

nothing compared to the benefits it provides. The costs could be brought down in a multipurpose facility treating a variety of products around the year. Processing brings benefits to the consumers in terms of availability, storage life, distribution, and improved hygiene of food. Radiation processing will be moving fast to the status of a 'wonder technology' to satisfy the sanitary and phytosanitary requirements of the importing countries [13]. Effective combinations of radiation processing with more non-thermal preservation hurdles has great potential for improving the safety and quality of foods, retaining the freshness although many technological and regulatory barriers still need to be overcome before the food supply can receive these benefits.

Also, the capacity of India to penetrate and capture world market for processed foods depends on its ability to meet increasingly stringent food safety standards imposed in developed countries. Compliance with international food standards is a prerequisite to gain a higher share of world trade. Irradiation is an effective technology to resolve technical problems in trade of many food and agricultural products, either as a stand-alone technology or in combination with others. Authorization of food irradiation by groups/classes of food in accordance with the guidelines framed by the International Consultative Group on Food Irradiation (ICGFI) is a step in this direction.

As our economies become more global, food products must meet high standards of quality and quarantine in order to move across borders. Irradiation is an important tool in the fight to prevent the spread of deleterious insects and microorganisms. Further, increasing demand for food supplies to serve the needs of ever-increasing population and for improving the diets of the millions suffering from malnutrition, food irradiation technology could make a useful contribution to help alleviate world food problems.

References

1. G.V. Barbosa-Canovas, M. S. Tapia and M.P. Cano, Novel Food Processing Technologies; CRC Press, Florida (2005).
2. G. Tewari, and V. Juneja, Advances in thermal and non-thermal food preservation; Oxford, UK: Blackwell Publishing (2007).
3. J. Farkas and C. Moha'csi-Farkas, Trends in Food Science & Technology, 22 (2011), 121-126.
4. S. Toepfl, A. Mathys, V. Heinz, D. Knorr, Food Reviews International, 22 (2006), 405-423.
5. K. A. Taiwo, A. Angersbach and D. Knorr, Journal of Food Engineering, 52 (2002), 185-192.
6. G. Pataro, A. Munoz, I. Palgan, F. Noci, G. Ferrari and J. G. Lyng, Journal of Food Research International, 44 (2011), 1642-1648.
7. I. S. Arvanitoyannis, Irradiation of Food Commodities: Techniques, Applications, Detection, Legislation, Safety and Consumer Opinion; Elsevier, San Diego (2010).
8. X. Fan, B.A. Niemira and A. Prakash, Food Technol, 62 (2008), 191-204.
9. C. Oliveira, J. Salgado, M. L. Botelho, L. M. Ferreira, Journal of Radiation PhysioChemistry, 57 (2000), 666-670.
10. M. Alothman, R. Bhat and A.A. Karim, Trends in Food Sci Tech, 20 (2009), 36-43.
11. FAO/ IAEA/ WHO, Report of a Joint FAO IAEA WHO Study Group. Rome: Food and Agriculture Organization of the United Nations, (1999).
12. A. Sharma, BARC News Letter, 296 (2008) 2-8.
13. J. F. Diehl, Rad PhyChem, 63 (2002) 211-215.



Sunil Kumar Ghosh is serving as Outstanding Scientist and Head, Food Technology Division Bhabha Atomic Research Centre (BARC), Mumbai. He studied for his M.Sc. (1984) and Ph.D. (1989) under the supervision of Prof. Tarun K. Sarkar at the Indian Institute of Technology, Kharagpur. He carried out his postdoctoral studies with Prof. Ian Fleming, FRS, at the University of Cambridge, UK (1991-1993) and with Prof. Scott E. Denmark, FRS, at the University of Illinois, Urbana-Champaign, USA (1999-2001). His research interests are directed toward organosilicon chemistry, sulfur ylide mediated reactions, polyolefin synthesis, asymmetric synthesis of natural products, structural and mechanistic studies, asymmetric organocatalysis, synthesis of labeled compounds and the food chemistry.

Pulse Radiolysis Study of 4-Nitrophenol Reduction Reaction using Porous Platinum Nanoballs

G. K. Sharma^a and K. K. K. Sharma^b

^aNational Centre for Free Radical Research, Department of Chemistry,
Savitribai Phule Pune University, Ganeshkhind Pune-411007

^bSchool of Nanoscience and Technology, Shivaji University, Vidyanagar, Kolhapur-416004

Abstract

The use of radiolytically synthesized palladium nanostructures viz. palladium nanoballs (PdNBs) and palladium urchin (Pdurc) in swollen liquid crystalline mesophase as nanocatalyst in the 4-nitrophenol (4-NP) reduction reaction is investigated by pulse radiolysis technique. The transient optical absorption spectra for the reaction of 4-NP with reducing radical e_{aq}^- , $CO_2^{\bullet-}$, $(CH_3)_2\dot{C}OH$ were studied. The 4-NP shows strong ground state absorption at 400 nm, therefore bleaching is observed for the parent molecule (4-NP) and so background corrections were done and absorption spectra in terms of molar extinction coefficient as a function of wavelength were plotted. The kinetics of the reactions under different experimental conditions viz. pH of solution, concentration of substrates and dose rate were studied to elucidate the mechanism of transient formation and their stability at higher time scale. The second order rate constants were determined by following decay of e_{aq}^- and $CO_2^{\bullet-}$ in both acidic and basic pH conditions. Further the role of Pt nanostructures in the decay of the transient species of 4-NP is investigated under the pseudo first order condition with respect to reducing radical.

1. Introduction

The treatment of waste water from agriculture and industrial effluents before releasing them into water bodies is a major challenge to the scientific community. The effluent contains toxic chemicals like, heavy metals, hydrocarbons and nitro compounds. 4-nitrophenol (4-NP), is one of the major water pollutant released from pharmaceuticals, pesticides, and synthetic dye industries.¹⁻² 4-NP may induce problems associated with nervous and respiratory system in living organisms.³ It is therefore, necessary for proper treatment of industrial waste before being released into natural water bodies. Some of the techniques utilized for the degradation of 4-NP includes microbial degradation and advance oxidation process (AOP).⁴⁻⁵ However, these techniques has its own limitations. eg. the microbial degradation requires long period of incubation, while the AOP involves ozonation, Fenton reaction, UV irradiation, gamma and electron beam irradiation.⁶⁻¹¹ However, these

techniques although used effectively lacks mechanism and characterization of the transient species involved. Pulse radiolysis technique is an excellent tool for the characterization of the transient species and their kinetics study.¹² This technique involves the use of electron beam to generate primary radicals by water radiolysis as described in chapter 1 section 1.3.1. In general, this technique uses low solute concentration ($\leq 10^{-3}$ mol dm⁻³) which creates a pseudo first order kinetic condition with respect to specific radicals produced. The solute concentration is in excess than the reactive radicals. Under these conditions, the reduction of 4-NP by pulse radiolysis has been reported and the transient species are characterized.⁹ 4-NP reduction by NaBH₄ in presence of catalyst gives rise to 4-AP, a known intermediate in pharmaceutical drugs.¹³⁻¹⁴ With the advancement in the area of nanocatalysis, the 4-NP reduction by NaBH₄ has been extensively used as model reaction for evaluating the catalytic activity of nanostructured materials.¹³⁻²⁸ In this

reaction, the reducing agent is in excess, resulting in the pseudo first order kinetic condition with respect to reducing agent which is the reverse of the normal pulse radiolysis conditions. Further, the kinetic model is developed for this reaction in presence of nanocatalyst involving 4 hydrogen transfer reaction.²⁹⁻³¹ However, there has not been any study to mimic these reaction condition using pulse radiolysis and monitor the formation and decay of the transient species in presence of nanostructured material. Therefore, investigation on the mechanism of the transient species formed and their decay with and without metal nanostructures will not only provide first hand information for evaluating the initial steps involved in the catalytic reduction of 4-NP leading to application of nanocatalyst in the remediation of environmental pollutants effectively.

The study investigates the use of pulse radiolysis technique with high dose rate/pulse (90-130 Gy/pulse) producing $5 \times 10^{-5} \text{ mol dm}^{-3}$ to $6.7 \times 10^{-6} \text{ mol dm}^{-3}$ of reducing radicals while maintaining the 4-NP concentration at $1 \times 10^{-6} \text{ mol dm}^{-3}$. These conditions mimics the reaction condition of 4-NP by NaBH_4 and the pseudo first order kinetic condition is maintained with respect to reducing agent. Reducing radicals like 2-hydroxy -2-propyl radical $(\text{CH}_3)_2\dot{\text{C}}\text{OH}$, solvated electrons (e^-_{aq}) and formate radical anion ($\text{CO}_2^{\bullet-}$) were used in presence and absence of PtNBs synthesized by radiolysis as described in chapter 3. The choice of the reducing species like $(\text{CH}_3)_2\dot{\text{C}}\text{OH}$ and $\text{CO}_2^{\bullet-}$ is keeping in view that the yields (G value) are highest for these radicals. These results are compare to pulse radiolysis condition with a dose rate of 10-15 Gy/pulse and 4-NP concentration of $1 \times 10^{-4} \text{ mol dm}^{-3}$ (pseudo first order kinetic condition with respect to 4-NP) in presence and absence of PtNBs to evaluate the mechanism for the reduction of 4-NP under these two conditions.

2. Pulse Radiolysis Study

The pulse radiolysis experiments were carried out at Pune University Linear Accelerator

Facility (PULAF) and BARC, Mumbai. The aqueous solution of 4-NP in presence and absence of PtNBs were subjected to electron beam irradiations from 7 MeV LINAC. The transient optical absorption spectra for the reaction of 4-NP with reducing radical e^-_{aq} , $\text{CO}_2^{\bullet-}$, $(\text{CH}_3)_2\dot{\text{C}}\text{OH}$ were studied. The 4-NP shows strong ground state absorption at 400 nm, therefore bleaching is observed for the parent molecule (4-NP) and so background corrections were done and absorption spectra in terms of molar extinction coefficient as a function of wavelength were plotted. The kinetics of the reactions under different experimental conditions viz. pH of solution, concentration of substrates and dose rate were studied to elucidate the mechanism of transient formation and their stability at higher time scale. The second order rate constants were determined by following decay of e^-_{aq} and $\text{CO}_2^{\bullet-}$ in both acidic and basic pH conditions.

The reactivity and optical properties of the transient species shows strong acid-base dependence, therefore it is essential to determine the pK_a of 4-NP to characterize the acid-base form of 4-NP. The absorbance of $1 \times 10^{-4} \text{ mol dm}^{-3}$ solution of 4-NP were recorded at pH ranging from 1 to 12 as shown in Figure 1. The plot of absorbance at 400 nm, for the 4-nitrophenolate ion of 4-NP versus pH was plotted. From plot, the value of pK_a found to be 7.09. The pK_a corresponds to the dissociation of proton from the phenolic group of the 4-NP and hence at $\text{pH} > pK_a$, 4-NP will be predominantly in the form of 4-nitrophenolate anion. Therefore, the pH of the solutions in this study was chosen so as to ensure predominantly the 4-NP or the 4-nitrophenolate anion.

Reaction of 4-NP with hydrated electron (e^-_{aq})

The time resolved transient absorption spectra of the species produced in the reaction of e^-_{aq} with N_2 saturated 4-NP ($1 \times 10^{-4} \text{ mol dm}^{-3}$) solution containing t-butanol ($2 \times 10^{-1} \text{ mol dm}^{-3}$) were recorded in absence and presence of

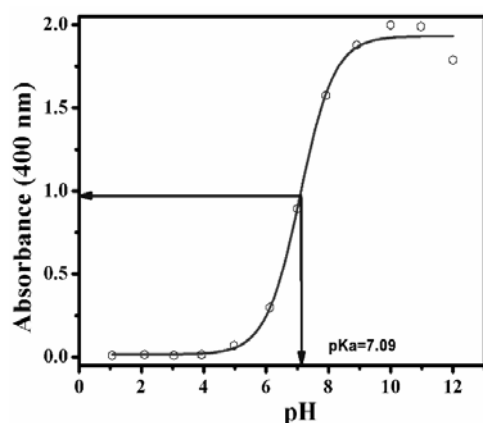
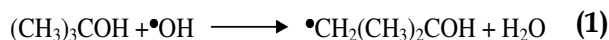


Figure 1. Absorbance at 400 nm as a function of pH for determination of pKa of 4-NP.



PtNBs after the pulse. The role of *t*-butanol is limited to converting strong oxidizing hydroxyl ($\bullet\text{OH}$) radical to weakly reducing carbon centered radical as shown in Equation (1).

The corrected time resolved transient absorption spectra for semi reduced species formed in absence and presence of PtNBs after 10-11 Gy / pulse are shown in the Figure 2 a and b respectively. The spectra recorded in both cases shows strong absorption band around 300 nm which is attributed to the $\text{OHC}_6\text{H}_4\text{NO}_2^\bullet$ radical anion following the reaction of 4-NP with e^-_{aq} . This is in good agreement with the literature report.⁹ The $\text{OHC}_6\text{H}_4\text{NO}_2^\bullet$ radical anion was found to be stable upto 305 μs .

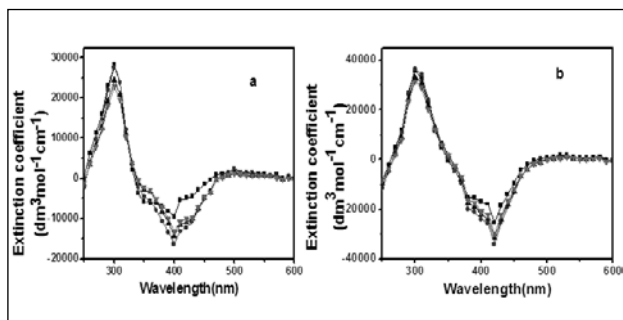


Figure 2. Time resolved corrected transient optical absorption spectra of N_2 saturated solution of 4-NP ($1 \times 10^{-4} \text{ mol dm}^{-3}$) at pH 6.7 containing *t*-butanol (0.2 mol dm^{-3}) for 400 μs . a) without PtNBs; b) with PtNBs (8.3 mg/L) at (■) 6.08 μs , (●) 35.5 μs , (▲) 168 μs , (▼) 305 μs . Dose rate: 10-11 Gy/pulse.

Kinetics of e^-_{aq} reaction at pH 6.7

The decay traces taken at 300 nm and 400 nm monitored for 1000 μs after the pulse at pH

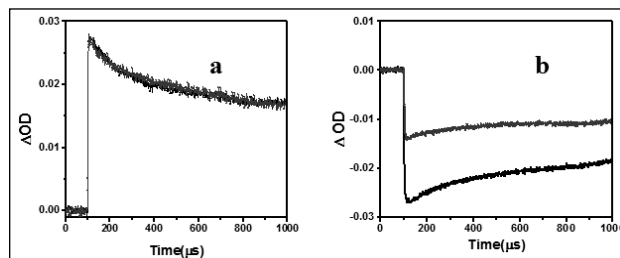


Figure 3. The traces of transient observed for N_2 saturated 4-NP ($1 \times 10^{-4} \text{ mol dm}^{-3}$) solution with *t* butanol (0.2 mol dm^{-3}) in presence (Top) and absence (Bottom) of PtNBs (8.33 ppm) at pH 6.7 a) at 300 nm; b) at 400 nm after the pulse. Dose: 10-11 Gy/pulse.

6.7 are shown in Figure 3 panel a and b. The transient species formed at 300 nm was not affected in presence and absence of PtNBs while the transient formed at 400 nm decays faster in presence of PtNBs as comparing with in absence of PtNBs.

In the pulse radiolysis, pseudo-first order kinetics with respect to the substrate concentration is used to calculate the rate constants of the fast reactions. A relatively high substrate concentration and low radical concentration is kept for such studies. These conditions however, failed to arrive at convincing results in the catalytic reduction of 4-NP, where high concentration of reducing species is essential. In order to study the reduction of 4-NP, the pseudo

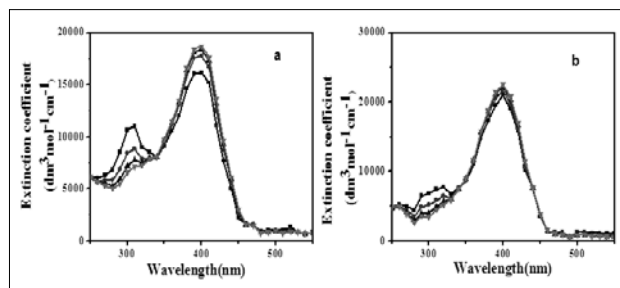


Figure 4. The time resolved corrected transient absorption spectra of N_2 saturated solution of 4-NP ($10 \times 10^{-6} \text{ mol dm}^{-3}$) containing 0.2 mol dm^{-3} *t*-butanol at pH 9.0 for 1000 μs a) without PtNBs b) with PtNBs (8.33 ppm) at (■) 6.4 μs , (●) 106 μs , (▲) 401 μs , (▼) 833 μs . Dose rate: 110-113 Gy/pulse.

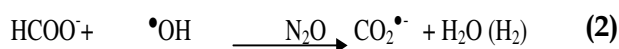
first order condition was maintained with respect to radical concentration (e^-_{aq}) at higher dose rate of 110-113 Gy/pulse. The time resolved transient absorption spectra recorded in absence and presence of PtNBs for N_2 saturated solution of 4-NP ($10 \times 10^{-6} \text{ mol dm}^{-3}$) containing 0.2 mol dm^{-3} t-butanol for 1000 μs at pH 9.0 is shown in Figure 4 a and b respectively. The spectra recorded at 300 nm shows the decrease in absorption with time and corresponding increase in absorption at 400 nm was observed. However, the spectral behaviour is different in presence of PtNBs (Figure 4 b). it was noted that, the formation of $\text{OHC}_6\text{H}_4\text{NO}_2^-$ radical anion at 400 nm was almost complete within 833 μs .

Kinetics of e^-_{aq} reaction at pH 9.0

The traces taken at 300 nm and 400 nm monitored for 1000 μs after the pulse at pH 9.0 are shown in Figure 5. The transient species formed at 300 nm decays with similar rates in presence and absence of PtNBs (Figure 5 a and b).

Reaction of 4-NP with Formate radical ($\text{CO}_2^{\bullet-}$)

To investigate the reaction under pseudo first order condition, yield of reducing radical must be higher than the corresponding substrate.



Therefore, to maintain the high yield of reducing radical, N_2O saturated sodium formate ($5 \times 10^{-1} \text{ mol dm}^{-3}$) was used to produce

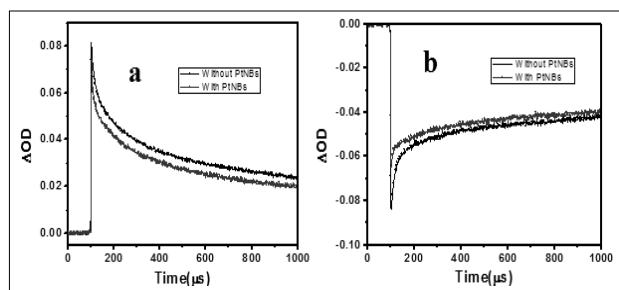


Figure 5. The decay traces of transient recorded at a) at 300 nm, b) at 400 nm) in the reaction of N_2 saturated 4-NP ($10 \times 10^{-6} \text{ mol dm}^{-3}$) with 0.2 mol dm^{-3} t-butanol solution in presence (red) and absence (black) of PtNBs (8.33 ppm) at pH 9.0 for 1000 μs after the pulse. Dose: 110-113 Gy/pulse.

$\text{CO}_2^{\bullet-}$ radicals. In N_2O saturated formate solution, $\bullet\text{OH}$ radicals reacts with formate ion, equation (2) giving $\text{CO}_2^{\bullet-}$ which are reducing in nature with yield 0.58 μM .

The corrected transient absorption spectra of species formed at pH 4.2 in absence and presence of PtNBs after 15-16 Gy/pulse are shown in Figure 6 a and b respectively. The strong transient absorption at 300 nm was observed due to the $\text{OHC}_6\text{H}_4\text{NO}_2^-$ radical formed in the reaction with $\text{CO}_2^{\bullet-}$ radical. The nature of transient absorption spectra recorded in the reactions of formate and

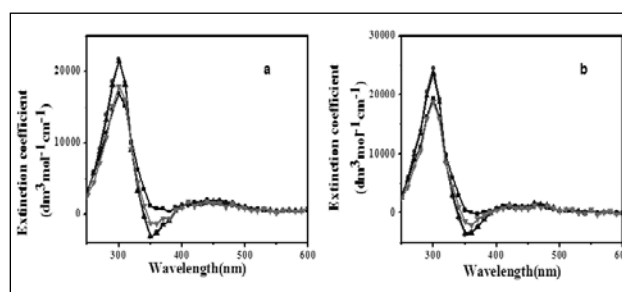


Figure 6. Time resolved corrected absorption spectra of transient formed by the reaction of 4-NP ($1 \times 10^{-4} \text{ mol dm}^{-3}$) with sodium formate ($5 \times 10^{-1} \text{ mol dm}^{-3}$) for 1000 μs a) without PtNBs; b) with PtNBs (8.3mg/L) at pH 4.2 at (■) 12 μs , (●) 85.6 μs , (▲) 216 μs , (▼) 804 μs after the pulse. Dose=15-16 Gy/pulse.

e^-_{aq} were observed to be similar below the pKa in presence and absence of PtNBs. This indicates that the transient formed with $\text{CO}_2^{\bullet-}$ radicals at 300 nm was quite stable and not reducing in nature at low dose and high substrate concentration.

However, the corrected transient absorption spectra taken at pH 9.1 shows two distinct absorptions at 300 and 400 nm with a dose of 15-16 Gy/pulse. At 300 nm, the extinction coefficient for the transient species $\text{OHC}_6\text{H}_4\text{NO}_2^-$ decreases from $37500 \text{ dm}^3 \text{ mol}^{-1} \text{ cm}^{-1}$ to $23400 \text{ dm}^3 \text{ mol}^{-1} \text{ cm}^{-1}$ in absence of PtNBs; however, this decrease was accompanied by simultaneous increase in extinction coefficient from $10000 \text{ dm}^3 \text{ mol}^{-1} \text{ cm}^{-1}$ to $18000 \text{ dm}^3 \text{ mol}^{-1} \text{ cm}^{-1}$ at 400 nm (Figure 7 a and b). It has to be noted that, with higher substrate concentration at low dose and lower radical concentration, $\text{OHC}_6\text{H}_4\text{NO}_2^-$ species is quite stable and not reducing.

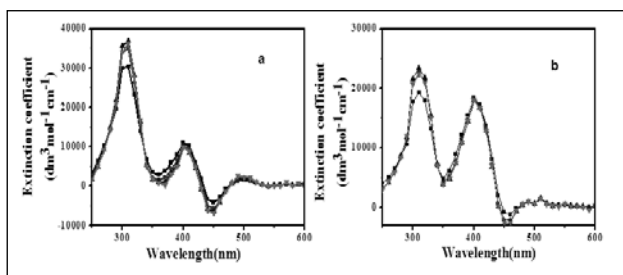


Figure 7. Time resolved corrected absorption spectra of transient formed by the reaction of 4-NP ($1 \times 10^{-4} \text{ mol dm}^{-3}$) with sodium formate ($5 \times 10^{-1} \text{ mol dm}^{-3}$) at pH 9.1 for 1000 μs a) without PtNBs b) with PtNBs; at (■) 12 μs , (●) 85.6 μs , (▲) 216 μs , (▼) 804 μs after the pulse. Dose=15-16 Gy/pulse.

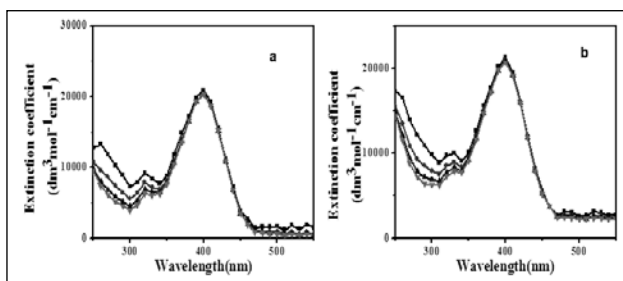


Figure 8. Time resolved corrected absorption spectra of transient formed by the reaction of 4-NP ($5 \times 10^{-6} \text{ mol dm}^{-3}$) with sodium formate ($5 \times 10^{-1} \text{ mol dm}^{-3}$) at pH 10.0 for 400 μs a) without PtNBs b) with PtNBs (8.33 ppm) at (■) 2.24 μs , (●) 16 μs , (▲) 61.4 μs , (▼) 315 μs after the pulse. Dose rate: 110-115 Gy/pulse.

Therefore, the study was carried out at higher dose rate of 110-115 Gy/pulse by maintaining pseudo first order condition with respect to $\text{CO}_2^{\bullet-}$ radical. The corrected transient absorption spectra shows a maximum at 400 nm accompanied by a small shoulder around 300 nm (Figure 8 a and b).

Kinetics of the reaction

The traces of 4-NP ($5 \times 10^{-6} \text{ mol dm}^{-3}$) with $\text{CO}_2^{\bullet-}$ radical in presence and absence of PtNBs at pH 10.00 after the dose of 90-100 Gy/pulse are depicted in Figure 9 a and b respectively. The transient optical absorption at 300 nm and 320 nm were different and at 320 nm stable transient was formed as compare to 300 nm. This was confirmed by calculating the second order rate constants at pH 10. The second order rate constant for the decay of species formed at 300

nm in absence and presence of PtNBs at pH 10 was found to be $2.8 \times 10^9 \text{ dm}^3 \text{ mol}^{-1} \text{ s}^{-1}$ and $4.3 \times 10^9 \text{ dm}^3 \text{ mol}^{-1} \text{ s}^{-1}$ respectively. This indicated that the second order rate constant is 1.5 times

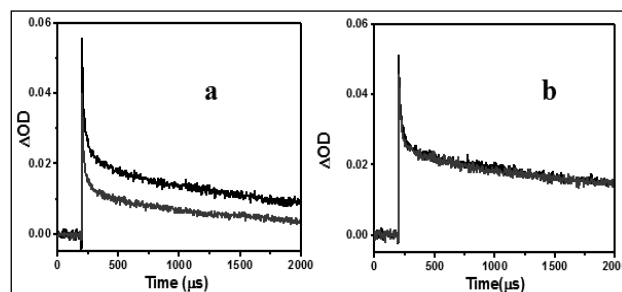


Figure 9. The traces of 4-NP ($5 \times 10^{-6} \text{ mol dm}^{-3}$) with sodium formate ($5 \times 10^{-1} \text{ mol dm}^{-3}$) at pH 10 for a) 300 nm b) at 320 nm; a: without PtNBs, b: with PtNBs (8.33 ppm). Dose/Pulse= 90-100 Gy.

more in presence of PtNBs While no significant change was observed in case of 320 nm ($\sim 3.3 \times 10^9 \text{ dm}^3 \text{ mol}^{-1} \text{ s}^{-1}$).

The kinetics of the reaction of 4-NP with $\text{CO}_2^{\bullet-}$ radicals were studied and the second order rate constants were evaluated at 300 nm from the linear dependence of first order decay rate in the range of concentrations of ($1 \times 10^{-6} \text{ mol dm}^{-3}$ to $5 \times 10^{-6} \text{ mol dm}^{-3}$ (Figure 10). The observed second order rate constants for $1 \times 10^{-6} \text{ mol dm}^{-3}$ to $5 \times 10^{-6} \text{ mol dm}^{-3}$ 4-NP solution was found to be $6.99 \times 10^{10} \text{ dm}^3 \text{ mol}^{-1} \text{ s}^{-1}$ to $1.35 \times 10^{10} \text{ dm}^3 \text{ mol}^{-1} \text{ s}^{-1}$ in

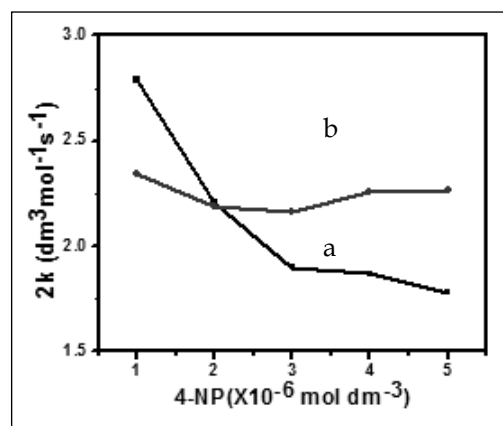


Figure 10. The second order rate constant as a function of 4-NP concentration at 300 nm in the reaction of 4-NP ($1-5 \times 10^{-6} \text{ mol dm}^{-3}$) with sodium formate ($5 \times 10^{-1} \text{ mol dm}^{-3}$) at pH 10. A: without PtNBs; B: with PtNBs (8.33 ppm). Dose/Pulse= 111 Gy.

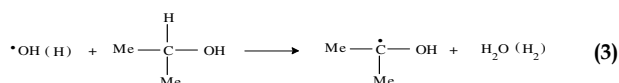
Table 1. Second order rate constants ($2k/10^6 \text{ dm}^3 \text{ mol}^{-1} \text{ s}^{-1}$) for the reaction of 4-NP ($1 \times 10^{-6} \text{ mol dm}^{-3}$) to ($5 \times 10^{-6} \text{ mol dm}^{-3}$) with $\text{CO}_2^{\bullet-}$ radical at pH 10.

[4-NP] ($\times 10^{-6} \text{ mol dm}^{-3}$)	$2k(\text{decay})/10^6 \text{ dm}^3 \text{ mol}^{-1} \text{ s}^{-1}$	
	Absence of PtNBs	Presence of PtNBs
1	2.79	2.34
2	2.21	2.19
3	1.90	2.09
4	1.87	2.30
5	1.78	2.27

absence of PtNBs while in presence of PtNBs they were, $7.33 \times 10^{10} \text{ dm}^3 \text{ mol}^{-1} \text{ s}^{-1}$ to $1.69 \times 10^{10} \text{ dm}^3 \text{ mol}^{-1} \text{ s}^{-1}$. (Table 1).

Reaction of 4-NP with 2-hydroxy propyl radical ($(\text{CH}_3)_2\dot{\text{C}}\text{OH}$)

The pulse radiolysis experiments were carried out in N_2O saturated solution of $10 \times 10^{-6} \text{ mol dm}^{-3}$ 4-NP containing $1 \times 10^{-1} \text{ mol dm}^{-3}$ 2-propanol at pH 9. Here, H^\bullet and $\bullet\text{OH}$ radicals are scavenge by 2-propanol forming $(\text{CH}_3)_2\dot{\text{C}}\text{OH}$ radical as shown equation (3).



The time resolved transient optical absorption spectra obtained from pulse radiolysis of N_2O saturated solution of $1 \times 10^{-5} \text{ mol dm}^{-3}$ 4-NP containing 0.1 mol dm^{-3} 2-propanol at pH 9.0 in absence and presence of PtNBs recorded at $1000 \mu\text{s}$ were shown in Figure 11, panel a and b.

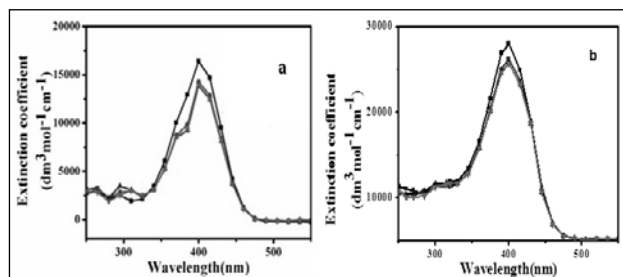


Figure 11. Time resolved corrected absorption spectra of transient formed by the reaction of 4-NP ($10 \times 10^{-6} \text{ mol dm}^{-3}$) with 2-propanol ($1 \times 10^{-1} \text{ mol dm}^{-3}$) at pH 9.0 for $1000 \mu\text{s}$. a) without PtNBs; b) with PtNBs (8.3 mg/L) at (■) $10 \mu\text{s}$, (●) $90 \mu\text{s}$, (▲) $200 \mu\text{s}$, (▼) $900 \mu\text{s}$ after the pulse. Dose = 135-140 Gy/pulse.

The comparison of transient optical absorption at 320 nm and 400 nm in the reaction of 2-propanol ($1 \times 10^{-1} \text{ mol dm}^{-3}$) with different 4-NP concentrations up to $5 \mu\text{s}$ after the pulse are depicted in Figure 12. From Figure 12 panel a and b reveals that the reduction of 4-NP is a two step process where initial formation of transient takes place up to $2 \mu\text{s}$ and then it decays slowly.

4. Conclusion

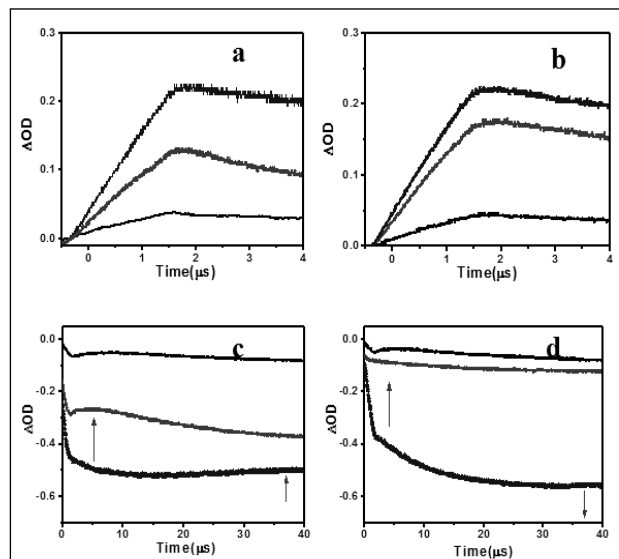


Figure 12. The comparison of transient optical absorption in the reaction of 2-propanol ($1 \times 10^{-1} \text{ mol dm}^{-3}$) with 4-NP. (A: $10 \times 10^{-6} \text{ mol dm}^{-3}$, B: $50 \times 10^{-6} \text{ mol dm}^{-3}$, C: $100 \times 10^{-6} \text{ mol dm}^{-3}$) at pH 9 for $5 \mu\text{s}$. a) at 320 nm in presence PtNBs (8.33 ppm); b) in absence PtNBs. At 400 nm for $50 \mu\text{s}$, c) in presence of PtNBs (8.33 ppm); d) in absence of PtNBs. Dose/Pulse = 135-140 Gy/pulse.

The reduction of 4-NP in presence and absence of PtNBs with solvated electrons ($e_{\text{aq}}^{\bullet-}$), formate ($\text{CO}_2^{\bullet-}$) radical anion and 2-hydroxy propyl $(\text{CH}_3)_2\dot{\text{C}}\text{OH}$ radical leads to formation of nitrophenolate anion radical at 400 nm. These radicals decay fast in presence of PtNBs results in formation of semireduced species. The second order rate constants for $\text{CO}_2^{\bullet-}$ radical with (1-5) $\times 10^{-6} \text{ mol dm}^{-3}$ 4-NP solution was found to be $(6.99-1.35) \times 10^{10} \text{ dm}^3 \text{ mol}^{-1} \text{ s}^{-1}$ in absence of PtNBs while in presence of PtNBs they were, $(7.33-1.69) \times 10^{10} \text{ dm}^3 \text{ mol}^{-1} \text{ s}^{-1}$. The differences in the transient absorption spectra with and without PtNBs suggests that these radicals react very fast but the stable product formed was long lived.

5. References

1. W. Zhang, F. Tan, W. Wang, X. Qiu, X. Qiao, J. Chen, J. Hazard. Mater., 217, 36, (2012).
2. N. Comisso, S. Cattarin, S. Fiameni, R. Gerbasi, L. Mattarozzi, M. Musiani, L. Vázquez- Gómez, E. Verlato, Electrochem. Commun., 25, 91, (2012).
3. W. B. Zhang, J. Chem. Technol. Biotechnol., 78, 788, (2003).
4. E. Suja, Y. V. Nancharaiiah, V. P. Venugopalan, Appl. Biochem. Biotechnol., 167, 1569, (2012).
5. P. Saritha, C. Aparna, V. Himabindu, Y. Anjaneyulu, J. Hazard. Mater., 149, 609, (2007).
6. J. A. Herrera-Melián, A. J. Martín-Rodríguez, A. Ortega-Méndez, J. Araña, J. M. Doña- Rodríguez, J. Pérez-Peña, J. Environ. Manage., 105, 53, (2012).
7. Q. Dai, L. Lei, X. Zhang, Sep. Purif. Technol., 61, 123, (2008).
8. F. S. García Einschlag, J. I. Felice, J. M. Triszcz, Photochem. Photobiol. Sci., 8, 953, (2009).
9. J. Biswal, J. Paul, D. B. Naik, S. K. Sarkar, S. Sabharwal, Radiat. Phys. Chem., 85, 161, (2013).
10. S. Weihua, Z. Zheng, A. S. Rami, Z. Tao, H. Desheng, Radiat. Phys. Chem., 65, 559, (2002).
11. F. Follut, N. Karpel Vel Leitner, Chemosphere, 66, 2114, (2007).
12. J. F. Wishart, B. S. M. Rao, Recent trends in radiation chemistry, world scientific, (2010).
13. K. Esumi, K. Miyamoto, T. Yoshimura, J. Colloid Interface Sci., 254, 402, (2002).
14. N. Pradhan, A. Pal, T. Pal, Colloids Surf. A: Physicochem. Eng. Aspects, 196, 247, (2002).
15. Y. Mei, G. Sharma, Y. Lu, M. Ballauff, Langmuir, 21, 12229, (2005).
16. S. Panigrahi, S. Basu, S. Praharaj, S. Pande, S. Jana, A. Pal, S. K. Gosh, T. Pal, J. Phys. Chem. C, 111, 4596, (2007).
17. S. Jana, T. Pal, J. Nanosci. Nanotechnol., 7, 2151, (2007).
18. Y. Mei, Y. Lu, F. Polzer, M. Ballauff, Chem. Mater., 19, 1062, (2007).
19. W. Yang, Y. Ma, J. Tang, X. Yang, Colloids and Surfaces A: Physicochem. Eng. Aspects, 302, 628, (2007).
20. S. Oh, M. Kim, S. Choi, J. Chun, K. Lee, A. Gopalan, C. Hwang, K. Ho, O. Hoon, J. Ind. Eng. Chem., 14, 687, (2008).
21. S. Saha, A. Pal, S. Kundu, S. Basu, T. Pal, Langmuir, 26, 2885, (2010).
22. G. W. Qin, W. Pei, X. Ma, X. Xu, Y. Ren, W. Sun, L. Zuo, J. Phys. Chem. C, 114, 6909, (2010).
23. Y. Shaoqing, H. Jun, W. Jianlong, Radiat. Phys. Chem., 79, 1039, (2010).
24. J. T. Zhang, G. Wei, T. F. Keller, H. Gallagher, C. Toetzel, F. A. Mueller, M. Gottschaldt, U. S. Schubert, K. D. Jandt, Macromol. Mater. Eng., 295, 1049, (2010).
25. M. A. Mahmoud, M. A. El-Sayed, Nano Lett., 11, 946, (2011).
26. S. Sarkar, A. K. Sinha, M. Pradhan, M. Basu, Y. Negishi, T. Pal, J. Phys. Chem. C, 115, 1659, (2011).
27. S. Wu, J. Kaiser, X. Guo, L. Li, Y. Lu, M. Ballauff, Ind. Eng. Chem. Res., 51, 5608, (2012).
28. J. A. Johnson, J. J. Makis, K. A. Marvin, S. E. Rodenbusch, K. J. Stevenson, J. Phys. Chem. C, 117, 22644, (2013).
29. N. Bingwa, R. Meijboom, J. Phys. Chem. C, 118, 19849, (2014).
30. N. Bingwa, R. Meijboom, Journal of Molecular Catalysis A: Chemical, 396, 1, (2015).
31. S. Gu, S. Wunder, Y. Lu, M. Ballauff, R. Fenger, K. Rademann, B. Jaquet, A. Zacccone, J. Phys. Chem. C, 118, 18618, (2014).

Reactions of model peroxy ($\text{CCl}_3\text{O}_2^\bullet$) radical by radiation chemical method

Shaukat Ali M. Shaikh,¹ Rupali G. Shinde,^{1,2} Atanu Barik^{1*}

¹Radiation & Photochemistry Division, Bhabha Atomic Research Centre, Trombay, Mumbai-400085, India

²Department of Chemistry, Savitribai Phule Pune University, Pune 411007, India.

email: atanu@barc.gov.in

Abstract

Peroxy radicals have fatal consequences in physiological system due to relative long life time (few seconds) which allows it to diffuse long distance from the site of generation. Due to different mode of reactions, it initiates and propagates the chain reaction in lipid peroxidation process. To combat this situation it is necessary to understand the kinetics of peroxy radical reaction with different compounds. As the reaction kinetics of peroxy radical takes place in microsecond time scale radiation chemical techniques, particularly pulse radiolysis technique finds extremely useful to study such reactions. In the aqueous environment trichloro methyl peroxy ($\text{CCl}_3\text{O}_2^\bullet$) radical is the unique model peroxy radical which is quantitatively produced by radiation chemical method. The chemical properties of $\text{CCl}_3\text{O}_2^\bullet$ radical including its generation, reaction and mode of reaction have been discussed. The reaction mechanism and the kinetics of the $\text{CCl}_3\text{O}_2^\bullet$ radical reaction with phenolic compounds, curcumin derivatives and organoselenium compounds have been studied. Wherever possible, structure activity correlation was established for a particular group of compounds.

Introduction

Ever since it was established that presence of oxygen intensify the radiation damage to the biological systems, peroxy radicals are considered to be the prime suspect for that process.¹ The formation of free radicals by thermal, photochemical or radiation chemical methods led to the formation of corresponding peroxy radicals very rapidly in the presence of oxygen.²⁻⁵ The very simple form of peroxy radical is perhydroxyl radical (HOO^\bullet) which is a conjugate acid of superoxide radical. Due to low pK_a (4.88) compare to biological pH, the reactivity of HOO^\bullet radical is important in the case of bilayer lipid membrane environment.⁵ Though the peroxy radical belongs to the class of reactive oxygen species (ROS), but they have certain distinct characteristics compared to other ROS. Peroxy radicals are primarily strong oxidants with an estimated lifetime of few seconds. The reactivity of the radicals depends on their half life. For example half life of hydroxyl ($^\bullet\text{OH}$) radical is

few nano seconds, whereas for peroxy (ROO^\bullet) radical it is in micro seconds.⁶ Obviously, in the physiological environment, other factors such as pH and the presence of other species, has a immense influence on the half-life of ROS. It may not be necessary that toxicity is directly correlated with the reactivity of the radical.⁷ In many cases a longer half life of a species might imply a higher toxicity of the compound by allowing it adequate time to diffuse and reach the sensitive location, where it can interact and cause damage at a long distance from its site of production. Peroxy radicals are the key source for lipid peroxidation. It is a chain reaction process initiated by hydrogen atom abstraction and by addition of oxygen radical, resulting in the oxidative damage of polyunsaturated fatty acids (PUFA).⁸ The active methylene group in PUFA is the primary site for hydrogen atom abstraction, whereas oxygen addition occurred to the carbon centered radical resulting lipid peroxy radical. These lipid peroxy radicals subsequently take part in the radical propagation reaction. The peroxidative

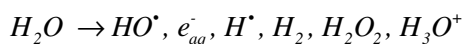
decomposition of unsaturated fatty acid resulted in different types of aldehydes. Compared to free radicals, aldehydes are highly stable and diffuse out from the cell and attack targets far from the site of their production. Ultimately the process of lipid peroxidation happens to be in all aerobic cells which led to oxidative damage to cell structures and the toxic aldehydes multiply the process of cell death.⁸⁻⁹ Here comes the role of antioxidant supplementation to protect the cells from the oxidative stress. There are large numbers of compounds that can act as peroxy radical scavenger. Some of the representative compounds have been discussed with respect to their reactivity with model peroxy radical like trichloro methyl peroxy ($\text{CCl}_3\text{O}_2^\bullet$) radical generated by radiation chemical method. It should be noted that incorporation of halogen atom in peroxy radical increases its oxidising power.

Experimental

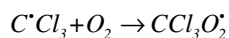
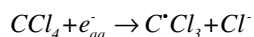
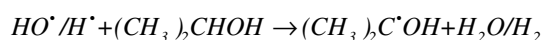
Generation of $\text{CCl}_3\text{O}_2^\bullet$ radical by radiation chemical method

Irradiation of aqueous solution with high energy electron or gamma radiation led to formation of e_{aq}^- , H^\bullet and OH^\bullet radicals in addition to the molecular products H_2 , H_2O_2 and H_3O^+ .¹⁰⁻¹²

$\text{CCl}_3\text{O}_2^\bullet$ radical was generated by irradiation

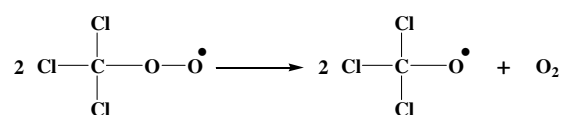


of the aerated aqueous solution containing 48% isopropanol (v/v) and 4% carbon tetrachloride (v/v) as shown in the following reaction sequence.^{2,13}



Considering the above reaction scheme the reported radiation chemical yield (G) of $\text{CCl}_3\text{O}_2^\bullet$ radical was $0.64 \mu\text{mol/J}$.¹⁴ The reaction of molecular oxygen with CCl_3^\bullet radical is under

diffusion control with rate constant of $3.3 \times 10^9 \text{ M}^{-1}\text{s}^{-1}$.¹⁵ Due to electrophilic nature of the oxygen, reaction of oxygen depends on the electron density at the radical site. Although in the case of CCl_3^\bullet radical, electron withdrawing nature of the chlorine atoms decreases the electron density at the radical site, the high reactivity is observed due to pyramidal structure of CCl_3^\bullet radical which allows easy access of oxygen atom to the radical site.¹⁶ The fate of the $\text{CCl}_3\text{O}_2^\bullet$ radical is radical-radical termination, which led to formation of trichloro methoxy ($\text{CCl}_3\text{O}^\bullet$) radical as shown in reaction.¹⁶

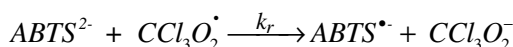


The pulse radiolysis experiments were carried out with high energy electron pulses (7 MeV) obtained from linear electron accelerator.^{17,18} The transients were detected by absorption spectrometry. The absorbed dose was measured by using aerated thiocyanate dosimeter by monitoring the $(\text{SCN})_2^{\bullet-}$ species at 475 nm with G ϵ value of $2.59 \times 10^{-4} \text{ m}^2\text{J}^{-1}$.¹⁹ Here G denotes the radiation chemical yield in mol/J and ϵ , the molar absorption coefficient in m^2/mol . Typical dose/pulse used for these studies were varied from 12 to 25 Gy.

Results and discussion

The reaction of $\text{CCl}_3\text{O}_2^\bullet$ radicals with molecules can be studied conveniently by radiation chemical method. In general for radiation chemical studies with OH^\bullet radical reaction the compound should be water soluble, but such type of limitation is not observed with $\text{CCl}_3\text{O}_2^\bullet$ radical. The predominant reaction of $\text{CCl}_3\text{O}_2^\bullet$ radical is oxidation reaction. The standard reduction potential of $\text{CCl}_3\text{O}_2^\bullet / \text{CCl}_3\text{O}_2^-$ is 1.55 V with respect to NHE.²⁰ The transient obtained by the reaction of $\text{CCl}_3\text{O}_2^\bullet$ radical with any compound can be observed by absorption spectrophotometry, provided the transient have absorption in the UV-visible region. From the kinetic absorption traces of the transient one

can estimate the observed rate constant under different concentrations of the compound maintaining pseudo first order condition. If the transient do not have any absorption in the above working wavelength, competition kinetics is an alternative way to estimate the bimolecular rate constant between $\text{CCl}_3\text{O}_2^\bullet$ radical with the compounds of interest.²¹⁻²³ In such cases a reference redox indicator has been used with the conditions a) the reference compound should be oxidised by $\text{CCl}_3\text{O}_2^\bullet$ radical, b) the oxidised product of the transient should have absorption in the working wavelength, c) the bimolecular rate constant (k_r) between $\text{CCl}_3\text{O}_2^\bullet$ radical and reference compound should be known. 2,2'-azinobis(3-ethylbenzthiazoline-6-sulfonic acid) diammonium salt (ABTS²⁻) is commonly used as a reference compound.



$$\frac{\text{Abs}_0}{\text{Abs}} = 1 + \frac{k_b}{k_r} \left(\frac{[\text{Compound}]}{[\text{ABTS}^{2-}]} \right)$$

Where k_b represents the rate constant between $\text{CCl}_3\text{O}_2^\bullet$ radical and "Compound" of interest. "Abs₀" and "Abs" denotes the absorbance of the ABTS²⁻ radical at 645 nm in absence and presence of compound. The rate constant (k_r) for the reaction of $\text{CCl}_3\text{O}_2^\bullet$ radical with ABTS²⁻ is $1.9 \times 10^9 \text{ M}^{-1}\text{s}^{-1}$.²¹

Kinetics of peroxy radical with selected compounds

Phenolic compounds

Bergenin, a polyphenol, exhibits antihepatotoxic, neuroprotective, anti-inflammatory and immunomodulatory properties. In most of these biological activities, bergenin either acts as a free radical scavenger or a redox regulatory agent. The transient absorption spectra for the reaction of bergenin with $\text{CCl}_3\text{O}_2^\bullet$ radicals at pH 7 has been shown in Figure 1. The transient product has absorption maxima at 400 nm.¹⁸ By monitoring

the k_{obs} (inset of figure 1) for the formation of the transient at 400 nm, as a function of bergenin concentration from 5 to 20 μM , the bimolecular rate constant for the reaction of $\text{CCl}_3\text{O}_2^\bullet$ radical with bergenin was evaluated as $4.2 \times 10^6 \text{ M}^{-1}\text{s}^{-1}$.¹⁸

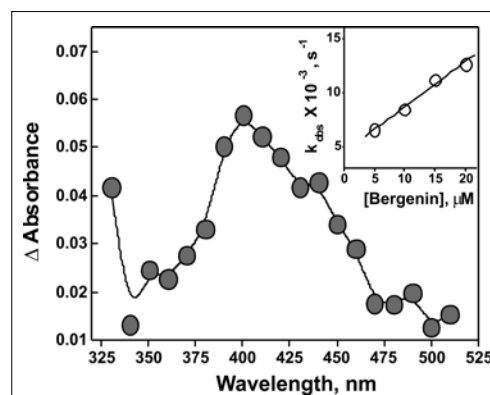
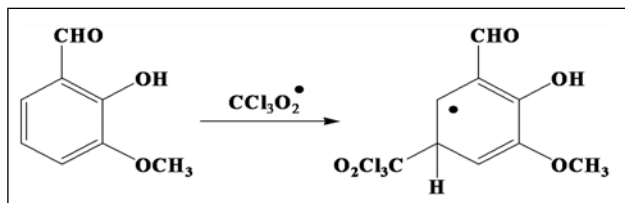


Figure 1: Transient absorption spectrum obtained on reaction of $\text{CCl}_3\text{O}_2^\bullet$ radical with 100 μM bergenin (Dose 14 Gy). Inset shows that observed rate of formation (k_{obs}) increases with increase in concentration of bergenin at 400 nm.

Ortho vanillin (o-vanillin) is a structural isomer of vanillin, a natural plant phenols frequently used in food, mainly as flavouring agents.²⁴⁻²⁵ There is contrasting report of biological activity between these two molecules. While vanillin acts as an antioxidant, o-vanillin enhances the mutagenic effects caused by different agents.²⁵⁻²⁶ Due to the presence of phenolic OH, o-vanillin has pK_a of 7.91. Thus below pH 7.91, it is in the phenol form above pH 7.91 it exists in phenolate form.²⁶ The reaction of $\text{CCl}_3\text{O}_2^\bullet$ radical with o-vanillin at neutral pH was very slow with a bimolecular rate constant of $10^5 \text{ M}^{-1}\text{s}^{-1}$, however the rate constant for the same reaction at alkaline pH (pH 9.7) was estimated to be $2 \times 10^6 \text{ M}^{-1}\text{s}^{-1}$.¹³ In general, the reactions of many substituted phenols with halocarbon peroxy radicals are faster by orders of magnitude; however, o-vanillin showed a much slower rate constant with $\text{CCl}_3\text{O}_2^\bullet$ radicals. The transient spectra obtained from reaction of azide radical and $\text{CCl}_3\text{O}_2^\bullet$ radicals at neutral pH were very much different from each other suggesting that $\text{CCl}_3\text{O}_2^\bullet$ radicals were unable to oxidise o-vanillin.

In the case of o-vanillin the reaction appeared that it was not driven by electron transfer but by addition to the ring, probably at the para position to the phenolic OH as shown below.

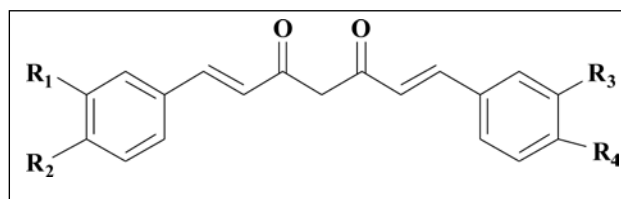


The phenolic OH group in o-vanillin is sterically crowded by the two bulky groups on both sides like methoxy group and aldehyde group. The $\text{CCl}_3\text{O}_2^\bullet$ group, also being very bulky, was unable to approach towards the phenolic OH group. Thermodynamically, electron transfer should have taken place as the one-electron oxidation potential values are favourable.¹³ However, the reaction appeared not only to be controlled thermodynamically but also kinetically. There were also reports in the literature that reduction potential of reacting molecules is not only the sole factor for the reactivity of $\text{CCl}_3\text{O}_2^\bullet$ radical. The rate constant for the reaction of $\text{CCl}_3\text{O}_2^\bullet$ radical with ebselen and 1,5-diselenocyclooctane was 3×10^8 and $2 \times 10^8 \text{ M}^{-1}\text{s}^{-1}$ respectively.¹⁶ Though the values of rate constants were nearly same, but the reduction potential of ebselen and 1,5-diselenocyclooctane was very much different. The reduction potential for ebselen and 1,5-diselenocyclooctane was 1.59 V and 0.25 V Vs Ag/AgCl electrode respectively in acetonitrile.¹⁶ These observations indirectly suggest that some different or additional reaction mechanism is prevalent for $\text{CCl}_3\text{O}_2^\bullet$ radical rather than simple one-electron oxidation process.

Curcumin and its derivatives

Curcumin is a polyphenol found in turmeric rhizome. Though curcumin exhibit excellent pharmacological properties, but its application is limited due to meagre aqueous solubility and bioavailability. Also it undergoes rapid degradation in aqueous medium. To overcome these problems several curcumin derivatives were

synthesised by different research groups.²¹ The strategy that are adopted is to have derivatives of curcumin either through the modification of phenolic OH group or through the β -diketo group. Here the reaction of $\text{CCl}_3\text{O}_2^\bullet$ radical with curcumin and its derivatives (Scheme 1) bis demethoxy curcumin (BDMC), mono demethoxy curcumin (MDMC) and dimethoxy curcumin (DMC) were studied by pulse radiolysis technique.



Curcumin :- $\text{R}_1 = \text{R}_3 = \text{OCH}_3$, $\text{R}_2 = \text{R}_4 = \text{OH}$
 MDMC :- $\text{R}_1 = \text{H}$, $\text{R}_2 = \text{R}_4 = \text{OH}$, $\text{R}_3 = \text{OCH}_3$
 BDMC :- $\text{R}_1 = \text{R}_3 = \text{H}$, $\text{R}_2 = \text{R}_4 = \text{OH}$
 DMC :- $\text{R}_1 = \text{R}_2 = \text{R}_3 = \text{R}_4 = \text{OCH}_3$

Scheme 1: Structures of curcumin and its derivatives

The transient absorption spectrum of curcumin and its analogue were broad in nature having absorption maxima at 490 to 500 nm. Typical transient absorption spectrum of MDMC with $\text{CCl}_3\text{O}_2^\bullet$ radical is shown in figure 2. Inset of figure 2 shows that the observed formation rate of the transient at 490 nm for MDMC with $\text{CCl}_3\text{O}_2^\bullet$ radical was increasing with increasing concentration of MDMC and from the slope of the linear fit the bimolecular rate constant was evaluated as $5.5 \times 10^7 \text{ M}^{-1}\text{s}^{-1}$.²¹

Peroxy radical reaction proceeds either the addition reaction forming radical adducts or through one electron oxidation. Formation of radical adducts most of the time lead to chain reaction, which is not desire for a free radical scavenger. The reaction of curcumin with pulse radiolytically generated specific one electron oxidant, produced phenoxyl type radical,²⁷ which have very similar transient spectrum to that of produced by reaction of curcumin with $\text{CCl}_3\text{O}_2^\bullet$ radical. The transient spectrum

for other curcumin analogues, viz. BDMC, and DMC, could not be recorded because of high value of parent absorption. Alternatively the bimolecular rate constant between curcumin and its analogues with $\text{CCl}_3\text{O}_2^\bullet$ radical were estimated by employing competition kinetic method.

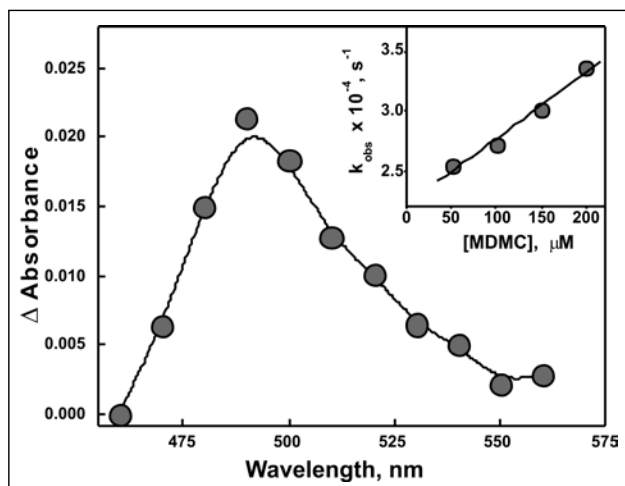


Figure 2: Transient absorption spectrum obtained on reaction of $\text{CCl}_3\text{O}_2^\bullet$ radical with $100 \mu\text{M}$ MDMC at pH 7 (Dose 20 Gy). Inset shows that observed rate of formation (k_{obs}) increases with increase in concentration of MDMC at 490 nm.

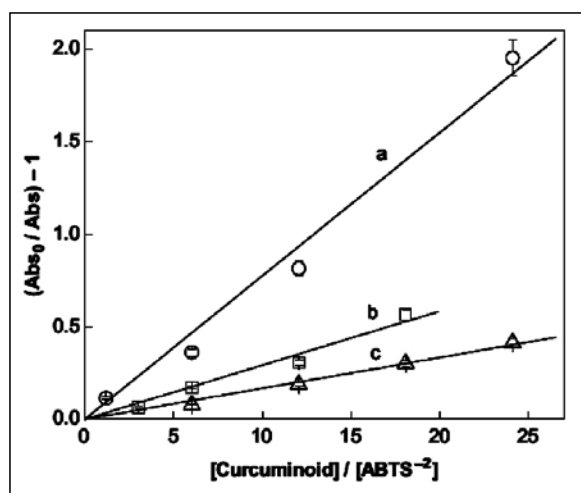


Figure 3: Change of absorbance of $\text{ABTS}^{\bullet-}$ at 645 nm in presence of different concentration of (a) Curcumin, (b) MDMC and (c) BDMC.

The bimolecular rate constants for $\text{CCl}_3\text{O}_2^\bullet$ radical with curcumin and its analogues were estimated as 14.7×10^7 , 5.9×10^7 , $3.1 \times 10^7 \text{ M}^{-1}\text{s}^{-1}$ for curcumin, MDMC, BDMC respectively as listed in table 1.²¹

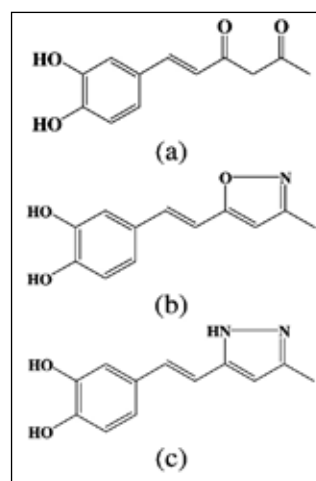
Table 1: Bimolecular rate constant of curcumin analogues with $\text{CCl}_3\text{O}_2^\bullet$ radical

Compounds	Rate constant, $\text{M}^{-1}\text{s}^{-1}$
Curcumin	14.7×10^7
MDMC	5.9×10^7
BDMC	3.1×10^7
DMC	Not detected

Curcumin analogue having phenolic OH group, reacted with $\text{CCl}_3\text{O}_2^\bullet$ radical to form corresponding phenoxyl radical. On the contrary DMC, which do not possesses any phenolic -OH group, was unreactive towards the peroxy radical. The variation of bimolecular rate constant between the curcumin analogues and $\text{CCl}_3\text{O}_2^\bullet$ radical was due to the electron donating nature of the substituent. Due to strong electron donating nature of methoxy group the rate constant is directly proportional to number of methoxy group present in the curcumin analogue.

Hispolon and its analogue

Hispolon (HS) is another natural product which structurally resembles with half curcumin. It has been found to be present in several medicinal species including plants, herbs and fungi.²⁸ HS isolated from *Phellinus linteus*, a traditional Chinese medicinal mushroom used for gastric diseases has been found to induce apoptosis in human epidermoid cells.²⁹ Recently HS and its derivatives were synthesised and



Scheme 2: Structures of (a) hispolon (HS) and its (b) isoxazole (HI), (c) pyrazole derivatives

evaluated for anti-cancer activity.³⁰ To understand the structure activity relationship, the β -diketo of HS was converted to its isoxazole (HI) and pyrazole (HP) derivatives as shown in scheme 2. The reaction of $\text{CCl}_3\text{O}_2^\bullet$ with HI and HP produced the transient species that showed absorption maxima (~ 410 to 420 nm) very similar in comparison to azide radical reaction except in HS where it has absorption maximum at 480 nm (Figure 4).²³ Due to the β -diketo group in HS, the hydrogen atom present in the methylene group is labile. It has been already discussed about the multimodal reaction pathways of $\text{CCl}_3\text{O}_2^\bullet$ radical. There was possibility of hydrogen atom abstraction from methylene group which resulted shift in the transient absorption band towards the longer wavelength.¹⁴

The rate constant, k_b for reaction of $\text{CCl}_3\text{O}_2^\bullet$ radicals with HS, HI and HP was estimated as 1.6×10^8 , 1.7×10^8 , and 2.5×10^8 $\text{M}^{-1}\text{s}^{-1}$ respectively.²³ The results indicated that the compounds show similar reactivity with $\text{CCl}_3\text{O}_2^\bullet$ radicals, while HP showed marginally higher bimolecular rate constant than HI and HS.

Organoselenium compounds

Selenium is an essential micronutrient for human, which is obtained primarily in the form of selenomethionine by consuming plant products. The selenomethionine obtained from these sources acts as a precursor for the synthesis of selenocysteine. Selenocysteine is regarded as the 21st amino acid and has specific genetic codon for its incorporation in to proteins. The groups of proteins that contain selenocysteine as an integral part of their polypeptide chain are defined as selenoproteins and these proteins are responsible for most of the physiological functions mediated by selenium. Selenoproteins play important roles in cellular antioxidative protection, redox regulation, thyroid function and immune function.^{31,32} The most important and well studied selenoprotein is glutathione peroxidase (GPx).

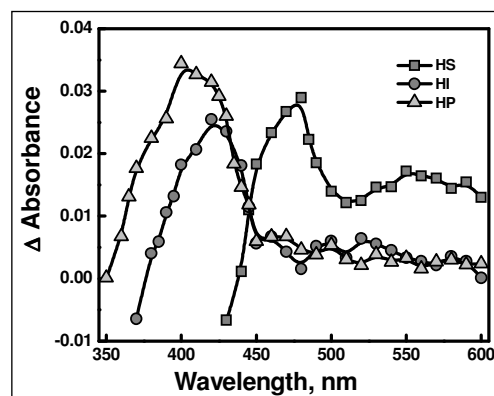
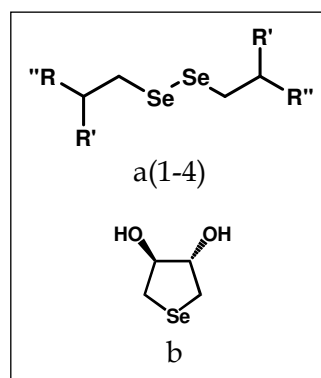


Figure 4: Transient absorption spectrum for the reaction of $\text{CCl}_3\text{O}_2^\bullet$ with $100 \mu\text{M}$ of HS, HI and HP respectively. (Dose 25 Gy/pulse)



	R'	R''
a1. Selenocystine (SeCys)	COOH	NH_3^+Cl^-
a2. Selenocystamine (SeA)	H	NH_3^+Cl^-
a3. Diselenodipropionic acid (SeP)	COOH	H
a4. Methyl ester of diselenodipropionic acid (MeSeP)	COOCH_3	H
b. 3,4-dihydroxy-1-selenolane (DHS)		

Scheme 3: Structures of organo selenium compounds

GPx is an antioxidant enzyme that detoxifies peroxides and protects the cells against oxidative stress. Selenocysteine is the active site of GPx enzyme and is directly involved in catalytic reactions. There are lot of interest to develop selenoether and diselenide derivatives of selenocystine as an antioxidant and radioprotectors. Some representative selenium compounds of the above category used in the study is shown in scheme 3. The transient spectra of $\text{CCl}_3\text{O}_2^\bullet$ radical with SeP and DHS

Table 2: Bimolecular rate constant of organo selenium compounds with $\text{CCl}_3\text{O}_2^\bullet$ radical

Compounds	Rate constant, $\text{M}^{-1}\text{s}^{-1}$
SeCys	Not detected
SeA	8.3×10^6
SeP	1.7×10^8
MeSeP	1.1×10^8
DHS	3.2×10^8

have absorption maxima at 560 nm and 480 nm respectively.^{22,33,34} Upon comparison transient spectra with azide radical it was confirmed that the reaction occurs through electron transfer. The bimolecular rate constant for the reaction of $\text{CCl}_3\text{O}_2^\bullet$ radicals with DHS was estimated from the formation kinetics at 480 nm and value from the same was $3.2 \times 10^8 \text{ M}^{-1}\text{s}^{-1}$. For the diselenides other than SeP, the transient absorption was weak to estimate the rate constant directly. From competition kinetics the rate constants with the $\text{CCl}_3\text{O}_2^\bullet$ radicals and diselenides were estimated and listed in the table 2.

Due to solubility limitation of SeCys at neutral pH, it was difficult to reach the required concentration to have competition among the reactants. The above studies with $\text{CCl}_3\text{O}_2^\bullet$ radicals

indicated that SeP was easier to oxidize compared to its other analogue.

Conclusion

In this article the reactions of model peroxy ($\text{CCl}_3\text{O}_2^\bullet$) radical with different types of compounds have been studied. Though the primary mode of reaction for $\text{CCl}_3\text{O}_2^\bullet$ radicals was through electron transfer, but there were instances where addition reaction was also observed. Steric crowding around the attacking site for $\text{CCl}_3\text{O}_2^\bullet$ radicals was also one of the factors to govern the reaction mechanism. From the comparative bimolecular rate constant for $\text{CCl}_3\text{O}_2^\bullet$ radicals with different compounds helped to understand the structure activity relationship and to design and develop an efficient peroxy radical scavenger.

Acknowledgement

The authors acknowledged all the co-authors of our published papers cited in the references. We are also thankful to head RPCD for encouragement and support.

References

1. C. J. Koch, In Oxygen effects in radiobiology, Advances in Experimental Medicine and Biology, Springer, Boston, MA, 1982.
2. P. Neta, R. E. Huie and A. B. Ross, J. Phys. Chem. Ref Data, 1990, 19, 413-515.
3. S. Kitao, K. Fujii, M. Teramoto, K. Harada, M. Ando and Y. Tamura, Food Sci. Technol. Res., 2005, 11, 318-323.
4. C. von Sonntag and H. P. Schuchmann, Angew. Chem. Int. Ed. Engl., 1991, 30, 1229-1253.
5. J. Aikens and T. A. Dix, J. Biol. Chem., 1991, 266, 15091-15098.
6. J.M. Gebicki, Arch. Biochem. Biophys., 2016, 595, 33-39.
7. R. Kohen and A. Nyska, Toxicol. Pathol., 2002, 30, 620-650.
8. M. Repetto, J. Semprine and A. Boveris, Intech open access chapter <http://dx.doi.org/10.5772/45943>
9. H. Sies, Am. J. Med., 1991, 91, 31-38.
10. E. M. Fielden, In The Study of Fast Processes and Transient Species by Electron Pulse Radiolysis, Reidel Publishing, London, 1984; pp 59.
11. G. V. Buxton, C. L. Greenstock, W. P. Helman and A. B. Ross, J. Phys. Chem. Ref. Data, 1988, 17, 513-886.
12. P. Neta and R. E. Huie, J. Phys. Chem. Ref. Data, 1988, 17, 1027-1227.
13. A. Barik, K. I. Priyadarsini and H. Mohan, Res. Chem. Intermed., 2006, 32, 837-845.
14. X. Shen, J. Lind, T. E. Eriksen and G. Merenyi, J. Phys. Chem., 1989, 93, 553-557.

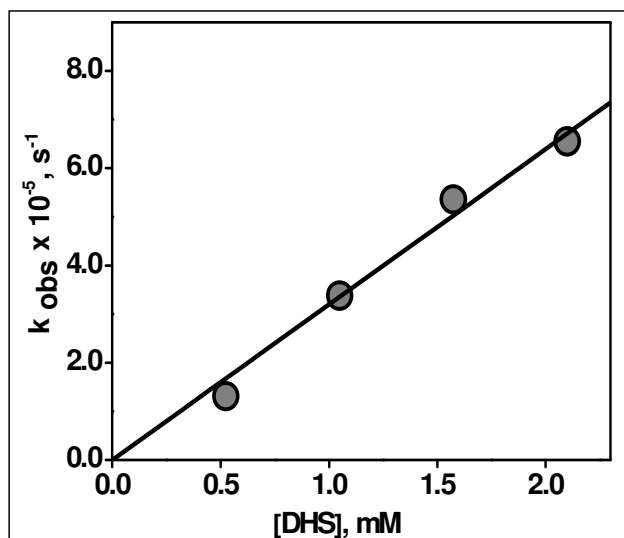


Figure 5: Linear plot for the observed rate of formation (k_{obs}) of the transient due to reaction of $\text{CCl}_3\text{O}_2^\bullet$ radical with varying concentration DHS at 480 nm at pH 7 (Dose 25 Gy/pulse).

15. J. Mönig, D. Bahnemann and K. D. Asmus, Chem. Biol. Interact., 1983, 47, 15-17.
16. R. Flyunt, O. Makogon and K. D. Asmus, Radiat. Phys. Chem., 2002, 65, 299-307
17. S. N. Guha, P. N. Moorthy, K. Kishore, D. B. Naik and K. N. Rao, Proc. Indian Acad.Sci. (Chem. Sci.), 1987, 99, 261-271.
18. U. Singh, A. Barik and K. I. Priyadarsini, Bioorg. Med. Chem., 2009, 17, 6008-6014
19. G. V. Buxton and C. R. Stuart, J. Chem. Soc. Faraday Trans., 1995, 91, 279-281.
20. T. N. Das, T. Dhanasekaran, Z. B. Alfassi, and P. Neta, J. Phys. Chem. A 1998, 102, 280 -284.
21. U. Singh, A. Barik, B. G. Singh and K. I. Priyadarsini, Free Radic. Res., 2011, 45, 317-325.
22. B. Mishra, A. Barik, A. Kunwar, L. B. Kumbhare, K. I. Priyadarsini and V. K. Jain, Phosphorus Sulfur and Silicon, 2008, 183, 1018-1025.
23. S. M. Shaikh, A. Barik, B. G. Singh, R. V. Madukuri, N. V. Balaji, G. V. Subbaraju, D. B. Naik and K. I. Priyadarsini, Free Radic. Res., 2016, 50, 1361-1373
24. S. S. Kumar, A. Ghosh, T. P. A. Devasagayam and P. S. Chauhan, Mutation Res., 2000, 469, 207-214.
25. K. Watanabe, T. Ohta and Y. Shirasu, Mutation Res., 1989, 218, 105-109.
26. A. Barik, K. I. Priyadarsini and H. Mohan, Radiat. Phys. Chem., 2004, 70, 687-696.
27. K. I. Priyadarsini, Free Radic. Biol. Med., 1997, 23, 838 - 843.
28. N. A. Ali, R. Jansen, H. Pilgrim, K. Liberra and U. Lindequist, Phytochemistry, 1996, 41, 927-929.
29. W. Chen, F. Y. He and Y. Q. Li, J. Ethnopharmacol., 2006, 105, 280-285.
30. N. V. Balaji, M. V. Ramani, A. G. Viana, L. P. Sanglard, J. White, V. Mulabagal, C. Lee, T. J. Gana, N. O. Egiebor, G. V. Subbaraju and A. K. Tiwari, Bioorg. Med. Chem., 2015, 23, 2148-2158.
31. P. Brenneisen, H. Steinbrenner and H. Sies, Mol. Aspects Med. 2005, 26, 256-267.
32. D. Behne, A. Kyriakopoulos, Annu. Rev. Nutr., 2001, 21, 453-473.
33. A. Kunwar, B. Mishra, A. Barik, L. B. Kumbhare, R. Pandey, V. K. Jain and K. I. Priyadarsini, Chem. Res. Toxicol., 2007, 20, 1482-1487.
34. B. G. Singh, E. Thomas, F. Kumakura, K. Dedachi, M. Iwaoka and K. I. Priyadarsini, J. Phys. Chem. A, 2010, 114, 8271-8277.



Mr. Shaukat Ali M. Shaikh obtained his M. Sc. Degree in Chemistry from Ismail Yusuf College, University of Mumbai, Mumbai, India in 2013. He then joined BARC-University of Mumbai collaborative Ph.D. programme for his doctoral studies in 2014. He is presently in final year of Ph. D. and already submitted a synopsis under the guidance of Dr. D. B. Naik (BARC). His research focus is on radiation and photochemical studies of new curcumin and hispolon derivatives.



Mrs. Rupali G. Shinde obtained her M. Sc. Degree in Chemistry from Department of Chemistry, Savitribai Phule Pune University (SPPU), Pune, India in 2013. She then joined BARC-SPPU collaborative Ph.D. programme for her doctoral studies in 2014. She is presently in final year of Ph. D. and already submitted a synopsis under the guidance of Dr. Atanu Barik (BARC) and Dr. Ayesha Khan (SPPU). Her research focus is on radiation and photophysical studies of coumarin and its derivatives.



D. Atanu Barik obtained M. Sc. degree in Chemistry from Burdwan University (West Bengal) in 1999. After graduating from BARC Training School in 2000, he joined Radiation & Photochemistry Division, BARC. He has obtained Ph. D. degree in Chemistry from University of Mumbai in the year 2006. During the year 2007-2008 he was post doctoral fellow at Laboratoire de Radiolyse, CEA Saclay, France. He is actively involved in free radical chemistry and excited state properties of molecules employing photochemical and radiation chemical techniques.

“Super-Strong” van der Waals Complexes involving Noble Gases

Ayan Ghosh^{a,c} and Tapan K. Ghanty^{*,b,c}

^aLaser and Plasma Technology Division, Beam Technology Development Group,
Bhabha Atomic Research Centre, Mumbai 400 085, INDIA.

^bTheoretical Chemistry Section, Chemistry Group, Bhabha Atomic Research Centre,
Mumbai 400 085, INDIA.

^cHomi Bhabha National Institute, Training School Complex, Anushakti Nagar, Mumbai 400094, INDIA.

Abstract

For a long time noble gases have been considered as inert and highly unreactive elements in the periodic table. However, in 1933, Pauling predicted the possibility of formation of stable molecules by heavier noble gas atoms such as Kr and Xe in view of the fact that their valence electrons are far away from their nuclei and less strongly bound and more susceptible to chemical bond formation. Pauling's prediction became a reality with the synthesis of first noble gas compound, XePtF₆ by Bartlett in 1962. Though there have been many reports on various noble gas compounds, however, noble gas atoms are mainly more prone to form van der Waals (vdW) complexes with various molecules and ions where weak interactions are involved. In the recent past it has been shown that noble gas atoms are also capable of forming strong vdW complexes. In this article we review our recent findings on few super-strong vdW complexes, which are predicted through high level *ab initio* based theoretical techniques.

I. Introduction

The macroscopic physical properties of the noble gases are primarily dominated by the weak van der Waals forces acting between the atoms. Going down the group from helium to radon, the attractive force increases with the increase in size of the atoms which in turn increase the polarizability resulting into an enhancement of melting point, boiling point, enthalpy of vaporization, and solubility. One unique feature of helium is its exceptionally low melting and boiling points compared to any known substance exhibiting its superfluidity. In order to make solid helium, one has to apply a huge pressure of 2500 kPa at a temperature of 0.95 K (−272.2°C).¹ One more important physical parameter is density, which is increased with the increase in atomic weight of the noble gas atoms while going down the group from helium to radon.

In general, the chemical properties of an atom exclusively depend on the number of electrons in the outermost occupied orbital known as valence shell. In 1916, both W. Kossel²

and G. N. Lewis³ reported and highlighted the electronic configuration of noble-gas atom, which was found to be the most stable electronic configuration among all the elements exists in nature. According to them, there was always a tendency of all the elements to get the stable neighbouring noble gas electronic configuration by gaining or losing electron(s). Since all the atoms had inherent affinity to obtain the electron arrangements of the nearest noble gas atoms, therefore the chemical inertness of the noble gases was self evident.

All the noble gases have closed shell structures with full valence eight electrons usually represented by the group term ‘octet’, ns^2np^6 , except helium having two electrons in the outermost shell possesses ‘duet’, $1s^2$, with closed shell electronic arrangement. Since noble gas atoms are extremely stable due to full valence electron shell, therefore, they do not have a tendency to form chemical bond with the other elements by gaining or losing any electron(s).⁴

This fact clearly indicates the inert nature of the noble gas atoms. Considering the most stable electronic configuration among all the elements of the periodic table, Mendeleev labelled the noble gas atoms as 'Group 0' and placed them in the periodic table in a separate group since the valency of the noble gas atoms is zero. In this context, it is important to emphasize that being the most stable electronic arrangement 'noble gas notation'⁵ is widely used to represent any electronic configuration of any other element in the periodic table. For example, the electronic configuration of sulphur atom is $1s^2 2s^2 2p^6 3s^2 3p^4$, which can be written in terms of 'noble gas notation' as $[\text{Ne}] 3s^2 3p^4$.

After the pioneering discovery of first noble gas compound, $\text{Xe}[\text{PtF}_6]$,⁶ by Bartlett, scientists all over the world were very keen to explore the field of noble gas chemistry by synthesizing various kinds of noble gas compounds. The first neutral argon compound, HArF ,⁷ was prepared experimentally at cryogenic conditions and was characterized using low temperature matrix isolation infrared spectroscopic technique by Khriachtchev *et al.*. The successful identification of the HArF molecule, associated with H–Ar covalent bonding, has revolutionized the field of 'noble gas chemistry'. Since then, noble gas chemistry has become an enthralling field of research for both theoreticians and experimentalists and has experienced a renaissance during the past two decades,^{8–16} and today it is one of the frontier areas of research in chemical sciences involving both theory and experiment. Subsequently, a unique category of novel noble gas hydrides of the type HNgY (Ng = Ar, Kr, and Xe; Y = electronegative element or group) has received considerable attention among researchers and broaden the scope of the field of noble gas chemistry.^{7–11} Various ionic or neutral insertion molecules of noble-gas atoms with environmentally important species, such as HOX ¹² (X = Cl, Br, F) and species of astronomical significance, like HCO^+ ,¹³ HN_2^+ ,¹⁴ and so on, have been theoretically investigated using various computational methods. In this

context, it is essential to emphasize that the noble gas-containing compounds had not hitherto been detected in space before the detection of noble gas hydride cations ($^{36}\text{ArH}^+$) in the Crab Nebula by Barlow and co-workers.¹⁵ Of late, one of the noble-gas insertion molecules, HXeOBr , has been successfully prepared and characterized using IR spectroscopic technique by Khriachtchev *et al.*,¹⁶ which was theoretically predicted by our group earlier.¹²

The bonding between noble gas and noble metal is unusual since both are extremely reluctant to form chemical bond due to their inert nature. Schröder *et al.* first experimentally identified chemical compounds involving noble gas and noble metal, XeAu^+ and XeAuXe^+ , by mass spectrometry in 1998,¹⁷ although they were first conceived by Pyykkö, who predicted the stability of the species theoretically in 1995.¹⁸ In 2000, Seidel and Seppelt¹⁹ had successfully isolated the first complex $[\text{AuXe}_4][\text{Sb}_2\text{F}_{11}]_2$ containing noble gas–noble metal bond which is found to be thermally stable. The AuXe_4^{2+} salt consists of four Xe atoms acting as Lewis bases coordinate the divalent gold central metal ion in more or less square planer arrangement.

The accidental finding of pure rotational spectra of ArAuCl and KrCuCl with the cavity pulsed-jet FTMW spectrometer by Gerry *et al.*²⁰ opens the gate of a new arena in the chemical sciences, where noble metal–noble gas bonding has been observed. Subsequently, a series of compounds containing Ng–M bond (Ng = Ar, Kr, and Xe; M = Au, Ag, and Cu), *viz.*, NgMX (X = F, Cl, and Br) have been investigated both experimentally as well as theoretically.²¹ In all these compounds, the noble gas–noble metal bondings are partially covalent in nature and strong interactions exist between the two closed-shell fragments, *viz.*, noble gas and noble metal halides. *Ab initio* density functional theory have been employed to investigate the geometries and bond energies of the He-MX , Ne-MX , and Ar-MX (M = Cu, Ag, Au; X = F, Cl) complexes by Wright *et al.*²²

Apart from fundamental interests on the structure and bonding in noble gas compounds, trapping of radioactive xenon and krypton generated during nuclear fission processes is very important. Thus, one of the major issues in nuclear fuel reprocessing and reactor accidental scenarios is to manage radioactive fission gases including xenon and krypton. Due to the extreme inert nature of noble gases, it is very difficult to trap the radioactive noble gases in suitable matrix by van der Waals interactions using simple physisorption process. It is well known that the metal-organic frameworks (MOFs) are extensively used to absorb and separate various gases including noble gases due to its high intake capacity, better selectivity and tunable chemical properties. Theoretical modelling is necessary to select the suitable MOFs required for radioactive noble gas adsorption/separation. The binding strength at different adsorption sites are favored by van der Waals interactions between the noble gas atoms with MOFs network. In recent times, Thallapally and co-workers have exhaustively studied the adsorption of Ng atom with a large number of MOF systems, *viz.*, Sb-MOF-2,²³ Ni/DOBDC,²⁴ Sb-MOF-1,²⁵ FMOFCu,²⁶ M-MOF-74,²⁷ etc. It has been well established that the successful deposition of Ag nanoparticles in porous MOF-74Ni (or Ni/DOBDC) significantly enhances the noble gas adsorption process in Ag@MOF-74Ni.²⁸ Very recently, our group has reported that the creation of active centers in the lattice by doping hetero atom in graphene considerably increase the adsorption of fission gases Xe and Kr on pristine and doped graphene.²⁹

In addition to the noble gas-noble metal bonding the chemistry of gold³⁰ is shown to be very rich. For instance, recent experimental investigation reveals that single gold atom can exhibit chemistry analogous to the hydrogen atom in SiAu_n clusters.³¹ The unusual chemistry of gold is mostly due to the strong relativistic effects,³⁰ which stabilize the valence 6s orbital and destabilize the 5d orbitals of gold resulting into decrease in size of former as compared

to that of the latter. Hydrogen like chemical behavior of gold is also supported by the similar electronegativity of gold and hydrogen atom. In the recent past, it has been verified that gold atom mimicks a hydrogen atom in the hydrogen-bonded complex of AuOH with water.³² Earlier our group have explored the feasibility study of noble gas inserted compounds, MNgF and MNgOH (M = Cu, Ag, and Au; Ng = Ar, Kr, and Xe) using *ab initio* quantum chemical calculations.³³

As mentioned, noble gas-noble metal bonding has been investigated extensively over the years; however, Fielicke and co-workers.³⁴ has pointed out that the nature of this kind of bonding has been controversial.³⁴ Moreover, they proposed trimeric coinage metal cluster as a prototype system to understand the nature of Ar-M bonding (M = Ag and Au). They also showed that the total Ar binding energy in Au₃⁺·Ar₃ is significantly higher than that in Ag₃⁺·Ar₃ (cf. 81.1 vs 43.4 kJ mol⁻¹). Moreover, they have shown that Ar atoms in the Ag₃⁺·Ar₃ complex act merely as messengers while the same participate in conventional Ar-Au chemical bonding in the Au₃⁺·Ar₃ complex and thereby modify the experimentally observed IR spectra significantly. Also, the Ar-M bond energy in ArAg₃⁺ complex (15.4 kJ mol⁻¹) is found to increase with the replacement of Ag with Au atom and finally reaches 29.9 kJ mol⁻¹ in the ArAu₃⁺ complex.

In this context, our objective has been to see whether the noble gas-noble metal binding energy can be increased further or not. To accomplish our objective we have considered various hydrogen-doped gold trimers, which is motivated by the gold-hydrogen analogy as proposed^{30-33,35} in the recent past and subsequently investigated by others for various systems.³⁶ In this context it may be noted that both hydrogen-doped noble metal clusters and H₂ adsorbed gold clusters have been shown to behave as a better catalyst in the oxidation of carbon monoxide;³⁷ however, the catalytic activity is found to be

almost unchanged when the Au_{20} cluster is doped with hydrogen atom.³⁸ Hence, it is further interesting to study the change in the nature and extent of Ng–Au bonding in NgAu_3^+ through successive hydrogen doping (replacement of Au atom(s) with H atom(s)). In this context, it is important to mention that the hydrogen-doped noble metal clusters have been investigated experimentally as well as theoretically.³⁹ In this article we review our recently published work on few super-strong vdW complexes, which are predicted through high level computational techniques.⁴⁰

II. Computational Details

We have used density functional theory (DFT) with the dispersion-corrected ω separated form of Becke's 1997 hybrid functional with short-range HF exchange (ω B97X-D) functional,⁴¹ second-order Møller–Plesset perturbation theory (MP2),⁴² and coupled-cluster theory with the inclusion of single and double excitations and an estimate of connected triples (CCSD(T))⁴³ to investigate the optimized geometrical structures and stabilities of the predicted ions. We have employed GAMESS⁴⁴ and MOLPRO-2012⁴⁵ softwares for all the calculations. In the frozen core approximations up to 3d and 4d orbitals for silver and gold, respectively, and 2p orbital for both copper and argon atoms, electrons are kept in the core for the ADF calculations, and the corresponding Slater type orbital TZ2P⁴⁶ basis sets have been used. Zeroth-order regular approximation (ZORA) has been used to take into account the scalar relativistic effects. Energy decomposition analysis (EDA)⁴⁷ of the total interaction energy has been performed to obtain the interaction energies between the two fragments (Ng and $\text{M}_{3-k}\text{H}_k^+$) in the $\text{NgM}_{3-k}\text{H}_k^+$ complexes. For this ADF 2013⁴⁸ software has been used with PBE-D3 functional (Perdew–Burke–Ernzerhof with dispersion correction). The total interaction energy, ΔE_{int} can be represented in terms of four components, *viz.*,

$$\Delta E_{\text{int}} = \Delta E_{\text{elec}} + \Delta E_{\text{Pauli}} + \Delta E_{\text{orb}} + \Delta E_{\text{dis}} \quad (5.1)$$

where ΔE_{elec} and ΔE_{Pauli} represent the

electrostatic interaction energy and the Pauli repulsive energy, respectively, between the fragments. ΔE_{orb} is the stabilizing orbital interaction term, which includes polarization term and covalency factor due to the overlap between the noble gas and noble metal orbitals. The term ΔE_{dis} denotes the dispersion energy.

Three approaches have been considered to take into account the relativistic effects, namely, (i) Use of relativistic effective core potential with def2-TZVPD basis sets (RECP), (ii) Scalar relativistic method with TZ2P basis set (SCL) and (iii) Use of explicit spin-orbit interaction with TZ2P basis set (SO). The optimized Xe–Au bond length, bond dissociation energy, and HOMO–LUMO energy gap for $\text{XeAu}_k\text{H}_{3-k}^+$ ($k = 1-3$) species have been calculated. The energy decomposition analysis (EDA) analysis has also been carried out using scalar relativistic approach.

III. Results and Discussions

III. A. Structural Parameters

First we discuss the structural parameters of various ions considered here. The minimum energy structures for the Au_3^+ , Au_2H^+ , and AuH_2^+ ions are found to be planar in their respective potential energy surfaces. The interaction of Ng atom with these ions leads to the formation of strongly bonded NgAu_3^+ , NgAu_2H^+ , and NgAuH_2^+ complexes, the optimized structures of which are depicted in Figure 1 showing the variation of Ng–Au bond lengths in these complexes. The CCSD(T) calculated Ar–Au bond length value is decreased from 2.605 Å in ArAu_3^+ to 2.518 Å in ArAu_2H^+ and 2.429 Å in ArAuH_2^+ , respectively. This trend suggests that the Ng–Au interaction is increased considerably in ArAuH_2^+ species. It further indicates that the Ng–Au bond strength is enhanced drastically with the doping of two hydrogen atoms in a pure Au trimer cation. In this context it is interesting to note that the calculated Ng–Au bond length values in NgAu^+ are generally larger (2.537, 2.553, and 2.617 Å in ArAu^+ , KrAu^+ , and XeAu^+ , respectively) than

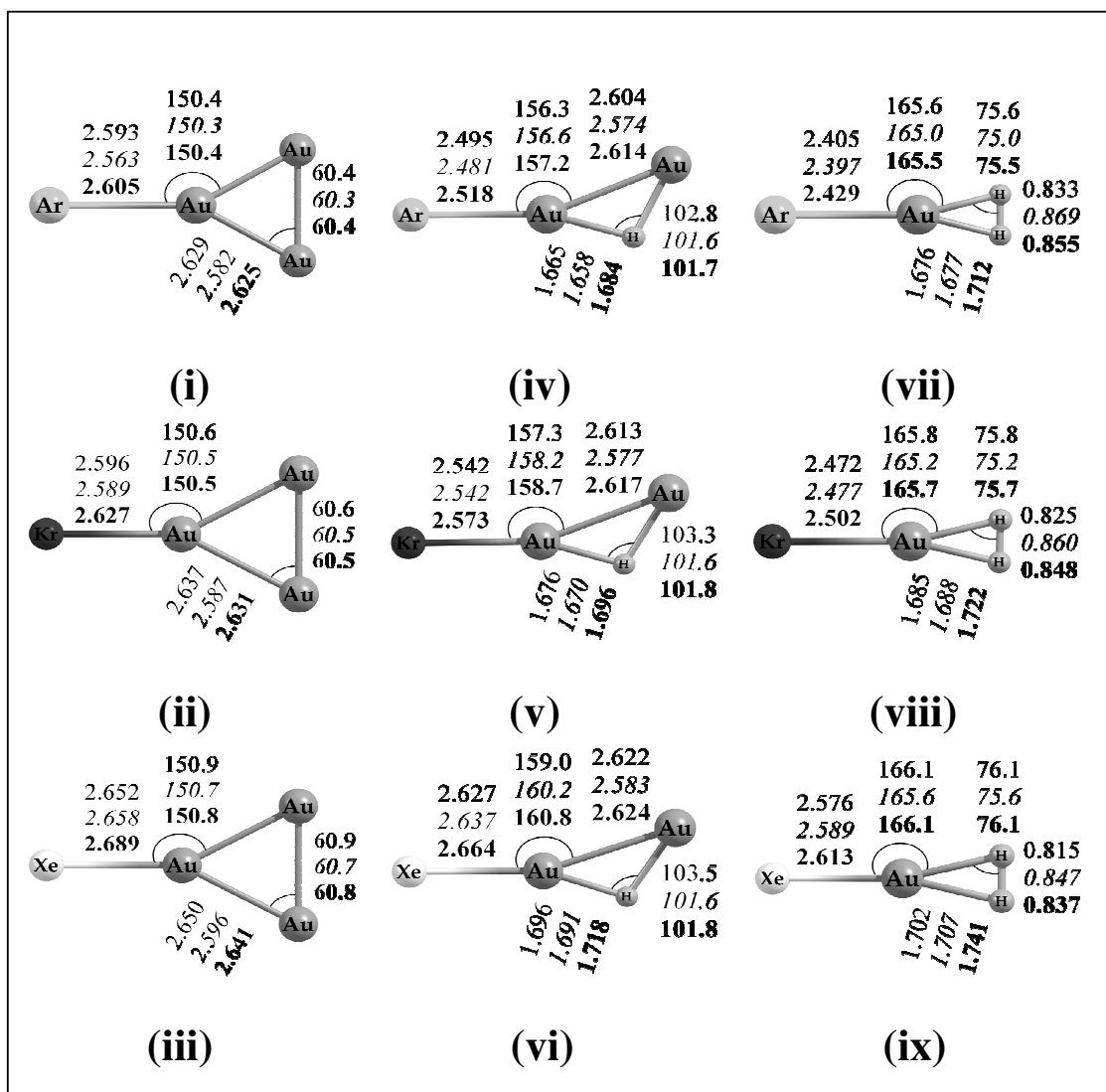


Figure 1. Optimized geometrical parameters in graphical format for planar structures of NgAu_3^+ (i, ii, iii), NgAu_2H^+ (iv, v, vi), and NgAuH_2^+ (vii, viii, ix) (Ng = Ar, Kr, Xe) where the bond lengths are in Å and bond angles are in degrees. The values in normal, italic, and bold face are computed at the $\omega\text{B97X-D/DEF2}$, MP2/DEF2, and CCSD(T)/AVTZ levels of theory, respectively.

that in the NgAuH_2^+ complexes, which again implies that the Ng–Au bond is stronger in the latter complexes.

Following the work of Gerry and co-workers,⁴⁹ we have analyzed the Ng–Au bond length with respect to the covalent limit (R_{cov}) and van der Waals limit (R_{vdW}). The R_{cov} values obtained from the recently reported literature⁵⁰ are 2.20, 2.41, and 2.55 Å for Ar–Au, Kr–Au and Xe–Au bond, respectively, and the corresponding R_{vdW} ⁵¹ values are 4.15, 4.57, and 4.38 Å. The R_{cov} , R_{vdW} and the Ng–Au bond length values reported

in Figure 1 clearly indicate that the Ng–Au bond length values in $\text{NgAu}_{3-k}\text{H}_k^+$ ($k = 0-2$) are in close proximity with the covalent limits. Also, a slightly larger value of the calculated Ng–Au bond length as compared to the corresponding R_{cov} value in the $\text{NgAu}_{3-k}\text{H}_k^+$ species implies that both covalent and dispersion interactions are likely to coexist in the Ng–Au bonding.

^aBond dissociation energy is calculated using CCSD(T) method, and stretching frequency and force constant values have been calculate using MP2 method.

Table 1. Calculated Bond Dissociation Energy (BE in kJ mol⁻¹) and the Stretching Frequency (ν in cm⁻¹) and Force Constant (k in N m⁻¹) Values for Ng–Au Bond in NgAu₃⁺, NgAu₂H⁺ and NgAuH₂⁺ Species^a

Ions	BE (Ng–Au)			ν (Ng–Au)			k (Ng–Au)		
	Ar	Kr	Xe	Ar	Kr	Xe	Ar	Kr	Xe
NgAu ₃ ⁺	31.9	50.7	81.2	120.5	116.7	114.1	39.4	60.3	81.0
NgAu ₂ H ⁺	47.5	69.3	102.4	142.2	126.3	116.4	63.4	81.1	95.6
NgAuH ₂ ⁺	72.0	100.7	142.0	223.2	183.0	166.2	97.8	115.2	125.3

III.B. Dissociation Energies

The zero-point energy (ZPE) and basis set superposition error (BSSE)-corrected Ng–Au bond dissociation energy for various ions are reported in Table 1, which clearly indicate that the predicted species are more stable than the dissociated products for the dissociation channel, NgAu_{3-k}H_k⁺ → Ng + Au_{3-k}H_k⁺. The Ng–Au binding energy in NgAuF and NgAu⁺ are also calculated and found to be 46.0, 44.1 kJ mol⁻¹ in Ar-complexes, 64.4, 73.5 kJ mol⁻¹ in Kr-complexes, and 92.4, 121.6 kJ mol⁻¹ in Xe-complexes, respectively. All these calculated Ng–Au bond energy values clearly indicate that the Ng–Au bonding interaction not only is greatly enhanced with the hydrogen doping in pure Au trimers but also is found to be greater than that in the NgAuF and NgAu⁺ species. With respect to the bond energy values, the Ng–Au bonding interaction has been found to be increased by 2.26 times for Ar, 1.99 times for Kr, and 1.75 times for Xe complexes in going from NgAu₃⁺ to NgAuH₂⁺ complex. Hence, it is quite obvious that the increase in the Ng–Au bonding interaction is more pronounced in the case of Ar containing H-doped Au trimers in comparison with the corresponding Kr and Xe complexes. All these calculated results evidently imply the importance of H doping in enhancing the noble gas–noble metal bonding strength drastically.

III.C. Vibrational Frequencies

For all the noble gas containing ions vibrational frequencies are calculated to confirm that all these species are optimized to the true minima in their respective potential energy surfaces.

Subsequently, we have analysed the Ng–Au stretching vibrational frequency along with the force constant values with all levels of theory. Since MP2 method is able to provide calculated frequency values which are close to the corresponding experimental frequencies, we have listed the MP2/DEF2 calculated frequency values Table 1. There is a remarkable change in the calculated Ng–Au stretching frequency value in going from NgAu₃⁺ to NgAuH₂⁺ species. For instances, a change from 120.5 to 223.2 cm⁻¹ in Ar, 116.7 to 183.0 cm⁻¹ in Kr, and 114.1 to 166.2 cm⁻¹ in Xe containing complexes in going from NgAu₃⁺ to NgAuH₂⁺ species, respectively, are observed. In a similar way, the corresponding force constant values are changed from 39.4 to 97.8 N m⁻¹ in Ar, 60.3 to 115.2 N m⁻¹ in Kr, and 81.0 to 125.3 N m⁻¹ in Xe containing complexes (Table 1). The trends in the Ng–Au stretching frequency and force constant values are in good agreement with the corresponding structural parameters and the bond dissociation energy values.

III.D. Description of Molecular Orbitals

The molecular orbitals depicting the Ar–Au bonding represented in Figure 2 reveal that the π orbitals from both Ar and Au are involved in the bonding and the nature of the Ar–Au interaction in all the three species, ArAu₃⁺, ArAu₂H⁺ and ArAuH₂⁺ is found to be almost the same. However, the highest occupied molecular orbital (HOMO) corresponding to the Ar–Au bonding in ArAuH₂⁺ ion is found to be the most stabilized. In view of significant differences in various bonding parameters as discussed above, it is interesting to analyze the enhancement of the Ng–Au binding

energy in terms of the HOMO and LUMO (lowest unoccupied molecular orbital) energy of the precursor species and their complexes. The Ar–Au bond energy has been shown to correlate very well with the LUMO energy of the precursor ion (Figure 3).

The ω B97X-D/DEF2 computed LUMO energy for Au_3^+ , Au_2H^+ , and AuH_2^+ species have been found to be -6.66 , -7.27 , and -8.12 eV, respectively, whereas the HOMO energy for Ar, Kr, and Xe are -13.93 , -12.71 , and -11.34 eV, respectively. Therefore, through successive replacement of Au atom(s) by the H atom(s) in pure Au trimer, the LUMO of the $\text{Au}_{3-k}\text{H}_k^+$ species has been stabilized more and more, resulting in decreases in the energy gap between the HOMO of Ng and LUMO of AuH_2^+ , leading to the formation of the most stable Ng–Au bond in NgAuH_2^+ complexes, among all the complexes discussed here. This is one of the most important factors for the enhancement of Ng–Au bonding interaction on doping with a hydrogen atom in the pure Au trimer. The HOMO–LUMO energy gaps of 7.88,

8.92, and 11.11 eV in Ar-complexes, 7.86, 8.97, and 11.23 eV in Kr-complexes, 7.81, 9.00, and 11.20 eV in Xe-complexes in the NgAu_3^+ , NgAu_2H^+ , and NgAuH_2^+ species, respectively, are also found to be significantly higher as compared to that for the respective precursor, Au_3^+ , Au_2H^+ , and AuH_2^+ . Moreover, this increase of the HOMO–LUMO gap is the maximum for the AuH_2^+ ion, which is in agreement with the highest stability of the NgAuH_2^+ complex. It is also important to note that the Ar–Au⁺ bond energy is lower than that in the Ar– AuH_2^+ species, although the LUMO of Au^+ (-9.73 eV) is more stable. It is because of the limited scope of charge reorganization in Ar–Au⁺ ion as compared to that in the Ar– AuH_2^+ ion. Hence, the HOMO–LUMO gap of the Au^+ ion (9.12 eV) remains almost the same as in the Ar–Au⁺ ion (9.02 eV). Here it may be noted that the performance of ω B97X-D functional in predicting the HOMO–LUMO gap is very good as compared to that of the other density functionals.

III.E. Charge Distribution Analysis

For analysis of the charge distributions, the partial atomic charges have been calculated using NBO approach within the framework of MP2 method and the values are reported in Table 2.

^aCharge corresponding to the Au atom bonded with the Ng atom is represented in boldface.

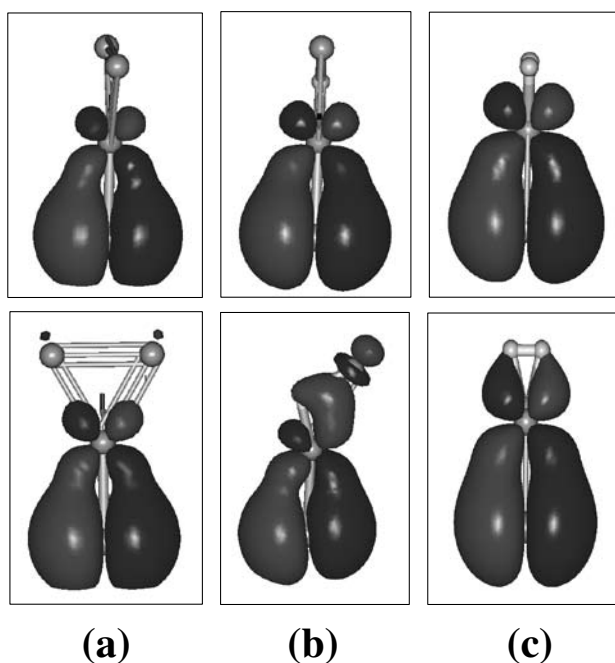


Figure 2. Degenerate molecular orbitals depicting the Ar–Au bonding in (a) ArAu_3^+ , (b) ArAu_2H^+ , and (c) ArAuH_2^+ with Orbital energy of -18.86 , -19.65 and -20.90 eV, respectively.

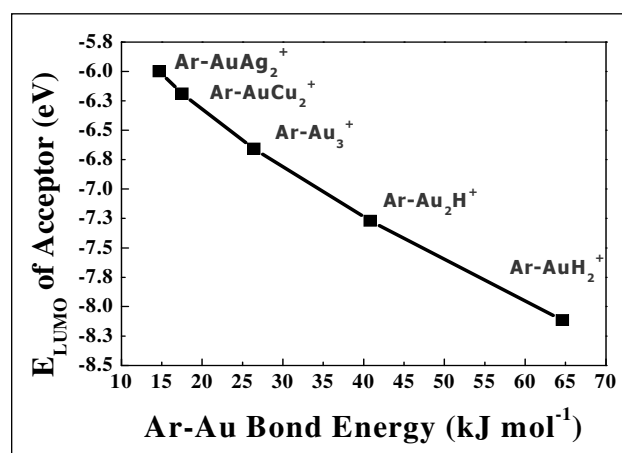


Figure 3. Plot of the Ar–Au bond energy vs the LUMO energy, calculated using ω B97X-D/DEF2 Method (Correlation Coefficient corresponding to linear least square fit, $R^2 = 0.988$).

Table 2. Values of the Atomic Charges in Au_3^+ , Au_2H^+ , AuH_2^+ , NgAu_3^+ , NgAu_2H^+ and NgAuH_2^+ Species (Ng = Ar, Kr, and Xe) Calculated using MP2/AVTZ Method.

Species	Atoms	Cation	Ar	Kr	Xe
Au_3^+ / Ng		...	0.076	0.123	0.202
NgAu_3^+	Au1 ^a	0.333	0.291	0.264	0.215
	Au2	0.333	0.317	0.306	0.291
	Au3	0.333	0.317	0.306	0.291
Au_2H^+ / Ng		...	0.107	0.174	0.259
NgAu_2H^+	Au1 ^a	0.627	0.513	0.445	0.376
	Au2	0.627	0.619	0.603	0.580
	H	-0.254	-0.240	-0.222	-0.215
AuH_2^+ / Ng		...	0.145	0.219	0.315
NgAuH_2^+	Au ^a	0.925	0.716	0.634	0.545
	H1	0.037	0.070	0.073	0.070
	H2	0.037	0.070	0.073	0.070

The calculated NBO charges (Table 2) indicate that the positive charge residing on the metal atom is increased considerably in going from the Au_3^+ ($q_{\text{Au}} = 0.333$ a.u.) to AuH_2^+ ($q_{\text{Au}} = 0.925$ a.u.) ion. Since Au atom is more positively charged in the AuH_2^+ species, the electron density transfer from the HOMO of the Ng atom to the LUMO of the AuH_2^+ species is more. It leads to the formation of a stronger Ng–Au bond. Moreover, the NBO charge on the Au atom in $\text{Au}_{3-k}\text{H}_k^+$ is decreased on complexation with Ng and the extent of decrease is the maximum in the AuH_2^+ ion (from 0.925 to 0.716, 0.634, and 0.545 a.u. in ArAuH_2^+ , KrAuH_2^+ , and XeAuH_2^+ , respectively) among all the Au containing trimers because of the lowest LUMO energy of the AuH_2^+ ion. As a result, charge transfer from the Ng atom to the trimer cation is also found to be the maximum in the case of the Ng– AuH_2^+ complex. It implies that charge reorganization in AuH_2^+ is the maximum after complexation, indicating an increase in the charge-induced dipole interaction in the series $\text{Ng–Au}_3^+ < \text{Ng–Au}_2\text{H}^+ < \text{Ng–AuH}_2^+$.

III.F. Comparative Accounts of NgAuH_n^+ Ions with NgAgH_n^+ and NgCuH_n^+ Ions

In addition to the Ng–Au bonding, it is also interesting to study the trends in Ng–Ag and Ng–Cu containing systems. Therefore, we have investigated the optimized Ng–M bond lengths, the bond dissociation energy, and the Ng–M stretching frequency and the corresponding force constant values for $\text{NgM}_{3-k}\text{H}_k^+$ (M = Cu and Ag; $k = 0-2$) complexes, and the results are found to be similar to that of the $\text{NgAu}_{3-k}\text{H}_k^+$ species. All the HOMO–LUMO energy values and the NBO charges of the concerned $\text{M}_{3-k}\text{H}_k^+$ and $\text{NgM}_{3-k}\text{H}_k^+$ complexes strongly indicate that the decrease in the energy gap between the HOMO of Ng and LUMO of MH_2^+ and considerable increase of positive charge on the metal atom in MH_2^+ ion enhance the electron density transfer from HOMO of Ng atom to the LUMO of MH_2^+ species, which leads to the formation of stronger Ng–M bonding in the case of all $\text{NgM}_{3-k}\text{H}_k^+$ complexes. Various energy components for all the NgMH_2^+ complexes clearly reveal that the electrostatic and orbital components of bonding energy play a key

role for the formation of a strong Ng-M bond in NgMH_2^+ complexes. It is interesting to note that the $\text{NgAg}_{3-k}\text{H}_k^+$ and $\text{NgCu}_{3-k}\text{H}_k^+$ complexes follow similar trends while going from pure metal trimers to hydrogen doped metal trimers as is observed in the case of $\text{NgAu}_{3-k}\text{H}_k^+$ complexes. However, all these effects are more pronounced in $\text{NgAu}_{3-k}\text{H}_k^+$ complexes due to the presence of strong relativistic effects in gold.³¹

III.G. Effect of Relativistic Interaction

In general, the relativistic effect is extremely important for any molecular system containing heavy atom. Hence, we have investigated the effect of relativistic interactions on the Xe-Au bonding since both Xe and Au are heaviest as far as present discussion is concerned. The optimized Xe-Au bond length, bond energy and the HOMO-LUMO gap (ΔE_{Gap}) values for the XeAu_3^+ , XeAu_2H^+ , and XeAuH_2^+ complexes are given in Table 3. The change in optimized Xe-Au bond length (R) values are found to be small (0.06–0.08 Å) after inclusion of explicit spin-orbit interaction as compared to those obtained by RECP method. The effect of spin-orbit interaction is found to be insignificant in terms of the bond dissociation energy (BE) values (2.5–6.5 kJ mol⁻¹). It is to be noted that the molecular orbital energy

Table 3. Optimized Xe-Au Bond Length (R, in Å), binding energy (BE, kJ mol⁻¹), and HOMO-LUMO gap (ΔE_{Gap} , eV) for $\text{XeAu}_k\text{H}_{3-k}^+$ (k = 1-3) Complexes.

Para-meter	Methods	XeAu_3^+	XeAu_2H^+	XeAuH_2^+
$R_{\text{Xe-Au}}$	RECP	2.652	2.627	2.576
	SCL	2.732	2.694	2.640
	SO	2.722	2.686	2.636
BE	RECP	69.5	90.0	129.0
	SCL	62.2	84.5	122.5
	SO	65.1	87.5	125.8
ΔE_{Gap}	RECP	7.807	8.996	11.200
	SCL	8.570	9.630	11.696
	SO	8.271	9.414	11.619

levels are somewhat shifted due to the effect of spin-orbit interaction. A slight change (0.4–0.6 eV) is observed in the ΔE_{Gap} for these clusters after inclusion of spin-orbit interaction with relativistic effect. From the results reported in Table 3 it can be inferred that the RECP method is quite adequate to describe the relativistic effects in noble gas-noble metal interactions. Further, results obtained with the scalar relativistic method are very close to the corresponding values obtained with inclusion of spin-orbit

Table 4. Various Energy Components (kJ mol⁻¹) for NgAu_3^+ , NgAu_2H^+ , and NgAuH_2^+ (Ng = Ar, Kr, and Xe) Species as Obtained Using PBE-D3/TZ2P Method by Taking MP2 Optimized Geometry.

Complexes	Pauli Repulsion Energy	Electrostatic Energy	Orbital Interaction Energy	Dispersion Energy	Total Bonding Energy
ArAu_3^+	112.33	-67.31	-77.88	-2.16	-35.02
ArAu_2H^+	132.91	-77.56	-102.11	-1.49	-48.25
ArAuH_2^+	144.14	-85.47	-142.82	-0.83	-84.99
KrAu_3^+	169.73	-109.27	-114.45	-2.86	-56.84
KrAu_2H^+	177.37	-111.67	-136.69	-1.92	-72.92
KrAuH_2^+	179.63	-115.21	-180.49	-1.05	-117.12
XeAu_3^+	242.26	-165.37	-162.74	-3.77	-89.62
XeAu_2H^+	233.96	-156.88	-182.44	-2.44	-107.80
XeAuH_2^+	224.74	-154.33	-229.03	-1.27	-159.89

interaction. Therefore, EDA analysis has been carried out with the scalar relativistic approach and clearly shows that the increase in the Ng–Au bonding interaction on replacing of Au atom with H atom is due to the enhancement of the orbital interaction energy component (Table 4).

An increase in both covalent characteristics and charge induced dipole interaction through successive replacement of Au atom with H atom in Ng–Au₃⁺ complex is further supported by the calculated values of various energy components (Table 4), which reveal that there has been an increase of both electrostatic and orbital components in going from NgAu₃⁺ to NgAuH₂⁺ species. It is also very important to note that the extent of increase in orbital component is significantly higher, particularly for the Ar–Au₃⁺ complex.

IV. Concluding Remarks



In summary, hydrogen doping has been found to have exceptional influence in the enhancement of noble gas–noble metal bonding strength in NgM₃⁺ (Ng = Ar, Kr, and Xe; M = Cu, Ag, and Au) ions, which have been explored⁴⁰ by using various high level *ab initio* methodologies. The concept of gold–hydrogen analogy, which has become popular in recent years, has been utilized to study this pronounced effect of hydrogen doping in Au trimers, which leads to the formation of strongest Ng–Au bond in NgAuH₂⁺ species, which is evident from the calculated Ng–Au bond length, bond energy, vibrational frequency and force constant values. Similar trends have been found in the case of Ng–Ag and Ng–Cu complexes. The enhancement of Ng–M bonding interaction in Ng–MH₂⁺ (Ng = Ar, Kr, and Xe; M = Cu, Ag, and Au) as compared to that in Ng–M₃⁺ can be attributed to considerable increase in the Ng–M covalency as evident from the analysis of electron density based topological properties and energy decomposition analysis. Moreover, an enhancement in the charge–induced dipole interaction is also responsible for the unusual high Ng–M bonding interaction in Ng–MH₂⁺

species as implied by the calculated values of frontier orbital (HOMO and LUMO) energies and the partial atomic charges. All the very high level theoretical results discussed here and earlier experimental evidences on the existence of AgH₂⁺,³⁹ Au_xH₂⁺,⁵² and Ng–MX (Ng = Ar, Kr, Xe; M = Cu, Ag, Au; X = F, C)^{20,48} species along with very recent experimental identification of Ar complexes of mixed noble metal clusters, Ar_kAu_nAg_m⁺ (n + m = 3; k = 0–3) by Fielicke and co-workers³⁴ clearly suggest that the predicted Ng–MH₂⁺ species are likely to be observed experimentally, and it would be worthwhile to investigate experimentally.

References

1. J. Wilks, *The Properties of Liquid and Solid Helium*, Oxford : Clarendon Press, UK, 1967, 703.
2. W. Kossel, *Ann. Phys. (Leipzig)*, 1916, **49**, 229.
3. G. N. Lewis, *J. Am. Chem. Soc.*, 1916, **38**, 762.
4. M. Ozima and F. A. Podosek, *Noble Gas Geochemistry*, Cambridge University Press, UK, 2002.
5. Bobrow Test Preparation Services, Cliffs A P Chemistry, 2007, 15.
6. N. Bartlett, *Proc. Chem. Soc.*, 1962, **112**, 218.
7. (a) L. Khriachtchev, M. Pettersson, N. Runeberg, J. Lundell and M. Räsänen, *Nature (London)*, 2000, **406**, 874; (b) L. Khriachtchev, M. Pettersson, A. Lignell and M. Räsänen, *J. Am. Chem. Soc.*, 2001, **123**, 8610.
8. R. B. Gerber, *Annu. Rev. Phys. Chem.*, 2004, **55**, 55.
9. M. Pettersson, L. Khriachtchev, J. Lundell and M. Räsänen in *Inorganic Chemistry in Focus II*, eds. G. Meyer, D. Naumann and L. Wesemann, Wiley-VCH, Weinheim, 2005, p. 15.
10. L. Khriachtchev, M. Räsänen and R. B. Gerber, *Acc. Chem. Res.*, 2009, **42**, 183.
11. L. Khriachtchev, K. Isokoski, A. Cohen, M. Räsänen and R. B. Gerber, *J. Am. Chem. Soc.*, 2008, **130**, 6114.
12. T. Jayasekharan and T. K. Ghanty, *J. Chem. Phys.*, 2006, **124**, 164309.
13. T. Jayasekharan and T. K. Ghanty, *J. Chem. Phys.*, 2008, **129**, 184302.
14. T. Jayasekharan and T. K. Ghanty, *J. Chem. Phys.*, 2012, **136**, 164312.
15. M. J. Barlow, B. M. Swinyard, P. J. Owen, J. Cernicharo, H. L. Gomez, R. J. Ivison, O. Krause, T. L. Lim, M. Matsuura, S. Miller, G. Olofsson and E. T. Polehampton, *Science*, 2013, **342**, 1343.
16. L. Khriachtchev, S. Tapio, A. V. Domanskaya, M. Räsänen, K. Isokoski and J. Lundell, *J. Chem. Phys.*, 2011, **134**, 124307.
17. D. Schröder, H. Schwarz, J. Hrušák and P. Pyykkö, *Inorg. Chem.*, 1998, **37**, 624.
18. P. Pyykkö, *J. Am. Chem. Soc.*, 1995, **117**, 2067.
19. S. Seidel and K. Seppelt, *Science*, 2000, **290**, 117.
20. C. J. Evans, A. Lesarri and M. C. L. Gerry, *J. Am. Chem. Soc.*, 2000, **122**, 6100.

21. (a) C. J. Evans and M. C. L. Gerry, *J. Chem. Phys.*, 2000, **112**, 9363; (b) C. J. Evans, D. S. Rubinoff and M. C. L. Gerry, *Phys. Chem. Chem. Phys.*, 2000, **2**, 3943; (c) J. M. Michaud and M. C. L. Gerry, *J. Am. Chem. Soc.*, 2006, **128**, 7613 and references therein; (d) L. Belpassi, I. Infante, F. Tarantelli and L. Visscher, *J. Am. Chem. Soc.*, 2008, **130**, 1048.
22. C. J. Evans, T. G. Wright and A. M. Gardner, *J. Phys. Chem. A*, 2010, **114**, 4446.
23. X. Chen, A. M. Plonka, D. Banerjee, R. Krishna, H. T. Schaefer, S. Ghose, P. K. Thallapally and J. B. Parise, *J. Am. Chem. Soc.*, 2015, **137**, 7007.
24. (a) J. Liu, P. K. Thallapally and D. Strachan, *Langmuir*, 2012, **28**, 11584; (b) P. K. Thallapally, J. W. Grateb and R. K. Motkuria, *Chem. Commun.*, 2012, **48**, 347.
25. D. Banerjee, C. M. Simon, A. M. Plonka, R. K. Motkuri, J. Liu, X. Chen, B. Smit, J. B. Parise, M. Haranczyk and P. K. Thallapally, *Nat. Commun.*, 2016, **7**, 11831.
26. C. A. Fernandez, J. Liu, P. K. Thallapally and D. M. Strachan, *J. Am. Chem. Soc.*, 2012, **134**, 9046.
27. T. Vazhappilly, T. K. Ghanty and B. N. Jagatap, *J. Phys. Chem. C*, 2016, **120**, 10968.
28. J. Liu, D. M. Strachana and P. K. Thallapally, *Chem. Commun.*, 2014, **50**, 466.
29. T. Vazhappilly, T. K. Ghanty and B. N. Jagatap, *J. Nucl. Mater.*, 2017, **490**, 174.
30. P. Pyykkö, *Angew. Chem., Int. Ed.*, 2004, **43**, 4412.
31. B. Kiran, X. Li, H. -I. Zhai, L. -F. Cui and L. -S. Wang, *Angew. Chem., Int. Ed.*, 2004, **43**, 2125.
32. A. Avramopoulos, M. G. Papadopoulos and A. J. Sadlej, *Chem. Phys. Lett.*, 2003, **370**, 765.
33. (a) T. K. Ghanty, *J. Chem. Phys.*, 2005, **123**, 074323. (b) T. K. Ghanty, *J. Chem. Phys.*, 2006, **124**, 124304.
34. (a) A. Shayeghi, R. L. Johnston, D. M. Rayner, R. Schäfer and A. Fielicke, *Angew. Chem., Int. Ed.*, 2015, **54**, 10675; (b) A. Shayeghi, R. Schäfer, D. M. Rayner, R. L. Johnston and A. Fielicke, *J. Chem. Phys.*, 2015, **143**, 024310.
35. X. Li, B. Kiran and L. -S. Wang, *J. Phys. Chem. A*, 2005, **109**, 4366.
36. (a) X. Wang, L. Andrews, K. Willmann, F. Brosi and S. Riedel, *Angew. Chem., Int. Ed.*, 2012, **51**, 10628; (b) X. Wang, L. Andrews, F. Brosi, S. Riedel, *Chem. -Eur. J.*, 2013, **19**, 1397; (c) T. K. Ghanty, *J. Chem. Phys.*, 2005, **123**, 241101.
37. (a) S. Buckart, G. Ganteför, Y. D. Kim and P. Jena, *J. Am. Chem. Soc.*, 2003, **125**, 14205; (b) S. M. Lang, T. M. Bernhardt, R. N. Barnett, B. Yoon and U. Landman, *J. Am. Chem. Soc.*, 2009, **131**, 8939; (c) N. K. Jena, K. R. S. Chandrakumar and S. K. Ghosh, *J. Phys. Chem. Lett.*, 2011, **2**, 1476.
38. K. Mondal, S. Agrawal, D. Manna, A. Banerjee and T. K. Ghanty, *J. Phys. Chem. C*, 2016, **120**, 18588.
39. (a) H. -J. Zhai, B. Kiran and L. -S. Wang, *J. Chem. Phys.*, 2004, **121**, 8231; (b) G. N. Khairallah and R. A. J. O'Hair, *Dalton Trans.*, 2005, 2702; (c) H. Xie, X. Xing, Z. Liu, R. Cong, Z. Qin, X. Wu, Z. Tang and H. Fan, *Phys. Chem. Chem. Phys.*, 2012, **14**, 11666; (d) K. Vetter, S. Proch, G. F. Ganteför, S. Behera and P. Jena, *Phys. Chem. Chem. Phys.*, 2013, **15**, 21007.
40. A. Ghosh and T. K. Ghanty, *J. Phys. Chem. A* 2016, **120**, 9998.
41. (a) J. -D. Chai and M. Head-Gordon, *J. Chem. Phys.*, 2008, **128**, 084106; (b) J. -D. Chai and M. Head-Gordon, *Phys. Chem. Chem. Phys.*, 2008, **10**, 6615.
42. M. J. Frisch, M. Head-Gordon and J. A. Pople, *Chem. Phys. Lett.*, 1990, **166**, 275.
43. C. Hampel, K. Peterson and H. -J. Werner, *Chem. Phys. Lett.*, 1992, **190**, 1.
44. M. W. Schmidt, K. K. Baldridge, J. A. Boatz, S. T. Elbert, M. S. Gordon, J. H. Jensen, S. Koseki, N. Matsunaga, K. A. Nguyen, S. Su, *et al.* *J. Comput. Chem.*, 1993, **14**, 1347.
45. H. -J. Werner, P. J. Knowles, G. Knizia, F. R. Manby, M. Schütz, P. Celani, T. Korona, R. Lindh, A. Mitrushenkov, G. Rauhut, *et al.* MOLPRO, version 2012.1, a Package of *ab initio* Programs, 2012; see <http://www.molpro.net>.
46. E. van Lenthe and E. J. Baerends, *J. Comput. Chem.*, 2003, **24**, 1142.
47. (a) T. Ziegler and A. Rauk, *Theor. Chim. Acta*, 1977, **46**, 1; (b) F. M. Bickelhaupt and E. J. Baerends, In *Reviews on Computational Chemistry*; eds. K. B. Lipkowitz and D. B. Boyd, Wiley-VCH: New York, 2000, Vol. 15, pp 1–86.
48. (a) G. te Velde, F. M. Bickelhaupt, S. J. A. van Gisbergen, C. Fonseca-Guerra, E. J. Baerends, J. G. Snijders and T. Ziegler, *J. Comput. Chem.*, 2001, **22**, 931; (b) E. J. Baerends, ADF 2013.01, SCM, Theoretical Chemistry, Vrije Universiteit: Amsterdam, The Netherlands, 2013.
49. (a) S. A. Cooke and M. C. L. Gerry, *J. Am. Chem. Soc.*, 2004, **126**, 17000; (b) J. M. Michaud, S. A. Cooke and M. C. L. Gerry, *Inorg. Chem.*, 2004, **43**, 3871.
50. (a) P. Pyykkö, *J. Phys. Chem. A*, 2015, **119**, 2326; (b) P. Pyykkö, M. Atsumi, *Chem. -Eur. J.*, 2009, **15**, 12770; (c) B. Cordero, V. Gómez, A. E. Platero-Prats, M. Revés, J. Echeverría, E. Cremades, F. Barragán and S. Alvarez, *Dalton Trans.*, 2008, 2832.
51. (a) A. Bondi, *J. Phys. Chem.*, 1964, **68**, 441; (b) P. Pyykkö, *Chem. Rev.*, 1997, **97**, 597; (c) J. Vogt and S. Alvarez, *Inorg. Chem.*, 2014, **53**, 9260; (d) S. Alvarez, *Dalton Trans.*, 2013, **42**, 8617.
52. L. M. Ghiringhelli, P. Gruene, J. T. Lyon, D. M. Rayner, G. Meijer, A. Fielicke and M. Scheffler, *New J. Phys.*, 2013, **15**, 083003 and references therein.

	<p>Shri Ayan Ghosh joined Laser and Plasma Technology Division in 2010 after completing BARC training school program (OCES, 53rd Batch of Chemistry). His current position is Scientific Officer-D in BARC. He was a Gold Medalist in M.Sc. (Chemistry) from Burdwan University, West Bengal (2007-2009). He is specialised in the field of Noble Gas Chemistry. Presently, he is doing Ph.D. under the supervision of Dr. Tapan K. Ghanty at Homi Bhabha National Institute, Mumbai. His research interest is computational investigations of weakly interacting chemical systems involving noble gas atoms and experimental study pertaining to laser-isotope separations. He has investigated various novel class of noble gas containing chemical compounds using ab initio density functional theory based methods.</p>
	<p>Dr. Tapan K. Ghanty is currently holding the position of Head, Theoretical Chemistry Section at Bhabha Atomic Research Centre. He is also a Professor of Homi Bhabha National Institute. After obtaining his M.Sc. degree in Physical Chemistry from Burdwan University, Dr. T. K. Ghanty joined BARC in 1988 through 32nd batch Training School and received Homi Bhabha Award. He obtained his Ph.D. degree in Chemistry from Bombay University in 1996 for his work on density functional theory of chemical binding and chemical reactivity on molecular systems. He has spent two years (1997-99) at Chemistry Department, Indiana University, USA as a postdoctoral fellow. His research interests include theoretical prediction of novel rare-gas compounds, computational investigation of structure and properties of hydrogen-bonded systems, supramolecular chemistry, electronic excited states, clusters and cluster assembled materials. He is also involved in the study of structure and bonding in lanthanide and actinide complexes relevant to nuclear waste management. He is the recipient of DAE Scientific & Technical Excellence award in the year 2009 for his important contribution on the prediction of chemical compounds involving noble gas – noble metal chemical bond. In 2014 he received the Homi Bhabha Science & Technology Award for his work on lanthanide-actinide separation and prediction of actinide encapsulated fullerenes. He is a fellow of the Maharashtra Academy of Sciences. He has been elected as a fellow of the National Academy of Sciences, India in 2014. Dr. Ghanty has co-authored more than 140 papers in peer reviewed international journals.</p>

Contents

Message from the President and Secretary, ISRAPS	i
Guest Editors	iii
<i>Soumyakanti Adhikari</i>	
<i>Subrata Sinha</i>	
Doped Carbon Nanodot: Heterogeneity in Molecular and Cluster level	1
<i>Debashis Panda, Shivoam Dwivedi</i>	
Intertwined Facet of Lasers and Accelerators	8
<i>Sisir K Sarkar</i>	
Radiation Processing: A non-thermal technology for food preservation	16
<i>Sunil K. Ghosh</i>	
Pulse Radiolysis Study of 4-Nitrophenol Reduction Reaction using Porous Platinum Nanoballs	25
<i>G. K. Sharma and K. K. K. Sharma</i>	
Reactions of model peroxy ($\text{CCl}_3\text{O}_2\cdot$) radical by radiation chemical method	32
<i>Shaikat Ali M. Shaikh, Rupali G. Shinde, Atanu Barik</i>	
"Super-Strong" van der Waals Complexes involving Noble Gases	40
<i>Ayan Ghosh and Tapan K. Ghanty</i>	